

Dynamic Modeling, Design and Control of Power Converters for Renewable Interface
and Microgrids

by

Ziwei Yu

A Dissertation Presented in Partial Fulfillment
of the Requirements for the Degree
Doctor of Philosophy

Graduate Supervisory Committee:

Raja Ayyanar, Chair
Vijay Vittal
Jiangchao Qin
Yang Weng

ARIZONA STATE UNIVERSITY

August 2018

ABSTRACT

Distributed energy resources have experienced dramatic growth and are beginning to support a significant amount of customer loads. Power electronic converters are the primary interface between the grid and the distributed energy resources/storage and offer several advantages including fast control, flexibility and high efficiency. The efficiency and the power density by volume are important performance metrics of a power converter. Compact and high efficiency power converter is beneficial to the cost-effectiveness of the converter interfaced generations. In this thesis, a soft-switching technique is proposed to reduce the size of passive components in a grid-connected converter while maintaining a high power conversion efficiency. The dynamic impact of the grid-connected converters on the power system is causing concerns as the penetration level of the converter interfaced generation increases, necessitating a detailed dynamic analysis. The unbalanced nature of distribution systems makes the conventional transient stability simulation based on positive sequence components unsuitable for this purpose. Methods suitable for the dynamic simulation of grid-connected converters in large scale unbalanced and single-phase systems are presented in this thesis to provide an effective way to study the dynamic interactions between the grid and the converters. Dynamic-link library (DLL) of converter dynamic models are developed by which converter dynamic simulations can be easily conducted in OpenDSS. To extend the converter controls testing beyond pure simulation, real-time simulation can be utilized where partial realistic scenarios can be created by including realistic components in the simulation loop. In this work, a multi-platform, real-time simulation testbed including actual digital controller platforms, communication networks and inverters has been developed for validating the microgrid concepts and

implementations. A hierarchical converted based microgrid control scheme is proposed which enables the islanded microgrid operation with 100% penetration level of converter interfaced generation. Impact of the load side dynamic modeling on the converter response is also discussed in this thesis.

ACKNOWLEDGMENTS

I would like to thank my advisor Dr. Raja Ayyanar for offering me this precious research and studying opportunity in Arizona State University. His continuous inspiration, guidance and immense knowledge have always been indispensable throughout my Ph. D study.

I would like to express my gratitude to my committee members, Dr. Vijay Vittal, Dr. Jiangchao Qin and Dr. Yang Weng, for their precious and insightful advice on my research and thesis.

I also wish to thank my colleges and friends Chenhao Nan, Yingying Tang, Caleb, Siddharth Kulasekaran, Tong Yao, Yinglai Xia, Jinia Roy, Deepak Ramasubramanian, R. Scott Mongrain, Pavan Kumar Hari, Nikhil Korada, Ankul Gupta and Hemanth Mullangi. Cooperation and discussion with them have always been joyful and enlightening.

I would like to thank my parents, Qin Yu and Ping Ouyang for supporting me both financially and spiritually. Last but not the least, I want to express my special thank to my wife Yuan Ge and my son Miduo for your love and support in my daily life.

TABLE OF CONTENTS

	Page
LIST OF TABLES	IX
LIST OF FIGURES	X
LIST OF ACRONYMS	XVII
CHAPTER	
1 INTRODUCTION.....	1
1.1 Grid-connected converters in distribution systems.....	1
1.2 Dynamic simulation of grid-connected converters in large scale distribution systems	2
1.3 Real-time simulation of power system and power electronics	4
1.4 Thesis organization	6
2 HIGH EFFICIENCY GRID-CONNECTED CONVERTER	8
2.1 Proposed circuit operating principle	10
2.1.1 Hybrid PWM modulation	10
2.1.2 ZVS turn-on realization for the high frequency switches	12

CHAPTER	Page
2.2 Timing control of the auxiliary switch for optimized loss saving	15
2.2.1 Cases when grid voltage is low	15
2.2.2 Cases when grid voltage is high	27
2.3 System design of a 3.3 kW prototype of the proposed circuit	30
2.3.1 LCL filter design	30
2.3.2 Determine the auxiliary inductance value	31
2.3.3 Device stress of S_1 and S_2	34
2.3.4 Control system of the converter	35
2.4 Hardware implementation and experimental results	38
2.4.1 Hardware prototype development	38
2.4.2 Experiment results	39
3 DYNAMIC SIMULATION OF GRID-CONNECTED CONVERTERS IN LARGE-SCALE DISTRIBUTION SYSTEMS	48
3.1 Dynamic simulation of grid-connected converter by EMT-TS hybrid simulation and phasor extraction techniques	48
3.1.1 Phasor extraction based on sampled data over a sliding window	50
3.1.2 Phasor extraction based on direct-quadrature transformation	51
3.1.3 Complex analytical signal model/dynamic phasor model	52
3.2 Comparison of the stability of the simulation using different phasor extraction techniques	53

CHAPTER	Page
3.2.1 Derivation of the analytical model of simulation	54
3.2.2 Stability of EMT-TS simulation based on different phasor extraction methods .	60
3.3 Dynamic phasor model of a single-phase grid-connected converter	67
3.4 Dynamic simulation of grid-connected converters in large unbalanced distribution systems using OpenDSS	70
3.4.1 Dynamic simulation in OpenDSS by using DLLs	70
3.4.2 Validation in IEEE 13-node test system	73
3.4.3 Volt-VAr control implementation in a large, real feeder.....	78
3.4.4 CIG based microgrid control in IEEE 123-node test feeder.....	80
3.4.5 Discussion.....	82
 4 REAL-TIME SIMULATION OF A MICROGRID POWERED BY CONVERTER-INTERFACED GENERATORS.....	 83
4.1 Hierarchical control of CIG based microgrids.....	83
4.1.1 Level 1 control	85
4.1.2 Level 2 control	88
4.1.2 Level 3 control	90
4.2 Multi-platform microgrid real-time simulation testbed	91
4.2.1 EMT-TS hybrid dynamic simulation in Opal-RT.....	92
4.2.2 Controller-hardware-in-loop (CHIL) simulation	93
4.2.3 Simulation with remote microgrid central controller	94

CHAPTER	Page
4.3 A microgrid test case based on IEEE 123 node test feeder	96
4.3.1 Microgrid configuration.....	96
4.3.2 Energy cell specifications	97
4.3.3 Controller design.....	98
4.4 Simulation results of IEEE 123 node test feeder configured as microgrid.....	101
4.4.1 Grid-connected operation	101
4.4.2 Islanded microgrid operation	102
4.5 Dynamic load modeling.....	107
4.5.1 Modeling of AC compressor motor.....	107
4.5.2 Inverter current limiting scheme under fault condition	111
4.5.3 Simulation results	113
5 CONCLUSIONS AND FUTURE WORK	120
5.1 Conclusions.....	120
5.2 Future work.....	121
REFERENCE.....	124
APPENDIX	
A ANALYSIS OF THE TURN-ON TRANSITION WHEN $V_G > 0.5V_{DC}$..	135

B CIRCUIT SCHEMATIC AND PCB LAYOUT OF THE HARDWARE
PROTOTYPE 147

C BLOCK DIAGRAMS OF THE MICROGRID OPAL-RT MODEL..... 153

D MATLAB FUNCTION FOR THE DYNAMIC PHASOR MODEL OF
SINGLE-PHASE PERMANENT-SPLIT CAPACITOR MOTOR 158

LIST OF TABLES

Table	Page
2.1 Parameters for loss calculations in Figure 2.12	26
2.2 Parameters for loss calculations in Figure 2.14	28
2.3 Prototype specifications	38
2.4 Comparison with recent full-bridge based inverter/PFC	47
3.1 Other system parameters used in the closed loop pole calculation.....	63
3.2 Simulation time comparison	76
4.1 Energy cell Modbus mapping	96
4.2 Energy cell specifications	97
4.3 Air conditioner compressor induction machine parameters	114

LIST OF FIGURES

Figure	Page
2.1 Grid-connected converter based on full-bridge topology	9
2.2 Proposed ZVT full-bridge grid-connected converter.....	10
2.3 Gate signals of the full-bridge converter in hybrid PWM modulation scheme	11
2.4 Converter power pole voltage in hybrid PWM modulation scheme.....	11
2.5 Timing diagram of the ZVT converter in ideal case.....	12
2.6 Commutation states of the proposed ZVT converter	14
2.7 Case <i>a</i> of the Q_2 turn-on transition when $v_g < 0.5V_{dc}$	16
2.8 Case <i>b</i> of the Q_2 turn-on transition when $v_g < 0.5V_{dc}$	19
2.9 Case <i>c</i> of the Q_2 turn-on transition when $v_g < 0.5V_{dc}$	20
2.10 Case <i>d</i> of the Q_2 turn-on transition when $v_g < 0.5V_{dc}$	24
2.11 Turn-on energy loss of C2M0025120D SiC MOSFET	25
2.12 Losses in the turn-on transition as T_a increases when $v_g < 0.5V_{dc}$	26
2.13 Turn-on transitions when $v_g > 0.5V_{dc}$	27
2.14 Losses in the turn-on transition as T_a increases when $v_g > 0.5V_{dc}$	28
2.15 Loss in the turn-on transition as T_a increases for different grid voltages	29
2.16 Turn-on loss plot with respect to L_{aux}	33
2.17 Control system of the proposed converter	35
2.18 Implementation of the auxiliary switch timing.....	35

Figure	Page
2.19 Bode plot of the PLL.....	36
2.20 Bode plot of the current control loop.....	37
2.21 Dimensions of the ZVT full-bridge converter prototype.....	38
2.22 Photograph of the ZVT full-bridge converter prototype.....	39
2.23 Dimensions of the main filter inductor.....	39
2.24 Fundamental waveforms in inverter mode.....	40
2.25 Fundamental waveforms in PFC mode.....	40
2.26 Gate signals for the main switches and auxiliary switches in PFC mode.....	40
2.27 ZVS turn-on transition waveforms.....	41
2.28 Switching cycle waveforms.....	41
2.29 Auxiliary switch voltage stress.....	42
2.30 Circuit efficiency measurement at 2.4 kW.....	42
2.31 Efficiency curve with and without the proposed ZVT technique.....	43
2.32 Loss breakdown of the proposed the circuit and conventional full-bridge converter.....	43
2.33 Detailed loss breakdown of the proposed circuit.....	43
2.34 Efficiency vs Ta when $V_{dc} = 400\text{ V}$ $v_g = 100\text{ V}$ $i_g = 7.7\text{ A}$	44
2.35 Turn-on transition corresponding to point a in Figure 2.34.....	44
2.36 Turn-on transition corresponding to point b in Figure 2.34.....	45
2.37 Turn-on transition corresponding to point c in Figure 2.34.....	45
2.38 Efficiency vs Ta when $V_{dc} = 400\text{ V}$ $v_g = 300\text{ V}$ $i_g = 7.7\text{ A}$	45

Figure	Page
2.39 Turn-on transition corresponding to point a in Figure 2.38.....	46
2.40 Turn-on transition corresponding to point b in Figure 2.38.....	46
2.41 Turn-on transition corresponding to point c in Figure 2.38.....	46
3.1 Data type conversion between EMT and phasor simulations.....	48
3.2 Application of Hilbert transform and frequency shifting	53
3.3 A simple system in EMT-TS hybrid simulation.....	54
3.4 The simple system based on pi-section line model.....	54
3.5 Equivalent representation of the EMT-TS simulation based on FFT phasor extraction	55
3.6 Representation of the network and dynamic model in the hybrid simulation	55
3.7 EMT-TS simulation based on FFT phasor extraction represented in dq frame.....	57
3.8 Equivalent representation of the EMT-TS simulation based on FFT phasor extraction	58
3.9 Simplified representation of the EMT-TS simulation based on $\alpha\beta$ to dq transformation	59
3.10 Equivalent representation of the EMT-TS simulation based dynamic phasor	60
3.11 Root locus of EMT-TS simulation based on $\alpha\beta$ to dq transformation.....	61
3.12 The highest real part of the closed loop poles of the EMT-TS simulation based FFT phasor extraction: $L_f = 200$ mH.....	62
3.13 The highest real part of the closed loop poles of the EMT-TS simulation based FFT phasor extraction: $R_f/L_f = 25$	63

Figure	Page
3.14 Case 1: $P = 300$ kW, $Q = 100$ kVAr ($z_1 = 155.72$, $z_2 = -52.17$).....	64
3.15 Case 2: $P = 2500$ kW, $Q = 100$ kVAr ($z_1 = 20.87$, $z_2 = -1.23$).....	64
3.16 Case 3: $P = 2.5$ kW, $Q = 2500$ kVAr ($z_1 = 0.19$, $z_2 = -21.14$).....	65
3.17 Case 4: $P = 300$ kW, $Q = 400$ kVAr ($z_1 = 62.4$, $z_2 = -83.35$).....	65
3.18 EMT-TS simulation results based on MATLAB and OpenDSS using three different phasor extraction methods	66
3.19 A single-phase grid-connected converter model [72]:.....	67
3.20 Dynamic simulation using DLL in OpenDSS	70
3.21 Representation of the network and dynamic model in OpenDSS:	71
3.22 Interaction between OpenDSS and the main functions in DLL	72
3.23 Solving power-flow by using the steady state model in DLL	72
3.24 Comparison of proposed method and PLECS time domain simulation: CIG current during a step change in I_d^*	74
3.25 Comparison of proposed method and PLECS time domain simulation: CIG terminal voltage during a step change in I_d^*	75
3.26 Instantaneous value of CIG current: OpenDSS vs PLECS.....	75
3.27 Comparison of proposed method and PLECS time domain simulation: line current during step change in I_d^*	75
3.28 Comparison of proposed method and PLECS time domain simulation: bus voltage during step change in I_d^*	76
3.29 Three-phase SRF-PLL	77

Figure	Page
3.30 Comparison with PLECS time domain simulation and positive sequence model: three-phase CIG response to single-phase fault	77
3.31 PLL frequency after disconnecting the feeder from the grid	78
3.32 OpenDSS model of the distribution feeder in Flagstaff, AZ	79
3.33 Voltage profile along the feeder in snapshot simulation	79
3.34 Voltage profile changing with time in dynamic simulation.....	80
3.35 Droop based microgrid control of single-phase CIG	81
3.36 Active power outputs from the CIGs in the 123-bus test feeder by disconnecting the grid at 1 s.....	81
3.37 Reactive power outputs from the CIGs in the 123-bus test feeder by disconnecting the grid at 1s.....	81
3.38 CIG frequency change after islanding	82
4.1 The physical layer and control structure of a microgrid	83
4.2 Virtual synchronous generator control.....	85
4.3 Dynamic power sharing control.....	88
4.4 Voltage/frequency regulation control	89
4.5 Grid synchronization loop.....	90
4.6 Reactive power controller under grid-connected operation.....	90
4.7 Communication between the central and local controller.....	91
4.8 Multi-platform microgrid real-time simulation testbed	91

Figure	Page
4.9 Microgrid network parameters in excel sheet to be imported to ePHASORSim model	92
4.10 EMT-TS hybrid dynamic simulation in Opal-RT.....	93
4.11 CHIL simulation of the energy cell	93
4.12 CHIL simulation setup for validating the inverter local controls	94
4.13 Modbus based communication network	95
4.14 IEEE 123 node test feeder based microgrid.....	96
4.15 Step response of system voltage by changing the voltage reference	98
4.16 Step response of system frequency by changing the frequency reference.....	99
4.17 Step response of inverter power output by changing the power reference	100
4.18 Small-signal model of the dynamic power sharing loop	100
4.19 Small-signal model of the grid synchronization loop.....	100
4.20 Step change of inverter active power output under grid-connected operation	101
4.21 Step change of inverter reactive power output under grid-connected operation	102
4.22 Inverter angular frequency under system load step change	103
4.23 Inverter terminal voltage under system load step change	103
4.24 Inverter active power output under system load step change	103
4.25 Inverter reactive power output under system load step change	104
4.26 PV generation profile.....	105
4.27 Inverter active power output varying with PV generation.....	105

Figure	Page
4.28 Cell energy level varying with PV generation	105
4.29 Inverter reactive power output varying with PV generation.....	106
4.30 Simulation result of grid synchronization control	106
4.31 Structure of air-conditioner compressor single-phase induction motor [109]	107
4.32 Mechanical load torque at constant speed [109].....	111
4.33 Fault current limiting based on virtual impedance control	113
4.34 Simulation result comparison: stator main winding current under terminal voltage drop	114
4.35 Simulation result comparison: rotor angular speed under terminal voltage drop...	114
4.36 Inverter output current under system fault with constant impedance, constant current and constant power load.....	115
4.37 Inverter terminal voltage under system fault with constant impedance, constant current and constant power load.....	116
4.38 Electromagnetic torque and mechanical load torque under system fault	117
4.39 Air conditioner compressor motor rotor speed under system fault.....	117
4.40 Air conditioner compressor motor terminal voltage and current under system fault	117
4.41 Inverter terminal current under system fault with air conditioner load	118
4.42 Inverter terminal voltage under system fault with air conditioner load.....	118

List of Acronyms

ARCP	Auxiliary resonant commuted pole
CCM	Continuous conduction mode
CHIL	Controller-hardware-in-loop
CIG	Converter-interfaced-generation
CRM	Critical mode
DCM	Discontinuous conduction mode
DER	Distributed energy resource
DLL	Dynamic-link library
EMI	Electromagnetic interference
EMT	Electromagnetic transient
EMTP	Electromagnetic transient programs
FFT	Fast Fourier transform
HIL	Hardware-in-loop
HUT	Hardware under test
PHIL	Power-hardware-in-loop
PR	Proportional-resonant
RES	Renewable energy standards
ROS	Rest of the system
SoC	State of charge

SRF	Synchronous reference frame
TS	Transient stability
VSG	Virtual synchronous generator
ZCS	Zero-current-switching
ZVS	Zero-voltage-switching
ZVT	Zero-voltage-transition

CHAPTER 1 INTRODUCTION

1.1 Grid-connected converters in distribution systems

Technology advances, environmental concerns and ambitious renewable energy standards (RES) have led to an increasing interest in distributed energy resources (DERs). Among all DERs, converter interfaced generations (CIGs) utilizing renewable energy (wind and solar) or micro-sources (fuel cells and micro-turbines) are experiencing a rapid development in distribution systems [1]-[4]. Converters are also used as the interface of energy storage, capable of providing some of the grid support features as discussed in [5]-[8]. Fast evolution of the power electronic converters, mainly from two perspectives - semiconductor power devices and real-time controllers, has led to the development of cost-effective and grid-friendly converters [8]. The power loss of the power electronic converters is mainly introduced by the semiconductor power devices. The development of wide bandgap semiconductors such as SiC and GaN has resulted in power devices capable of operating at higher voltage, higher temperature and higher switching speed than the conventional Si based devices [10]. These improved power device properties can lead to higher efficiency and higher switching frequency converters where the size and cost of the cooling system and passive filter components can be drastically reduced [18]-[20]. The use of fast digital controllers makes it possible to implement high bandwidth and complex controls for the converters. Several converter control schemes have been proposed and successfully implemented in hardware for various control objectives in power system applications [10]-[17]. The most common control is in the grid-synchronized mode [10] where converter output current is regulated, and the phase is synchronized with the terminal

voltage through a PLL. Droop control [11] can be added as an upper level control above the grid current control in the grid-synchronized mode when the converter participates in grid frequency regulation or provides grid voltage support. Another type of control involves the autonomous control of converter based microgrid or UPS systems where large generators providing stable frequency and voltage reference are absent [12]-[17]. Instead of PLL, P-Q droops are essential components which generate the voltage and frequency reference for the converter in this type of controls.

1.2 Dynamic simulation of grid-connected converters in large scale distribution systems

Many electric utilities have active advanced inverter pilot programs to understand the capabilities and technical performance of PV and energy storage converters, and their implications to distribution system management, and to determine the most suitable methods to control these DERs with manageable and cost-effective communications. As the penetration levels of CIGs constantly increase, concerns arise on their dynamic impact, such as fault current contribution and voltage violations. Also, as the CIGs assume an increasingly significant role in distribution system management with advanced autonomous control, the dynamic interactions among the CIGs and between CIGs and legacy control and protection devices need to be fully understood and considered in the system design. The extreme number of CIGs to be modeled in a large distribution system with several thousands of nodes, and the wide range of time scales involved in the different dynamic events make the dynamic analysis challenging.

New methods and high performance, electromagnetic transient (EMT) level analysis and simulation tools are therefore needed. Electromagnetic transient programs

(EMTP) (PLECS [42], PSCAD [43], MATLAB/Simulink) are capable of modeling a power system in detail, and conducting time domain simulations using small time-steps. However, a detailed time-domain simulation for a typical distribution system which contains hundreds or thousands of laterals and sub-laterals is impractical since it requires substantial computational resources. A practical way to simulate such large systems is the reduced order simulation where the major part of the system (mainly the network part including lines and loads) is simplified while using the detailed model for one or several components or areas of interest. This concept can be found in the traditional transient stability (TS) simulations [45]-[47] as well as the hybrid of TS and EMT simulations [48]-[54]. To simplify the network model, the steady state representations (algebraic equations) similar to those used in power flow are used. The network is considered to be directly passing from one steady state to another and the transient is neglected. The dynamic properties of the selected components or areas are retained by using detailed model represented by differential equations. This type of simulation is referred to as dynamic simulation in the rest of this thesis.

Dynamic models of various types of devices used in dynamic simulations such as synchronous generator, induction machine and more recently CIG are available in the literature [55]-[60]. In transmission system level simulations, positive-sequence model is used for both the network and detailed component models such as synchronous generator, induction machine and CIG. However, models corresponding to unbalanced operation and single-phase systems are needed while analyzing distribution systems. This is found to be necessary because distribution systems are naturally unbalanced with untransposed lines, single-phase laterals and unbalanced loads. An example of such models can be found in

[61] where an unbalanced model is derived for synchronous generators to study microgrid operation in the distribution system analysis tool GridLAB-D. When the dynamic model contains fast changing components, and natural waveform is used instead of phasor, the simulation becomes more like a TS-EMT hybrid simulation [48]-[54]. In this type of simulation, the main issues are at the interface between the dynamic model and the network model, including choosing the equivalent representation of the detailed system and the external system, conversion between phasor and natural waveform data, and the interaction protocol between the quasi-static simulation (network) and full order dynamic simulation (detailed system). Several analytical tools are now available with the capability to analyze unbalanced distribution systems such as OpenDSS [44], CYMDIST [62], and GridLab-D [63]. Among them, OpenDSS is an open source program which can be used to run various types of simulations including steady state, quasi-static, and with suitable dynamic model, dynamic simulations [47], [64] and [65]. The dynamic model can be written in dynamic-link library (DLL) and used by OpenDSS for dynamic simulations. One of the merits of using DLL is that it can help protect the proprietary information for the device vendors who want to provide the dynamic model of their products. Using DLL also has the advantage of scalability, for example, only one DLL is needed when multiple instances of the same devices are in the system.

1.3 Real-time simulation of power system and power electronics

A digital real-time simulator, as the name suggests, generates real time accurate waveforms at its output that represent the behavior of the system being modeled in the simulator. To achieve real-time simulation, the simulator needs to solve the system model for one step within the same time length in real world. Thus, the real-time simulation can

easily become a computationally intensive task, which requires large amount of computational resources and special techniques of implementing parallel processing. Some advantages of using real-time simulation in system design and testing are

- Reduces development costs by identifying design issues in early stage of the process
- Effective way for controller development
- Testing costs are reduced and testing results are more repeatable
- An easier way to conduct tests that are very expensive and risky in real world

The real-time simulation can be categorized into two different types depending on whether external hardware is involved in the simulation setup. The pure software simulation doesn't involve any external hardware, thus the entire system is modeled and simulated in the real-time simulator. While in hardware-in-loop (HIL) simulations, external hardware is connected to the real-time simulator through its IOs and communication ports. The full system is then split into hardware under test (HUT) and rest of the system (ROS) in HIL simulation [100]. ROS is simulated in the real-time simulator and produce the real-time data/waveform for testing the external hardware connected in the loop. HIL simulation can be categorized into controller-hardware-in-loop (CHIL) and power-hardware-in-loop (PHIL) depending on the type of hardware which is being connected to the real-time simulator [78]. In CHIL, real-time controller hardware is connected to the simulator through the IOs. Analog or digital signals are transferred between the hardware and simulator, and no real power transfer is involved. In PHIL, a system with real power involved is simulated while part of the system is simulated in the real-time simulator. A power amplifier is needed in the simulation as the interface between the real-time simulator

and external power hardware. The high voltage side of the power amplifier needs to sink and supply power as it is connected to external power hardware. The low voltage side is connected to the real-time simulator to receive the reference signal which changes based on the simulated system responds. PHIL is used in the test of power converters, machines and other electrical devices.

Commercial real-time simulators relevant to power systems and power electronics study include RTDS [79], Opal-RT [80] and dSPACE [81]. There are also customized real-time simulators which are built in labs for in house research [82]-[84]. Applications of real-time simulators in power system design, analysis and test can be found in the literature [78]-[99]. The real-time simulator has been used to test the controller for medium/high voltage motor drives in [84]-[87]. Hybrid simulation systems based on real-time simulator for studying the performance of wind turbines both electrically and mechanically have been proposed in [88]-[90]. Hardware-in-loop testing of protection and fault isolation devices has been a main application of real-time simulators as described in [92]-[95]. Microgrids have been modeled and simulated in real-time simulators for testing physical microgrid controllers in [96]-[99].

1.4 Thesis organization

The rest of this thesis is organized as three chapters. In Chapter 2, a high frequency, high efficiency grid-connected converter based on full-bridge topology is proposed. The operating principle, control and design of the proposed circuit have been introduced. The hardware prototype and experimental results are also demonstrated. In Chapter 3, methods for dynamic simulation of grid-connected converters in large scale distribution systems and their performance are presented. Dynamic phasor model of the grid-connected converter is

derived for use in hybrid simulations where the large-scale network model is solved by power-flow. Several methods for phasor extraction in the hybrid simulation are introduced and compared. The dynamic simulation by using OpenDSS and DLL is presented. In Chapter 4, a real-time simulation testbed for validating the operation and controls of a converter based microgrid is presented. A multi-platform simulation testbed including realistic controller platforms and communication network is proposed based on the Opal-RT real-time simulator.

CHAPTER 2 High efficiency grid-connected converter

A dc/ac converter which can operate in all four quadrants such as full-bridge converter [17] is needed at the grid side of a bidirectional power conversion system. Figure 2.1 shows the circuit diagram of the full-bridge converter which consists of four semiconductor switches, dc side filter and grid side filter. The grid side filter which is placed between the power pole and grid mitigates the high frequency ripple in the grid current so that it can comply with the standard IEC 61000-3-2 and IEEE 1547. The switching frequency of the converter affects the overall performance of the converter from multiple aspects including efficiency, power density and control bandwidth. Higher switching frequency is preferred when the power density is a major concern of the converter design since the requirement on the grid current filter is reduced [19]-[21]. However, as the switching frequency increases, the switching loss associated with turn-on and turn-off transition of the switches increases so that the converter efficiency is reduced. Moreover, the overall size of the converter might not get reduced by using a very high switching frequency because a large heat sink is needed to handle the excessive heat generated in the switches. Zero-voltage-transition (ZVT) is a type of soft-switching techniques which reduces the power loss associated with the turn-on transition of the switches [22]-[33]. The converter efficiency can be improved by applying ZVT technique especially under cases where a high switching frequency is used. The electromagnetic interference (EMI) generated by the converter can also be reduced by applying such soft-switching techniques [33] [34].

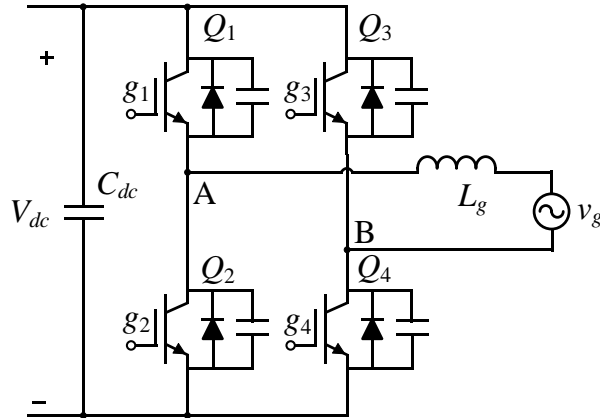


Figure 2.1 Grid-connected converter based on full-bridge topology

ZVT schemes have been introduced for the full-bridge converter without any additional circuit in [22] and [23]. The drawback of this scheme is the required large filter inductor current ripple which makes it difficult to design the inductor. ZVT schemes with auxiliary circuits have also been introduced for full-bridge converter. The auxiliary resonant commuted pole (ARCP) ZVT schemes in [24] and [25] add two separate auxiliary circuits to the system to realize zero-voltage-switching (ZVS) turn-on of the main switches. The use of split dc-link capacitor causes the voltage balancing issue in this scheme. The resonant ac-link converters proposed in [31]-[33] have less components in the auxiliary circuit than ARCP converters, however, is only suitable for bipolar PWM modulation which adds more requirement on the grid-side filter. There are other types of ZVT auxiliary circuit for full-bridge converter including triangular resonant snubber based circuit [26] [27], and coupled inductor based circuits [28]-[30]. Although the mechanism of these ZVT auxiliary circuits are similar, the exact configuration in terms of where the auxiliary circuit is connected to the main circuit are different, which results different overall performance of the converter.

In this chapter, a ZVT scheme is proposed for the full-bridge grid-connected converter. A simple auxiliary circuit is added to the main circuit to realize the ZVS turn-

on of the main switches in the high frequency leg with hybrid PWM modulation scheme. In section 2.2, the circuit topology and basic operating principle are introduced. The timing control of the auxiliary switches is discussed in section 2.3. The system design of a 3.3 kW prototype for the proposed circuit is described in section 2.4. The hardware implementation of the prototype and the experimental results are presented in section 2.5.

2.1 Proposed circuit operating principle

The circuit diagram of the proposed ZVT full-bridge converter is shown in Figure 2.2. A LCL filter (L , C_f and L_g) is used as the grid current filter. An auxiliary branch which consists of two auxiliary switches (S_1 and S_2) and an auxiliary inductor (L_{aux}) is connected across the converter side current filter L . The drain to source capacitor C_{ds} between drain and source of the main switches is shown in the figure since it is needed to explain the transient during switching transitions in detail. $g_1\sim g_4$ and g_{s1} , g_{s2} are the gate signals given to the corresponding switches.

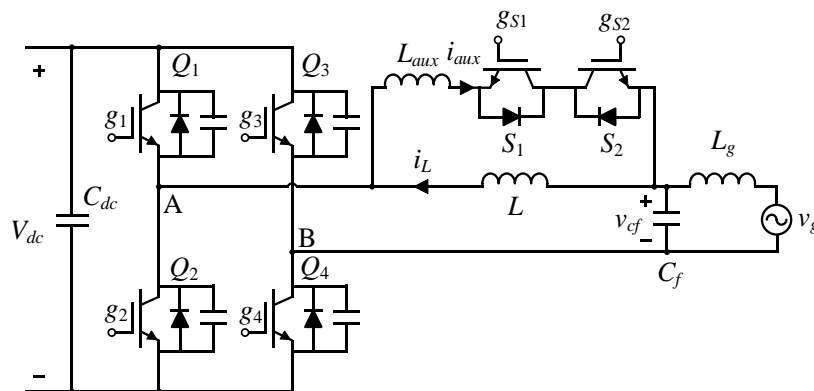


Figure 2.2 Proposed ZVT full-bridge grid-connected converter

2.1.1 Hybrid PWM modulation

One of the main advantages of the proposed circuit is that the hybrid PWM modulation scheme can be used. In hybrid PWM modulation, one leg of the full-bridge

converter (Q_1 and Q_2) switches at high frequency while the other leg (Q_3 and Q_4) switches at the line frequency. The gate signals and the corresponding duties in hybrid PWM modulation are shown in Figure 2.3. The resulting pole voltage v_{AB} is shown in Figure 2.4.

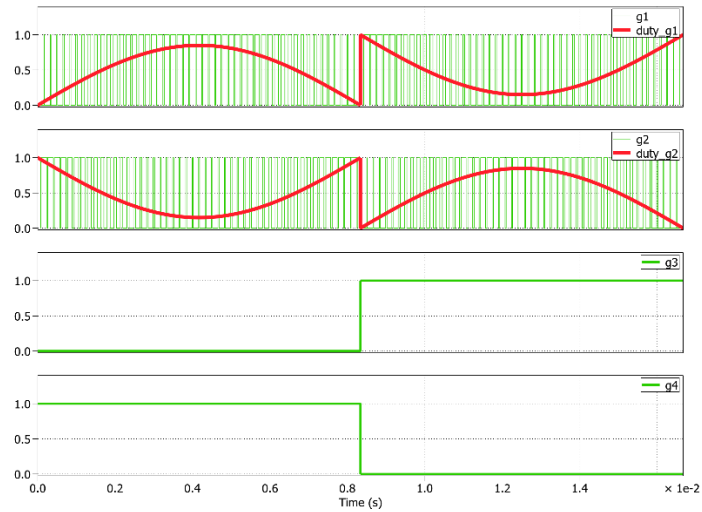


Figure 2.3 Gate signals of the full-bridge converter in hybrid PWM modulation scheme

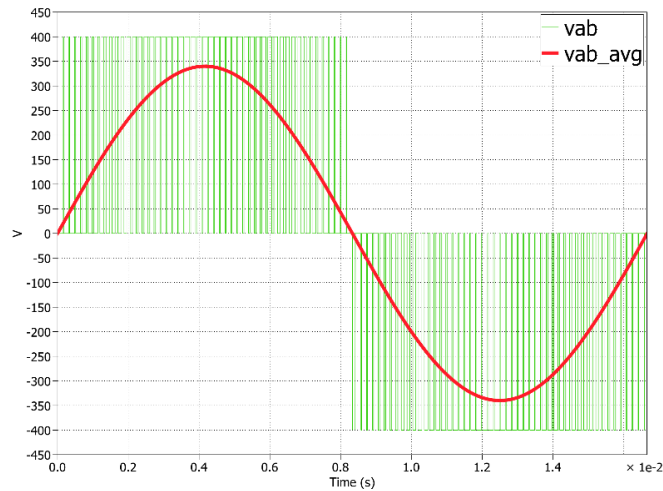


Figure 2.4 Converter power pole voltage in hybrid PWM modulation scheme

2.1.2 ZVS turn-on realization for the high frequency switches

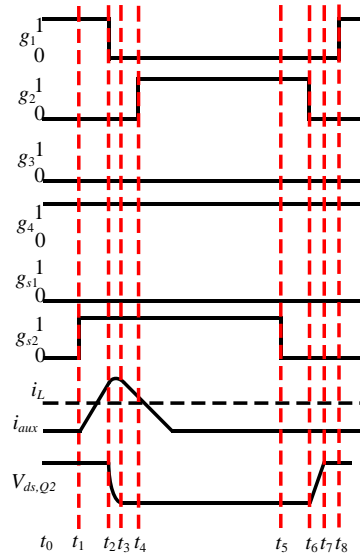


Figure 2.5 Timing diagram of the ZVT converter in ideal case

The operating principle of the auxiliary circuit is illustrated by the timing diagram shown in Figure 2.5 where the gate signals including those for the auxiliary switches are shown for one switching cycle of Q_1 and Q_2 . The commutation states corresponding to each of time periods in Figure 2.5 are illustrated in Figure 2.6. Note that the grid voltage is positive and the grid current is flowing into point A in the illustration. The filter inductor current i_L is assumed to be constant in the analysis. The description of each commutation state is given as following:

$[t_0 \sim t_1]$: Q_1 is on and Q_2 is off. Before the ZVS branch is turned on, the main inductor current is flowing through the channel of Q_1 and Q_4 .

$[t_1 \sim t_2]$: The auxiliary branch is activated by turning on S_2 . The auxiliary inductor is charged by the voltage $V_{dc} - V_{Cf}$. By the end of this period, the auxiliary branch current becomes higher than the main inductor current so that the current at point A is reversed.

[$t_2 \sim t_3$]: This state and the following state happen during the deadtime where g_1 and g_2 are both set as low. After g_1 is set low, the auxiliary inductor starts to resonate with the drain-to-source capacitance of Q_1 and Q_2 until V_{ds,Q_2} reaches zero. The change of the filter inductor current can be neglected due to the relatively large inductance.

[$t_3 \sim t_4$]: The current starts to flow through the body diode of Q_2 since V_{ds,Q_2} has reached zero. The auxiliary inductor starts to be discharged by $-V_{Cf}$. Q_2 can be ZVS turned on before the auxiliary inductor current drops lower than i_L .

[$t_4 \sim t_5$]: Q_2 is ZVS turned on and the current flows through the channel of Q_2 . i_{aux} continues to decrease until it reaches zero and is blocked by the body diode of S_1 . S_2 is turned off at the end of this period.

[$t_5 \sim t_6$]: During the rest of the duty cycle of Q_2 , Q_2 is on and Q_1 is off.

[$t_6 \sim t_7$]: Q_2 is turned off. The filter inductor current starts to discharge and charge the drain-to-source capacitance of Q_1 and Q_2 respectively until V_{ds,Q_1} reaches zero.

[$t_7 \sim t_8$]: The filter inductor current flows through the body diode of Q_1 so that it can be ZVS turned on at the end of deadtime.

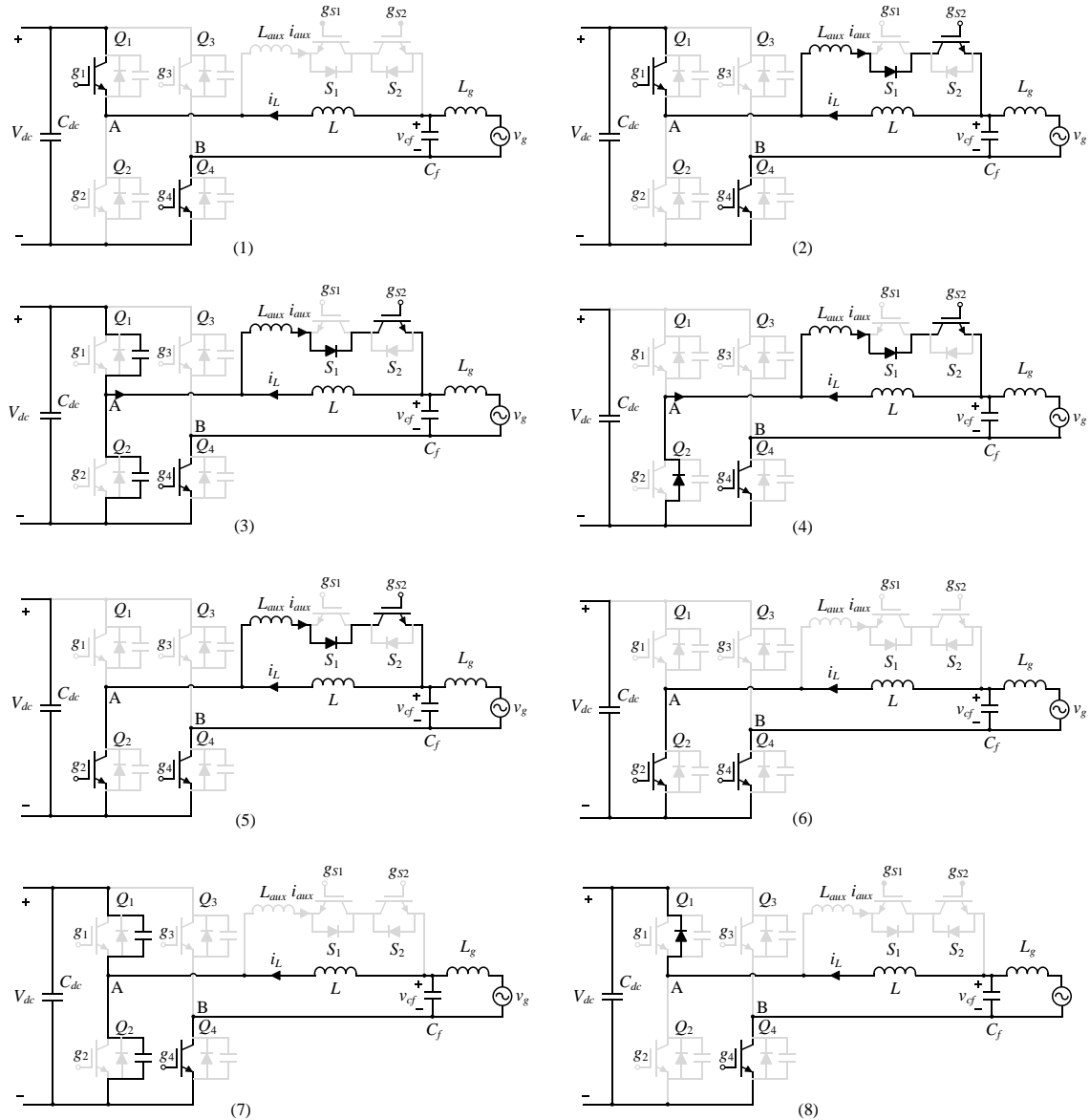


Figure 2.6 Commutation states of the proposed ZVT converter

As can be seen from the circuit operation, the ZVS turn-on is achieved for the main switch Q_2 by changing the current direction at point A before Q_2 is turned on. The other auxiliary switch S_1 is needed when the grid current is flowing out of point A to realize the ZVS turn-on for Q_1 . The switching loss in the auxiliary switch is low since both turn-on and turn-off of the switch are zero-current-switching (ZCS). However, due to the other losses generated by the ZVT scheme, the circuit might need to operate at partial ZVS

condition where the drain to source capacitance of the main switch is not fully discharged in $[t_2 \sim t_3]$. The auxiliary switch timing plays an important role in determining the waveforms in the turn-on transition, thus affects the overall loss saving of the ZVT scheme. The impact of the auxiliary switch timing on the energy loss in the turn-on transition is analyzed in the following section.

2.2 Timing control of the auxiliary switch for optimized loss saving

2.2.1 Cases when grid voltage is low

As shown in Figure 2.7-Figure 2.10, the turn-on transition has different patterns as the turn-on timing of the auxiliary switch changes. The grid side voltage is assumed to be less than half of the dc side voltage in these cases. It can be shown that there will be no more loss saving for Q_2 as the ahead time T_a become larger than that in Figure 2.9. The turn-on loss of Q_2 , turn-off loss of Q_1 and conduction loss in the auxiliary branch are evaluated for case a , b and d to find the relationship between the overall loss saving and the auxiliary switch turn-on timing. Case c can be considered as a special case of case b where the drain to source voltage of Q_2 just drops to zero when its gate signal is turned high. The switching loss of the auxiliary switch is not considered since it is not affected by varying the turn-on timing of the auxiliary switch.

Case a

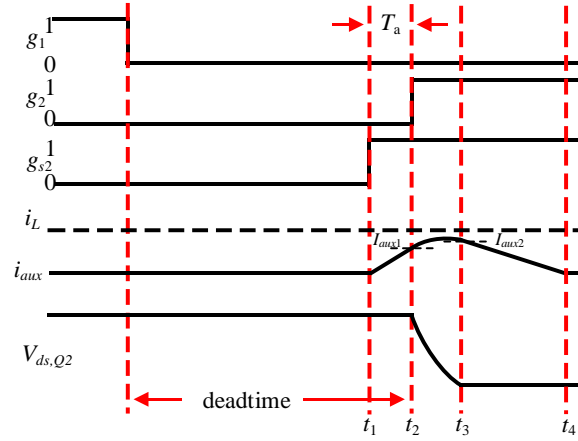


Figure 2.7 Case a of the Q_2 turn-on transition when $v_g < 0.5V_{dc}$

Figure 2.7 shows the first case where the charging time for the auxiliary inductor is low so that i_{aux} cannot reach the magnitude of the main inductor current before Q_2 is turned on. The deadtime between g_1 and g_2 is assumed to be half cycle of the resonant period of the resonance between $C_{ds,Q1}$, $C_{ds,Q2}$ and L_{aux} . The resonant frequency can be calculated as:

$$\omega_r = \sqrt{\frac{1}{2L_{aux}C_{ds}}} \quad (2.1)$$

In the period $[t_1 \sim t_2]$:

$$v_{ds,Q2} = V_{dc} \quad (2.2)$$

$$i_{aux} = \frac{V_{dc} - v_g}{L_{aux}}(t - t_1) \quad (2.3)$$

The RMS value of the auxiliary current of this period can be calculated as:

$$I_{rms1} = \sqrt{\frac{1}{T_a} \int_{t_1}^{t_2} i_{aux}^2 dt} = \frac{I_{aux1}}{\sqrt{3}} \quad (2.4)$$

where

$$I_{aux1} = \frac{V_{dc} - v_g}{L_{aux}} T_a \quad (2.5)$$

The resistive conduction loss in the auxiliary branch during this period can be calculated by:

$$E_1 = I_{rms1}^2 R_{aux} T_a \quad (2.6)$$

where R_{aux} is the total resistance in the loop of i_{aux} , including the resistance of the auxiliary inductor, on-resistance of the auxiliary switch, ESR of the filter capacitor and damping resistor for the LCL filter. Another type of the conduction loss in the auxiliary branch is the diode loss of the anti-parallel diode of S_1 . With the diode forward voltage V_F , the diode loss can be calculated as:

$$E_{D1} = V_F \frac{I_{aux1}}{2} T_a \quad (2.7)$$

In the period $[t_2 \sim t_3]$:

$$v_{ds,Q2} = V_{dc} - V_{dc} \frac{t-t_2}{t_r} \quad (2.8)$$

$$i_{aux} = I_{aux1} + \frac{V_{dc} - v_g}{L_{aux}} (t - t_2) - \frac{V_{dc}}{2t_r L_{aux}} (t - t_2)^2 \quad (2.9)$$

The rise time t_r is the time needed to turn on Q_2 by hard-switching. The auxiliary branch resistive conduction loss in this period is:

$$E_2 = I_{rms2}^2 R_{aux} t_r \quad (2.10)$$

where

$$I_{rms2} = \sqrt{\frac{1}{t_r} \int_{t_2}^{t_3} i_{aux}^2 dt} \quad (2.11)$$

The diode loss of S_1 in this period is:

$$E_{D2} = V_F \int_{t_2}^{t_3} i_{aux} dt = V_F \left(\frac{V_{dc} - v_g}{2L_{aux}} t_r^2 - \frac{V_{dc}}{6t_r L_{aux}} t_r^3 + I_{aux1} t_r \right) \quad (2.12)$$

In the period $[t_3 \sim t_4]$:

$$v_{ds,Q2} = 0 \quad (2.13)$$

$$i_{aux} = I_{aux2} - \frac{v_g}{L_{aux}} (t - t_3) \quad (2.14)$$

where

$$I_{aux2} = I_{aux1} + \frac{V_{dc} - v_g}{L_{aux}} t_r - \frac{V_{dc}}{2t_r L_{aux}} t_r^2 \quad (2.15)$$

The auxiliary branch resistive conduction loss in this period is

$$\begin{aligned} E_3 &= I_{rms3}^2 R_{aux} (t_4 - t_3) = \frac{1}{t_4 - t_3} \int_{t_3}^{t_4} i_{aux}^2 dt R_{aux} (t_4 - t_3) \\ &= \frac{I_{aux2}^3 L_{aux} R_{aux}}{3v_g} \end{aligned} \quad (2.16)$$

The diode loss of S_1 in this period is:

$$E_{D3} = V_F \frac{I_{aux2}^2 L_{aux}}{2v_g} \quad (2.17)$$

The total loss in the auxiliary branch in the entire turn-on transition is the sum of losses in each period:

$$E_{aux} = E_1 + E_2 + E_3 + E_{D1} + E_{D2} + E_{D3} \quad (2.18)$$

The pole current and drain-to-source voltage at the instant when g_2 becomes high (I_{pole}, V_{ds}) have major impact on the turn-on energy loss of Q_2 . Ignoring the impact from other aspects, the turn-on energy loss of Q_2 can be expressed as $E_{on}(I_{pole}, V_{ds})$. Thus, the turn-on loss of Q_2 in the conventional full-bridge converter is $E_{on}(i_L, V_{dc})$ (hard-switching), while the turn-on loss in this case is reduced to:

$$E_{on,Q2} = E_{on}(i_L - I_{aux1}, V_{dc}) \quad (2.19)$$

since the pole current is reduced at instant when g_2 becomes high by the auxiliary circuit.

Case b and case c

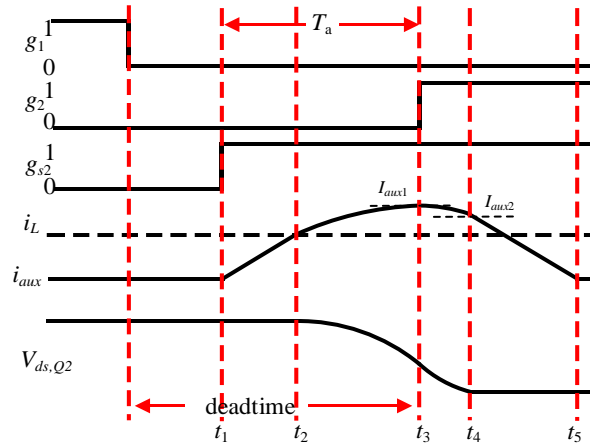


Figure 2.8 Case b of the Q_2 turn-on transition when $v_g < 0.5V_{dc}$

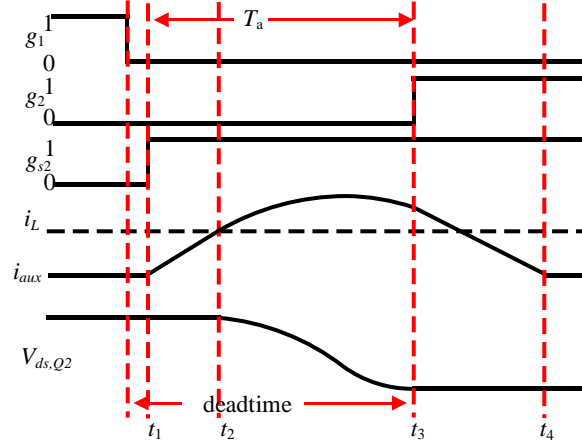


Figure 2.9 Case *c* of the Q_2 turn-on transition when $v_g < 0.5V_{dc}$

As shown in Figure 2.8 and Figure 2.9, the auxiliary inductor current is charged to the value of i_L with larger T_a and starts to resonate with the drain to source capacitor of the main switches until g_2 becomes high. The minimum value of T_a in this case is:

$$T_{amin} = \frac{iL_{aux}}{V_{dc} - v_g} \quad (2.20)$$

Since the grid voltage is lower than half of the dc side voltage, $v_{ds,Q2}$ can be fully discharged by the resonance. Figure 2.9 shows the special case where $v_{ds,Q2}$ just get fully discharged when g_2 becomes high. The value of T_a in this case can be calculated as:

$$T_{amax} = \frac{iL_{aux}}{V_{dc} - v_g} + \frac{\cos^{-1}\left(\frac{v_g}{v_g - V_{dc}}\right)}{\omega_r} \quad (2.21)$$

Thus, Figure 2.8 shows the scenario where

$$T_{amin} < T_a < T_{amax} \quad (2.22)$$

Like what has been done for case *a*, the auxiliary branch conduction losses in each of the periods in case *b* are calculated as follows.

$[t_1 \sim t_2]$:

$$v_{ds,Q2} = V_{dc} \quad (2.23)$$

$$i_{aux} = \frac{V_{dc} - v_g}{L_{aux}}(t - t_1) \quad (2.24)$$

$$t_2 - t_1 = \frac{i_L L_{aux}}{V_{dc} - v_g} \quad (2.25)$$

$$I_{rms1} = \frac{i_L}{\sqrt{3}} \quad (2.26)$$

$$E_1 = I_{rms1}^2 R_{aux} (t_2 - t_1) = \frac{i_L^3 L_{aux} R_{aux}}{3(V_{dc} - v_g)} \quad (2.27)$$

$$E_{D1} = \frac{1}{2} V_F I_L (t_2 - t_1) = \frac{i_L^2 V_F L_{aux}}{2(V_{dc} - v_g)} \quad (2.28)$$

$[t_2 \sim t_3]$:

$$v_{ds,Q2} = v_g + (V_{dc} - v_g) \cos(\omega_r(t - t_2)) \quad (2.29)$$

$$V_{ds1} = v_g + (V_{dc} - v_g) \cos(\omega_r(t_3 - t_2)) \quad (2.30)$$

$$i_{aux} = i_L + \frac{V_{dc} - v_g}{L_{aux} \omega_r} \sin(\omega_r(t - t_2)) \quad (2.31)$$

$$I_{aux1} = i_L + \frac{V_{dc} - v_g}{L_{aux} \omega_r} \sin(\omega_r(t_3 - t_2)) \quad (2.32)$$

$$t_3 - t_2 = T_a - \frac{i_L L_{aux}}{V_{dc} - v_g} \quad (2.33)$$

$$I_{rms2} = \sqrt{\frac{1}{t_3 - t_2} \int_{t_2}^{t_3} i_{aux}^2 dt} \quad (2.34)$$

$$E_2 = I_{rms2}^2 R_{aux} (t_3 - t_2) \quad (2.35)$$

$$\begin{aligned} E_{D2} &= V_F \int_{t_2}^{t_3} i_{aux} dt \\ &= V_F \left(i_L(t_3 - t_2) - \frac{V_{dc} - v_g}{L_{aux} \omega_r^2} \cos(\omega_r(t_3 - t_2)) + \frac{V_{dc} - v_g}{L_{aux} \omega_r^2} \right) \end{aligned} \quad (2.36)$$

[$t_3 \sim t_4$]:

$$v_{ds,Q2} = V_{ds1} - \frac{V_{dc}}{t_r} (t - t_3) \quad (2.37)$$

$$i_{aux} = I_{aux1} + \frac{V_{ds1} - v_g}{L_{aux}} (t - t_3) - \frac{V_{dc}}{2L_{aux} t_r} (t - t_3)^2 \quad (2.38)$$

$$t_4 - t_3 = \frac{V_{ds1}}{V_{dc}} t_r \quad (2.39)$$

$$I_{aux2} = I_{aux1} + \frac{V_{ds1} - v_g}{L_{aux}} (t_4 - t_3) - \frac{V_{dc}}{2L_{aux} t_r} (t_4 - t_3)^2 \quad (2.40)$$

$$I_{rms3} = \sqrt{\frac{1}{t_4 - t_3} \int_{t_3}^{t_4} i_{aux}^2 dt} \quad (2.41)$$

$$E_3 = I_{rms3}^2 R_{aux} (t_4 - t_3) \quad (2.42)$$

$$E_{D3} = V_F \int_{t_3}^{t_4} i_{aux} dt \quad (2.43)$$

[$t_4 \sim t_5$]:

$$v_{ds,Q2} = 0 \quad (2.44)$$

$$i_{aux} = I_{aux2} - \frac{v_g}{L_{aux}}(t - t_4) \quad (2.45)$$

$$I_{rms4} = \frac{I_{aux2}}{\sqrt{3}} \quad (2.46)$$

$$E_4 = I_{rms4}^2 R_{aux}(t_5 - t_4) = \frac{I_{aux2}^3 L_{aux} R_{aux}}{3v_g} \quad (2.47)$$

$$E_{D4} = \frac{V_F I_{aux2}}{2}(t_5 - t_4) = \frac{V_F I_{aux2}^2 L_{aux}}{2v_g} \quad (2.48)$$

$$E_{aux} = E_1 + E_2 + E_3 + E_4 + E_{D1} + E_{D2} + E_{D3} + E_{D4} \quad (2.49)$$

The turn-on loss of Q_2 in this case only contains the capacitive loss since pole current is flowing out of point A when gate signal g_2 becomes high. The corresponding turn-on loss can be expressed as:

$$E_{on,Q2} = E_{on}(0, V_{ds1}) \quad (2.50)$$

where V_{ds1} is calculated in (2.30) which is the drain to source voltage of Q_2 when g_2 becomes high. Note that the turn-on loss is fully eliminated in the case shown in Figure 2.9 where V_{ds1} equals to zero.

Case d

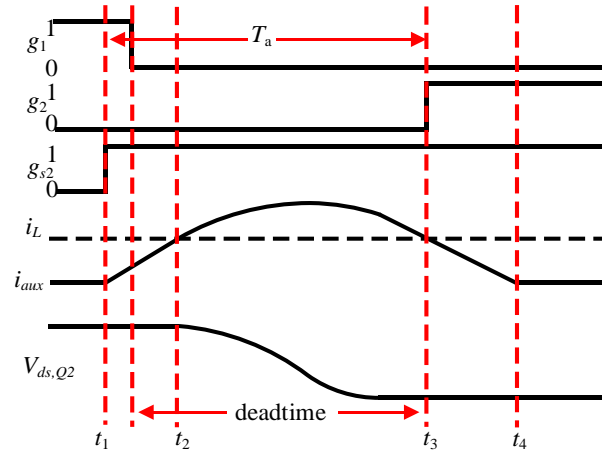


Figure 2.10 Case *d* of the Q_2 turn-on transition when $v_g < 0.5V_{dc}$

Figure 2.10 shows the scenario when T_a is larger than the value given in (2.21). The time instant t_2 when the auxiliary inductor current reaches i_L stays within the deadtime in this scenario. The auxiliary current will be higher than i_L at the end of the deadtime when g_2 becomes high. It can be noticed that the waveform of i_{aux} and $v_{ds,Q2}$ in the figure are just the shifted waveform of Figure 2.9. Thus, the losses in this case are identical to that of case *c*. However, as T_a keeps increasing, the auxiliary current can be charged to a higher value than i_L when it surpasses i_L before Q_1 is turned off. The auxiliary branch conduction loss will become higher in this case, however, the turn-on loss of Q_2 stays the same. Moreover, it will induce turn-off loss in Q_1 which does not exist previously since the pole current hasn't been reversed when Q_1 is turned off. Based on the analysis, the optimized auxiliary switch turn-on timing should be searched in the range given by (2.22).

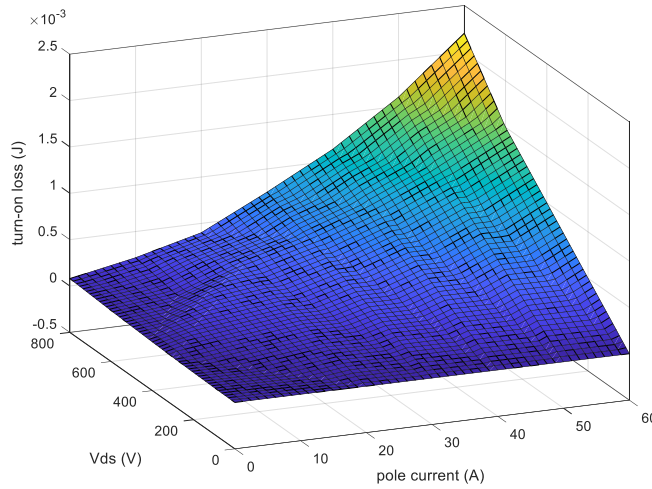


Figure 2.11 Turn-on energy loss of C2M0025120D SiC MOSFET

The data of the turn-on loss is commonly available in the datasheet of a switch for multiple voltage and current conditions. A lookup table can be created from the available data based on curve fitting. The turn-on loss curve of the C2M0025120D SiC MOSFET extracted from its datasheet is shown in Figure 2.11. Another important type of loss in the auxiliary circuit is the core loss in the auxiliary inductor. Knowing a specific inductor which is used as the auxiliary inductor, the flux density variation ΔB can be determined based on the peak value of the auxiliary branch current during the transition. The corresponding core loss can be calculated by

$$E_3 = K_{fe} \Delta B^\alpha f_{sw}^\beta \quad (2.51)$$

where K_{fe} , α , β can be determined based on the characteristic curve provided for the magnetic core. Considering the main switch turn-on loss, auxiliary inductor copper loss, core loss and the diode conduction loss, the combined turn-on transition loss plot with respect to the auxiliary switch timing can be generated. Figure 2.12 shows the plot generated based on the parameters given in Table 2.1. Note that the turn-on loss of the

auxiliary switch is excluded in the analysis since it doesn't depend on the auxiliary switch turn-on timing.

Table 2.1 Parameters for loss calculations in Figure 2.12

Auxiliary inductor L_{aux}	440 nH
Magnetic core of the auxiliary inductor	13mm×3mm×9mm 3F36 ferrite core
Main switch drain-to-source capacitance C_{ds}	220 pF
Auxiliary branch resistance R_{aux}	100 mΩ
S_1 diode forward voltage V_F	1.5 V
Main switch rise time t_r	16 ns
Dc side voltage V_{dc}	400 V
Grid voltage v_g	150 V
Main inductor current i_L	7.7 A

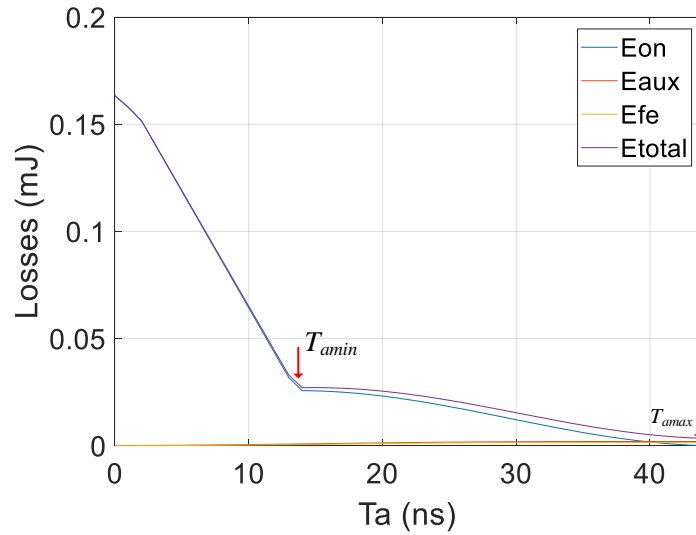


Figure 2.12 Losses in the turn-on transition as T_a increases when $v_g < 0.5V_{dc}$

2.2.2 Cases when grid voltage is high

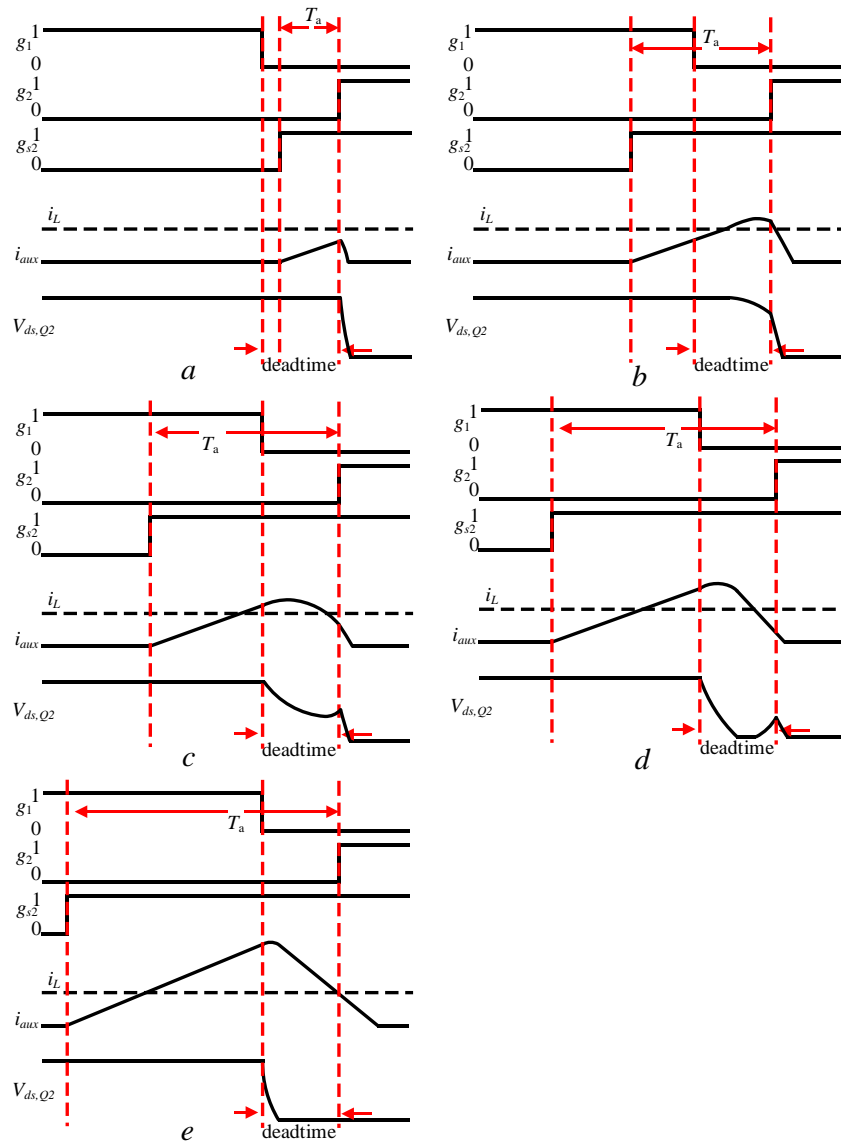


Figure 2.13 Turn-on transitions when $v_g > 0.5V_{dc}$

The scenarios become different when grid voltage is higher than half of the dc side voltage. This is because $v_{ds,Q2}$ cannot get fully discharged by the self-resonance as what happens in the low grid voltage cases. The scenarios corresponding to different value of T_a for the high grid voltages are illustrated in Figure 2.13. The boundaries between cases in the figure is:

$$\text{case a: } T_a < \frac{i_L L_{aux}}{V_{dc} - v_g} \quad \text{case b: } \frac{i_L L_{aux}}{V_{dc} - v_g} < T_a < \frac{i_L L_{aux}}{V_{dc} - v_g} + \frac{\pi}{\omega_r}$$

$$\text{case c: } \frac{i_L L_{aux}}{V_{dc} - v_g} + \frac{\pi}{\omega_r} < T_a < \frac{i_L L_{aux}}{V_{dc} - v_g} + \frac{\pi}{\omega_r} + \sqrt{\frac{V_{dc}(2v_g - V_{dc})}{(V_{dc} - v_g)^2 \omega_r^2}}$$

$$\text{case d and e: } T_a > \frac{i_L L_{aux}}{V_{dc} - v_g} + \frac{\pi}{\omega_r} + \sqrt{\frac{V_{dc}(2v_g - V_{dc})}{(V_{dc} - v_g)^2 \omega_r^2}}$$

The losses in each of the scenarios are calculated in the same way as what have been presented for the low grid voltage cases. The analytical derivation of each segment of the waveforms is given in the Appendix. The turn-on transition loss plot is shown in Figure 2.14. The boundary points of case *c* are indicated on the plot. The parameters used for the plot are given in Table 2.2.

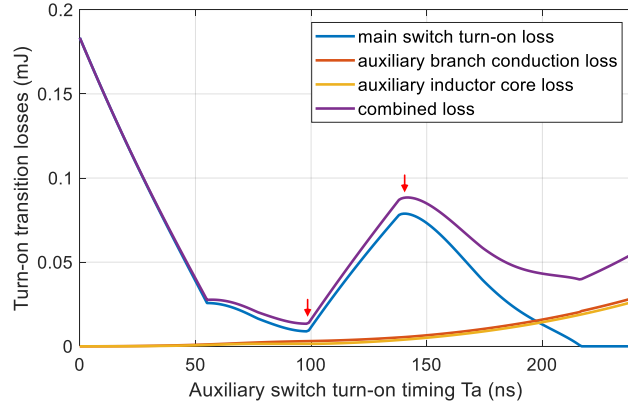


Figure 2.14 Losses in the turn-on transition as T_a increases when $v_g > 0.5V_{dc}$

Table 2.2 Parameters for loss calculations in Figure 2.14

Auxiliary inductor L_{aux}	440 μ H
Magnetic core of the auxiliary inductor	13mm \times 3mm \times 9mm 3F36 ferrite core
Main switch drain to source capacitance C_{ds}	220 pF
Auxiliary branch resistance R_{aux}	100 m Ω
S_1 diode forward voltage V_F	1.5 V
Main switch rise time t_r	16 ns
Dc side voltage V_{dc}	400 V
Grid voltage v_g	300 V
Main inductor current i_L	15.4 A

Figure 2.15 shows the combined loss value for multiple grid voltages. It can be found that the optimized cases always stay around the boundary between the cases *b* and *c*. As shown in Figure 2.14, the turn-on loss of Q_2 has been reduced by the self-resonance while the auxiliary branch conduction loss is relatively low at this point. It also shows that even though the turn-on loss can be further reduced in cases *d* and *f*, the total loss becomes more because of higher auxiliary branch loss and turn-off loss of Q_1 . Based on the analysis, the value of T_a should be adapting in the line period and expression for the case when the converter absorbs power from grid at unity power factor can be written as:

$$T_a = \frac{k_1 \cos(\theta)}{1 - m \cos(\theta)} + k_2 \quad (2.52)$$

where θ is the angle of grid voltage. A good guess of the parameters can be evaluated by:

$$T_a = \frac{I_L \cos(\theta) L_{aux}}{V_{dc} - V_{gpk} \cos(\theta)} + \frac{\pi}{\omega_r} \quad (2.53)$$

by which the circuit operates at the boundary between case *b* and case *c* in Figure 2.13 and the early stage in Figure 2.10.

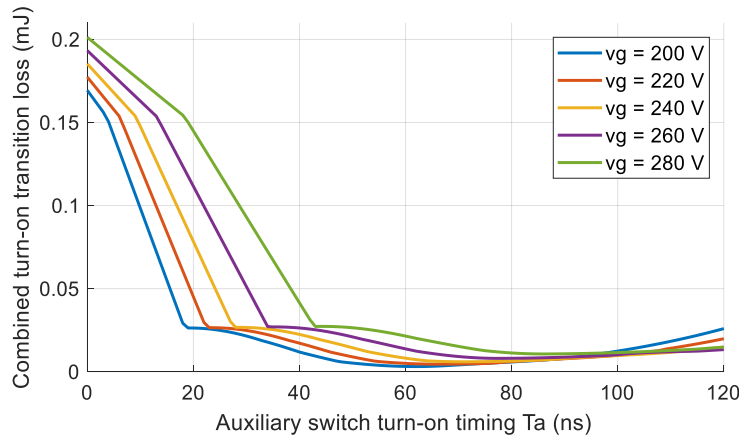


Figure 2.15 Loss in the turn-on transition as T_a increases for different grid voltages

2.3 System design of a 3.3 kW prototype of the proposed circuit

The system design of a prototype of the proposed circuit is introduced in this section including the grid current filter design, the auxiliary inductor design and the control system design. The grid voltage and the dc side voltage of the prototype are 240 V_{rms} and 400 V respectively. The target power rating of the prototype is 3.3 kW. The target switching frequency of the main switches in the high frequency leg is 400 kHz.

2.3.1 LCL filter design

A LCL filter is used to attenuate the harmonic components in the grid current so that the current THD can meet the requirement in standard IEC 61000-3-2 and IEEE 1547. The filter parameters are designed by following the step-by-step procedure as below:

1. Decide the value of converter side filter L

The inductance of the converter side filter can be decided based on the desired ripple amplitude in the inductor. Given 30% current ripple tolerance in the first stage of the LCL filter, L can be determined by:

$$\frac{V_{dc}}{f_{sw}L} m \sin(\omega t) (1 - m \sin(\omega t)) \leq 0.3I_{gpk} \quad (2.54)$$

The resulting inductance is 50 uH for the converter side inductor based on the prototype specifications.

2. Designing the resonant frequency of the LCL filter

The resonant frequency of the LCL filter given as (2.55) should be included in a range between ten times the line frequency and half of the switching frequency [35]. Based on

the prototype switching frequency, the resonant frequency of the LCL filter is picked as 130 kHz.

$$\omega_{LCL} = \sqrt{\frac{1}{C_f} \left(\frac{1}{L} + \frac{1}{L_g} \right)} \quad (2.55)$$

3. Determine the current attenuation by the second stage of the LCL filter

According to [35], the second stage current ripple reduction for the switching frequency component by the LCL filter can be evaluated by:

$$\frac{i_g(h_{sw})}{i_L(h_{sw})} \approx \frac{1}{L_g C_f |\omega_{sw}^2 - \omega_{LCL}^2|} \quad (2.56)$$

The ratio is designed to be 10% in this case so that the ripple in the grid side current can be reduced to approximately 3%. With the constraints given in (2.55) and (2.56), the value of L_g and C_f can be finalized, which is 6.8 uH and 0.22 uF.

2.3.2 Determine the auxiliary inductance value

As given in (2.1), the inductance of the auxiliary inductor determines the resonant speed of the main switch voltage and auxiliary current during the turn-on transition. The analysis given in the previous section implies that the loss saving from the ZVT circuit will be less if the deadtime of the main switches is too small as compared to this resonant time. A special value is $\frac{\pi}{2\omega_r}$ which is the shortest time to fully discharge the drain to source capacitance of the main switch without excessive auxiliary current among all the cases. It can be shown that the losses will always be larger if the deadtime is smaller than this value since higher auxiliary current is needed since the main switch needs to get discharged in a

shorter time. Thus, the following constraint should be complied to ensure the benefit of the ZVT circuit:

$$\frac{\pi}{2\omega_r} < \frac{0.05}{f_{sw}} \quad (2.57)$$

where the deadtime is assumed to be no larger than 5% of the switching period. The higher bound of the auxiliary inductance can be calculated as 14 uH based on (2.57) if the switch C2M0025120D is used for the main switches. The higher bound of the auxiliary inductance can also be determined based on the requirement of continuous conduction mode (CCM) operation of the inverter. As the inductance value increases, the duration of the auxiliary circuit current becomes a larger portion of the switching period. The current waveform becomes equivalent to discontinuous conduction mode (DCM) operation when

$$L_{aux_CRM} = \frac{m(1-m)V_{dc}}{I_g f_s} \quad (2.58)$$

However, the desired auxiliary circuit operation should limit the impact to the normal CCM operation as low as possible, thus L_{aux} should be much less than (2.58) so that switch node current is only manipulated in a very short duration at the switching transitions. Thus, the upper boundary of L_{aux} can be determined by

$$L_{aux} < \frac{1}{5} L_{aux_CRM} = \frac{m(1-m)V_{dc}}{5I_g f_s} \quad (2.59)$$

The resulting higher bound of L_{aux} is 1.8 uH. The lower boundary of L_{aux} is determined from a perspective of the actual control implementation. Given a processor frequency of the digital controller f_{dsp} , the lower limit of L_{aux} can be determined by

$$L_{aux} > \frac{5(1-m)V_{dc}}{I_g f_{dsp}} \quad (2.60)$$

That is, the variation range of the first term of (2.53) in a line cycle is at least five clock cycles of the digital controller. Otherwise it is nearly impossible to effectively implement the variable turn-on timing by the controller. The lower bound value corresponding to a 150 MHz DSP frequency is 140 nH.

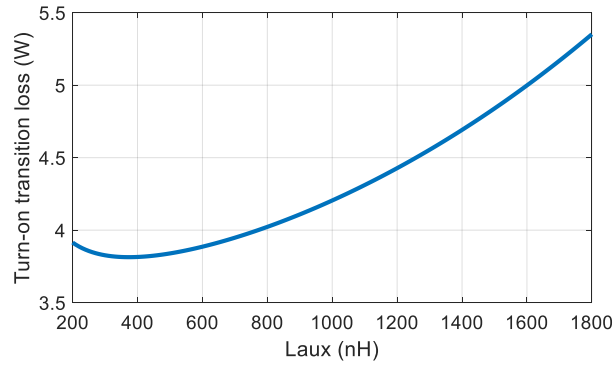


Figure 2.16 Turn-on loss plot with respect to L_{aux}

By using the auxiliary switch timing given in (2.53), the combined turn-on power loss (excluding the switching loss of the auxiliary switch) can be evaluated along the changing grid side voltage. The flux density variation, winding resistance of the auxiliary inductor will change as the inductance value changes. The core loss and conduction loss will change accordingly. Given the magnetic core, the maximum auxiliary inductor current in the line cycle and the maximum allowable flux density, the number of turns of the auxiliary inductor can be determined by

$$n = \frac{L_{aux} i_{max}}{B_{max} A_C} = \frac{L_{aux}}{B_{max} A_C} \left(I_g + \frac{V_{dc}(1-m)}{L_{aux} \omega_r} \right) \quad (2.61)$$

The flux density elsewhere then can be calculated by

$$\Delta B = \frac{B_{max}}{i_{max}} i_{aux_pk} = \frac{B_{max}}{i_{max}} \left(I_g |\sin(\theta)| + \frac{V_{dc}(1-m|\sin(\theta)|)}{L_{aux}\omega_r} \right) \quad (2.62)$$

The winding resistance can be calculated by

$$R_{L_{aux}} = \frac{\rho M L T n^2}{W_A k} \quad (2.63)$$

which is part of the auxiliary branch resistance R_{aux} . The combined turn-on transition loss then can be calculated as what has been done in the previous section for the entire fundamental cycle and integrated to get the total value. As shown in Figure 2.16, the optimized L_{aux} is found to be around 400 nH for the given specification.

2.3.3 Device stress of S_1 and S_2

As long as small L_{aux} is used, the current stress of the auxiliary switches can be extremely low. The RMS value of the auxiliary branch current can be calculated based on the current waveform. Considering the resonance between L_{aux} and the parasitic capacitance of S_1 and S_2 when the corresponding main switch turns off (e.g. when Q_2 turns off in the positive half cycle), the undamped resonance peak of the auxiliary switch voltage can be calculated as

$$V_{ds,max} = V_{dc} - |v_g| + \sqrt{(V_{dc} - |v_g|)^2 + v_g^2} \quad (2.64)$$

The worst case happens at the zero-crossing of the input voltage in which the auxiliary switch voltage can become as high as twice the output voltage. The actual voltage stress is lower considering the damping effect and limited turn-off speed of the main switch.

2.3.4 Control system of the converter

The control system structure of the proposed circuit is shown in Figure 2.17. The system is synchronized with the grid voltage through a PLL. The grid current is regulated through a current controller. The gate signal for the main switches are generated based on the controller output and hybrid PWM modulation. The gate signal for the auxiliary switches are generated based on the duty and the timing control described in section 2.3. The generation of the auxiliary switch gate pulses based on the calculated timing values is illustrated in Figure 2.18.

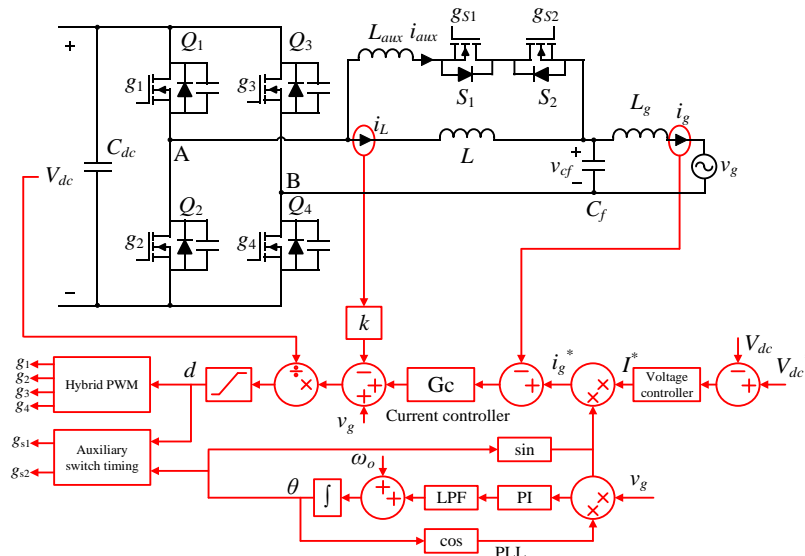


Figure 2.17 Control system of the proposed converter

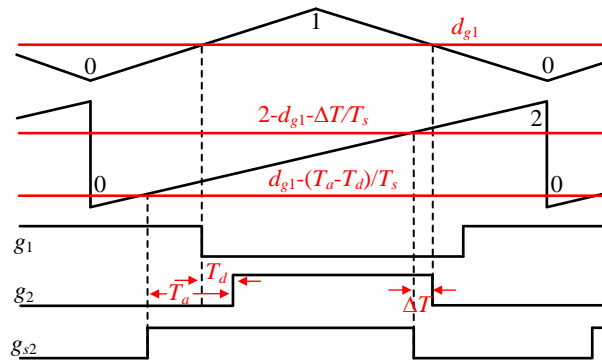


Figure 2.18 Implementation of the auxiliary switch timing

The bandwidth of the PLL is designed as 3 Hz with a PI controller and a low-pass filter. The transfer function of the controller is:

$$G_{pll} = \left(\frac{0.018}{s} + 0.057 \right) \left(\frac{2\pi 5}{s + 2\pi 5} \right) \quad (2.65)$$

The open loop transfer function of the PLL is

$$G_{op} = \frac{340}{s} \left(\frac{0.018}{s} + 0.057 \right) \left(\frac{2\pi 5}{s + 2\pi 5} \right) \quad (2.66)$$

and the corresponding bode plot is shown in Figure 2.19.

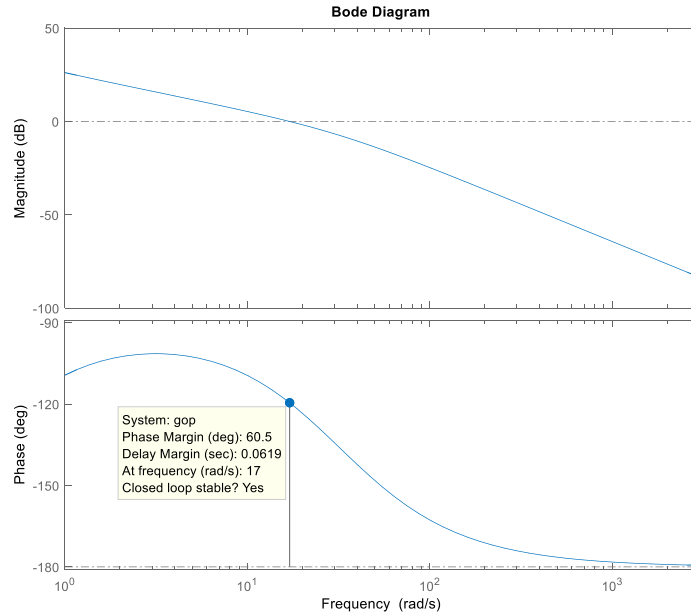


Figure 2.19 Bode plot of the PLL

The current controller includes a PI controller, an active damping feedback and the grid voltage feedforward. The active damping technique [36] damps out the resonant peak in the current loop which is introduced by LCL filter. The passive damping scheme by adding resistance in the real circuit is not used in the design because it will add extra loss

to the converter. With the active damping and the grid voltage feedforward, the plant model of the current loop becomes:

$$\begin{bmatrix} \dot{i}_L \\ \dot{i}_g \\ \dot{v}_{Cf} \end{bmatrix} = \begin{bmatrix} -\frac{K}{L} & 0 & -\frac{1}{L} \\ 0 & 0 & \frac{1}{L_g} \\ \frac{1}{C_f} & -\frac{1}{C_f} & 0 \end{bmatrix} \begin{bmatrix} i_L \\ i_g \\ v_{Cf} \end{bmatrix} + \begin{bmatrix} \frac{1}{L} \\ 0 \\ 0 \end{bmatrix} y_{PI} \quad (2.67)$$

The bandwidth of the current loop is designed as 1000 Hz. A gain of 0.8 is used for the active damping term. The transfer function of the PI controller is:

$$G_{PI} = \frac{5530}{s} \quad (2.68)$$

The bode plot of the current loop is shown in Figure 2.20.

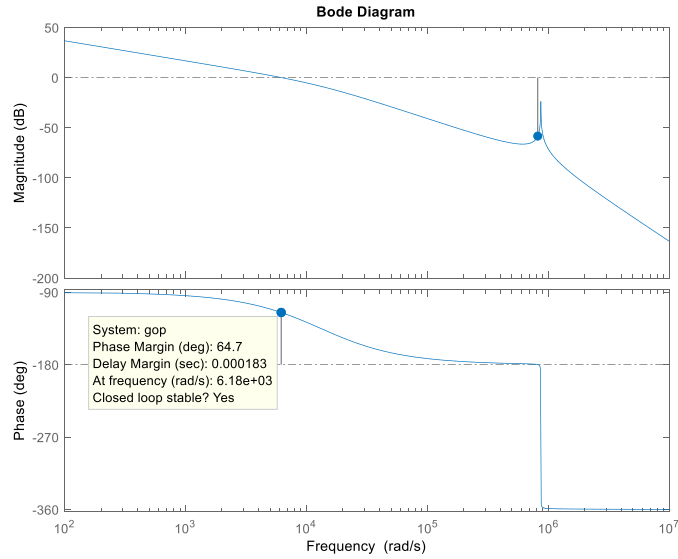


Figure 2.20 Bode plot of the current control loop

2.4 Hardware implementation and experimental results

2.4.1 Hardware prototype development

Table 2.3 Prototype specifications

Grid voltage (v_g)	240 Vrms
Dc side voltage (V_{dc})	400 V
Converter power rating	3.3 kW
DC-link capacitor	2000 μ F
Filter inductor (L)	54.8 μ H
Filter inductor (L_g)	6.8 μ H
Filter capacitor (C_f)	220 nF
Auxiliary inductor (L_{aux})	440 nF
Switching frequency	400 kHz

The proposed circuit has been validated through hardware experiment. A 3.3 kW prototype has been built with the specifications given in Table 2.3. The Cree SiC MOSFET C2M0025120D is used for both the main switches and auxiliary switches. A SiC schottky diode is placed in parallel with each of the switches in order to reduce the diode reverse recovery loss. 3F36 ferrite core and litz wire are used to make the main filter inductor. The digital controller TI TMS320F28335 is used for implementing the real-time control of the circuit. The actual hardware built based on the design is shown in Figure 2.21-Figure 2.23. The circuit schematic and PCB layout of the circuit board are given in the Appendix.

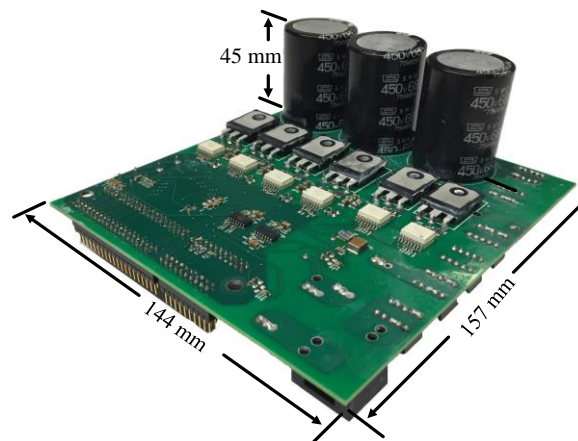


Figure 2.21 Dimensions of the ZVT full-bridge converter prototype



Figure 2.22 Photograph of the ZVT full-bridge converter prototype

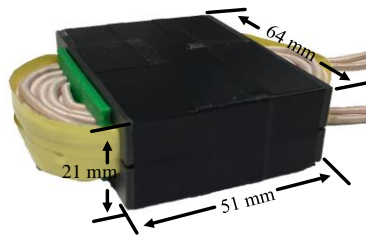


Figure 2.23 Dimensions of the main filter inductor

2.4.2 Experiment results

The line frequency waveforms of the converter operating in the inverter and PFC modes are shown in Figure 2.24 and Figure 2.25 respectively. The experimental result shows that the grid current is well regulated. The THD of the grid current is less than 5% in both cases. Note that the patterns of the auxiliary current are different since the auxiliary circuit takes care of the ZVS turn-on for different switches in each case. The gate voltage of all the switches in PFC mode are shown in Figure 2.26. As defined by the hybrid PWM modulation, Q_1 and Q_2 switch at 400 kHz while Q_3 and Q_4 switch at line frequency. The auxiliary switch S_1 only switches in the negative half cycle for realizing the ZVS of Q_1 . The auxiliary switch S_2 only switches in the positive half cycle for realizing the ZVS of Q_2 .

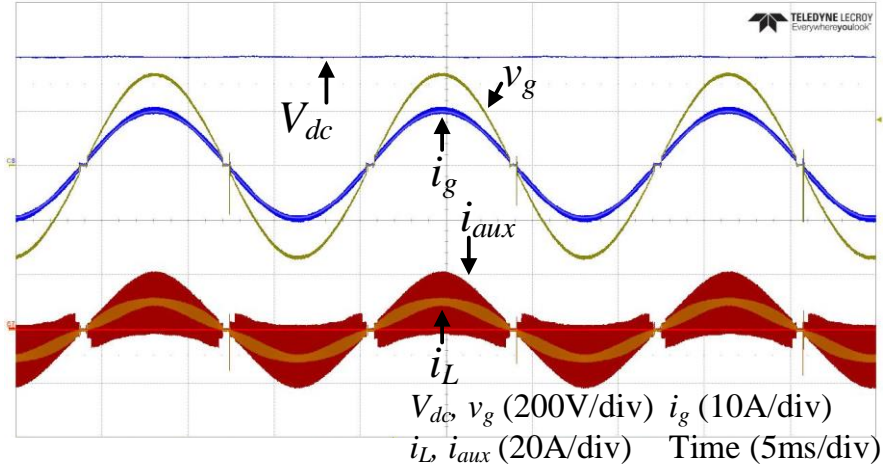


Figure 2.24 Fundamental waveforms in inverter mode

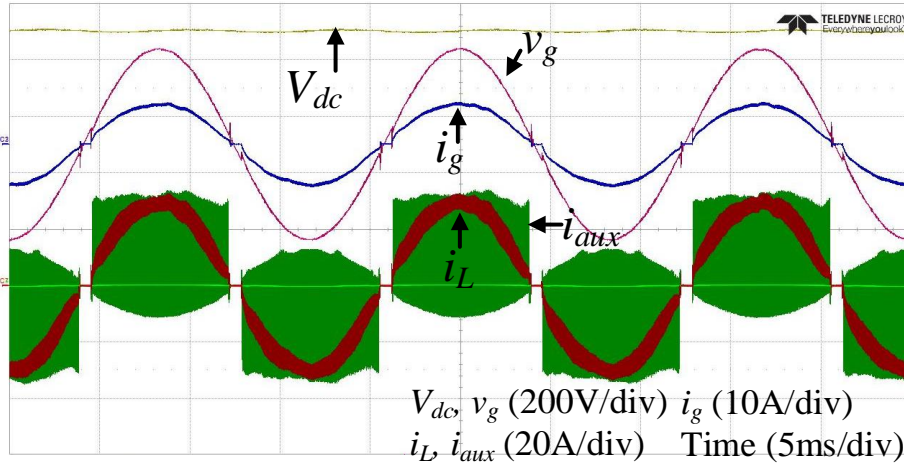


Figure 2.25 Fundamental waveforms in PFC mode

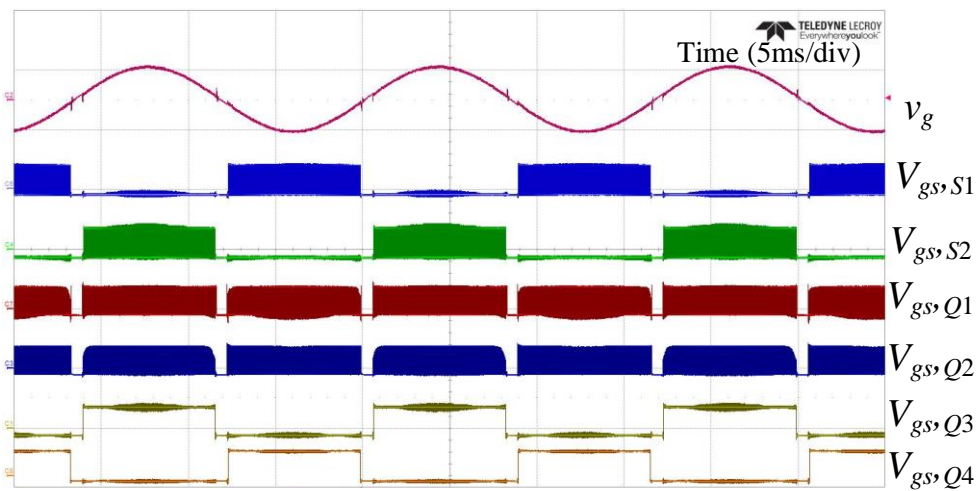


Figure 2.26 Gate signals for the main switches and auxiliary switches in PFC mode

The switching cycle waveforms are shown in Figure 2.27 and Figure 2.28. Figure 2.27 shows the ZVS turn-on transition which is very similar to Figure 2.9 in the analysis. The drain to source capacitance of the main switch is fully discharged before its gate voltage is turned high. Thus, the turn-on loss of the main switch is fully eliminated. Figure 2.28 shows the same waveforms in several switching cycles. It shows that both turn-on and turn-off of the auxiliary switch are ZCS. Thus, the switching loss of the auxiliary switches is very low even with the same switching frequency as the main switches. The auxiliary switches drain-to-source voltage are shown in Figure 2.29. Due to damping effect in the circuit, the maximum resonant peak voltage is less than 600 V for the auxiliary switches which happens near the peak of the grid voltage.

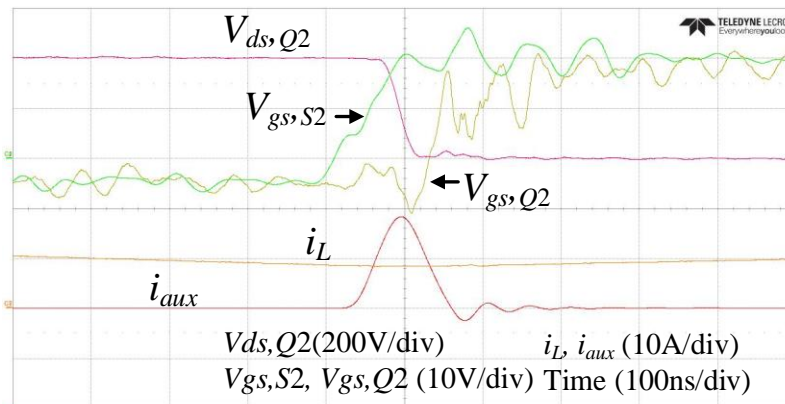


Figure 2.27 ZVS turn-on transition waveforms

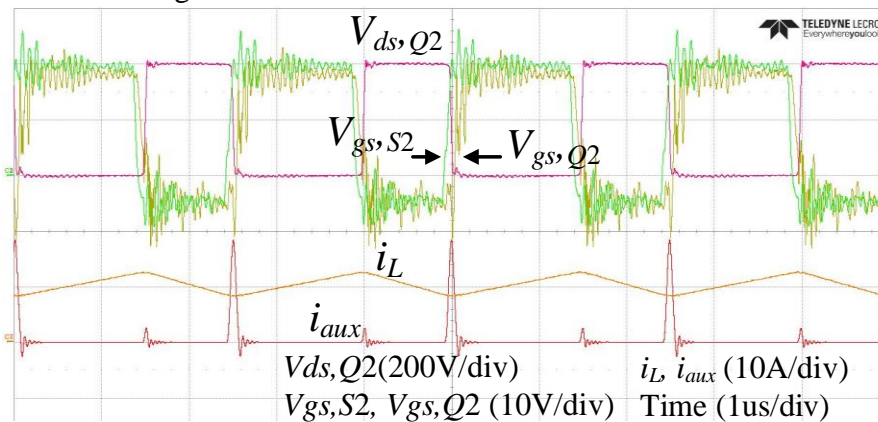


Figure 2.28 Switching cycle waveforms

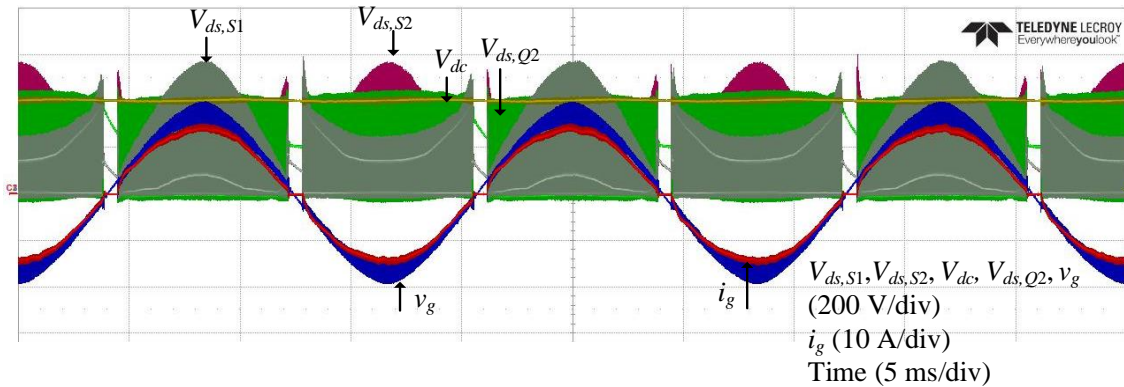


Figure 2.29 Auxiliary switch voltage stress

As shown in Figure 2.30, the converter efficiency has been measured through the YOKOGAWA WT3000 power analyzer. The efficiency curve of the proposed circuit and the conventional full-bridge converter are shown in Figure 2.31. The results show that the proposed circuit has higher efficiency than the conventional full-bridge converter over a wide range of operating powers. The peak efficiency of the proposed circuit is obtained at 2 kW. The circuit efficiency is 98.53% while the conventional full-bridge converter efficiency is 96.57%. The total loss is reduced from 68.6 W to 32.88 W which corresponds to a 52% loss reduction. A loss breakdown shown in Figure 2.32 and Figure 2.33 illustrates the estimated losses for each part of the converter. The total value of the estimated losses is close to the measured value in the experiment.



Figure 2.30 Circuit efficiency measurement at 2.4 kW

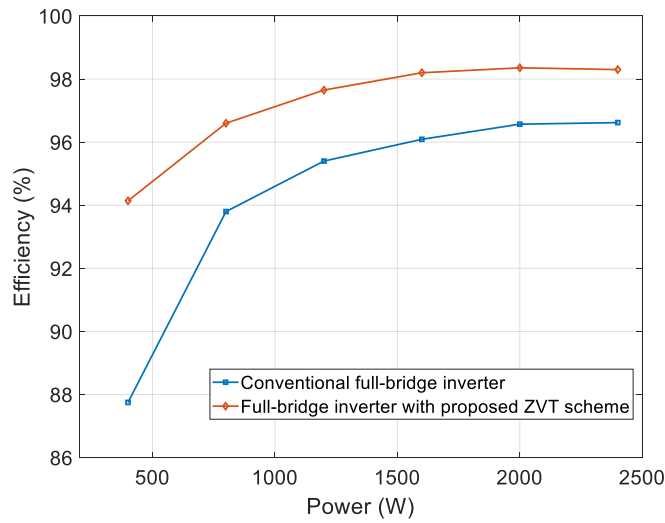


Figure 2.31 Efficiency curve with and without the proposed ZVT technique

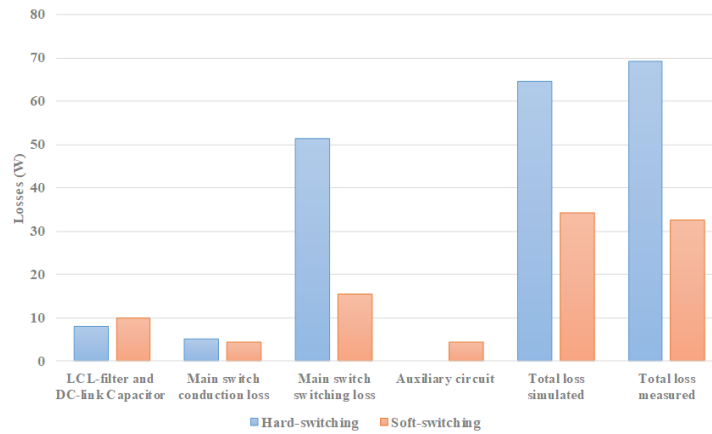


Figure 2.32 Loss breakdown of the proposed the circuit and conventional full-bridge converter

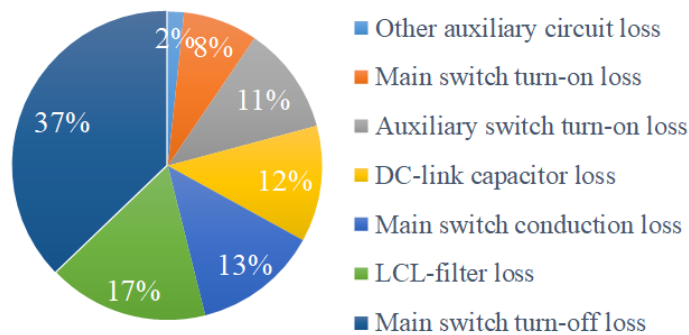


Figure 2.33 Detailed loss breakdown of the proposed circuit

The auxiliary switch timing analysis is also validated through experiments. Low and high grid side voltage scenarios are emulated by connecting the grid terminal to a dc

voltage source. The circuit operates as dc-dc converter in the experiment and the efficiencies are measured for different auxiliary switching timings. The efficiency curve for low grid side voltage is shown in Figure 2.34. The turn-on transition waveforms corresponding to three points on the curve are shown in Figure 2.35 – Figure 2.37. The experiment results match with the analysis given in Figure 2.7, Figure 2.9 and Figure 2.10.

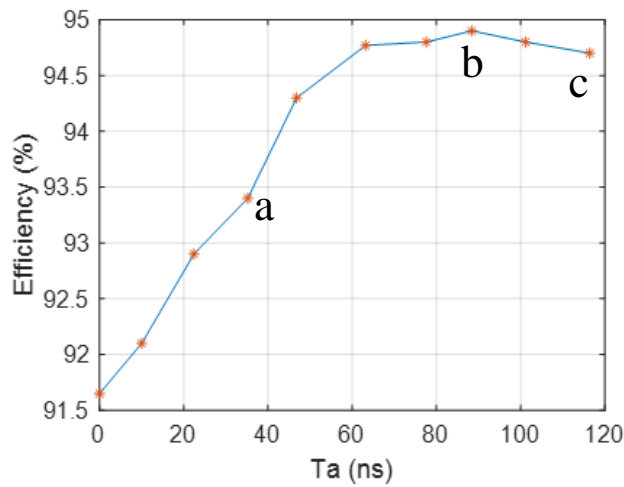


Figure 2.34 Efficiency vs Ta when $V_{dc} = 400\text{ V}$ $v_g = 100\text{ V}$ $i_g = 7.7\text{ A}$

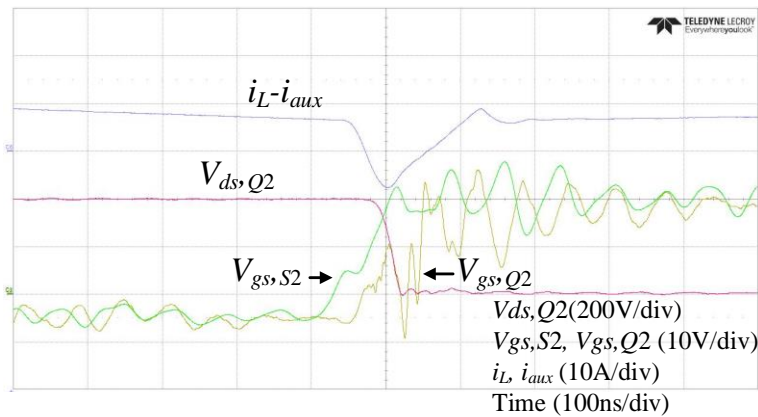


Figure 2.35 Turn-on transition corresponding to point a in Figure 2.34

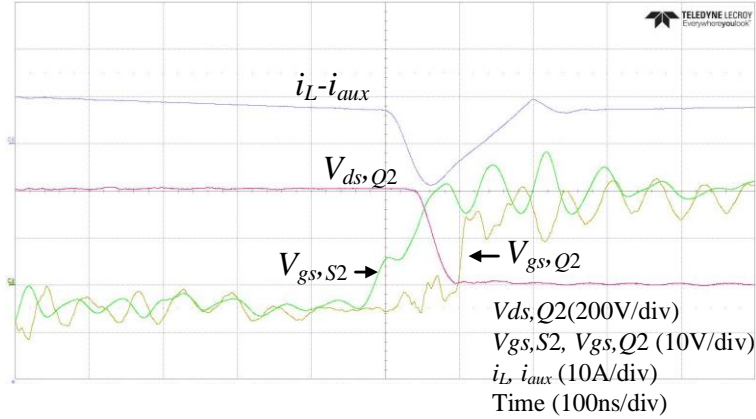


Figure 2.36 Turn-on transition corresponding to point b in Figure 2.34

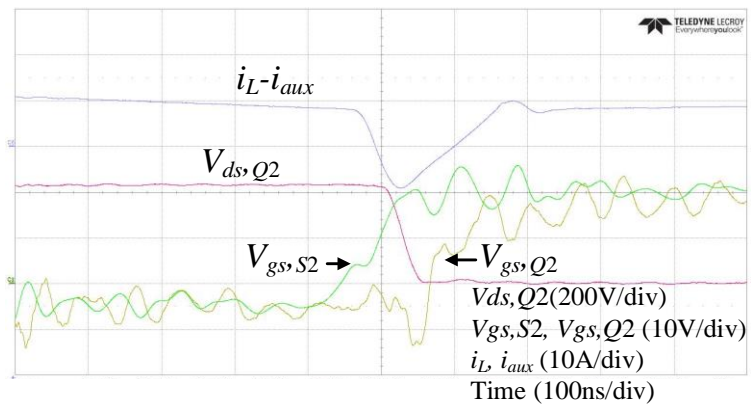


Figure 2.37 Turn-on transition corresponding to point c in Figure 2.34

The efficiency curve for high grid side voltage is shown in Figure 2.38. The turn-on transition waveforms corresponding to three points on the curve are shown in Figure 2.39 – Figure 2.41. The experiment results match with the analysis given in Figure 2.13.

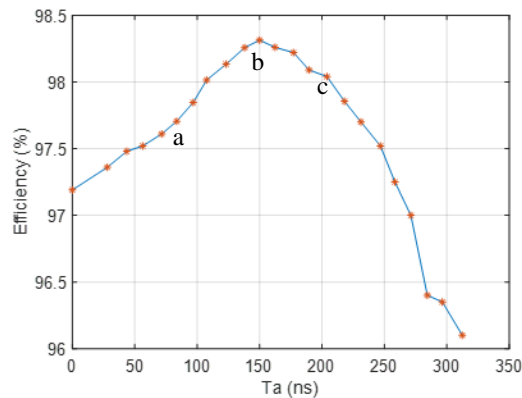


Figure 2.38 Efficiency vs Ta when $V_{dc} = 400 \text{ V}$ $v_g = 300 \text{ V}$ $i_g = 7.7 \text{ A}$

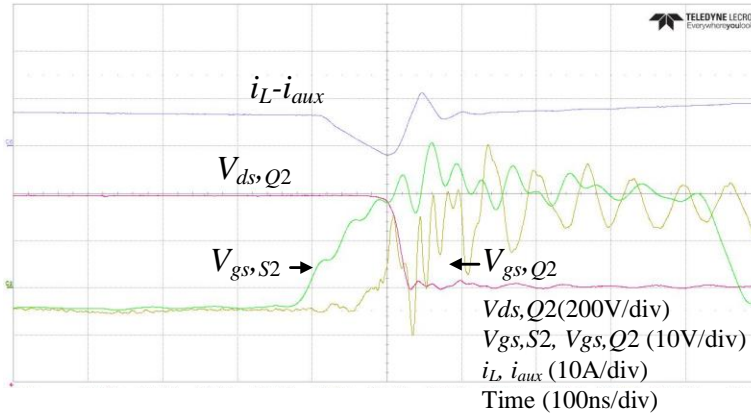


Figure 2.39 Turn-on transition corresponding to point a in Figure 2.38

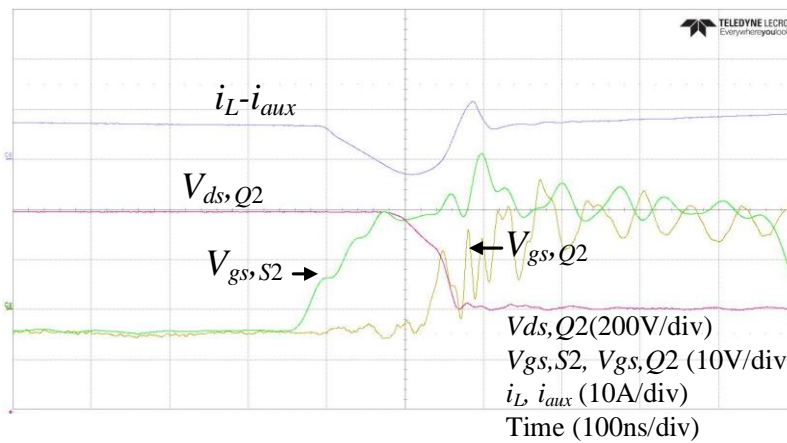


Figure 2.40 Turn-on transition corresponding to point b in Figure 2.38

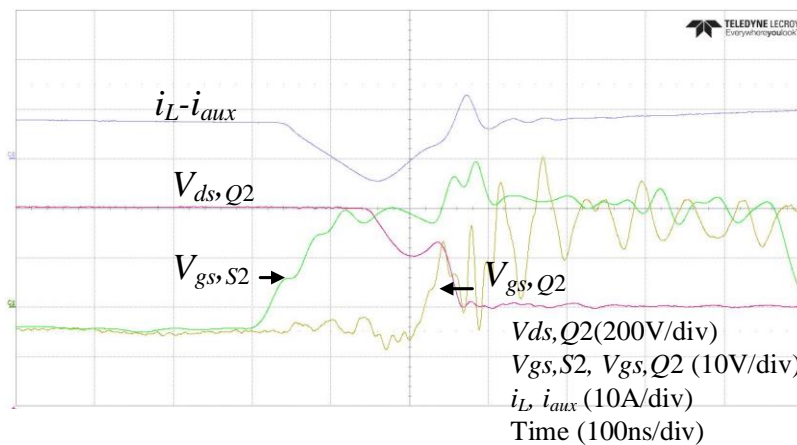


Figure 2.41 Turn-on transition corresponding to point c in Figure 2.38

A comparison with the recent full-bridge based inverter/PFC at similar power levels is given in Table 2.4. It is hard to find any full-bridge based inverter/PFC which operates

at switching frequency higher than 200 kHz except for critical mode operation (CRM) converters. The grid side filter of the CRM converters is larger than the continuous conduction mode (CCM) converters such as the proposed scheme with the same switching frequency since the converter side current is required to touch zero in every switching cycle. Compare with the CCM circuits in Table 2.4, the proposed circuit has pushed the switching frequency four times higher, while obtaining comparable circuit efficiency.

Table 2.4 Comparison with recent full-bridge based inverter/PFC

Circuit	Power device for the main switches	Power rating	Switching frequency	Peak efficiency	Number of components in auxiliary circuit
Proposed circuit	SiC MOSFET	2.4 kW	400 kHz	98.35%	3
CRM totem-pole PFC [38] (2018)	GaN	1.6 kW	450 kHz ~ 1 MHz	98.7%	0
CCM totem-pole PFC [39] (2018)	SiC MOSFET	6.6 kW	100 kHz	98.46%	0
ZVT HERIC Inverter [40] (2017)	SJ Si MOSFET	3 kW	100 kHz	97.8	8
ZVS full-bridge inverter [41] (2016)	SuperFET SJ Si MOSFET	3 kw	100 kHz	98.8	3

CHAPTER 3 DYNAMIC SIMULATION OF GRID-CONNECTED CONVERTERS IN LARGE-SCALE DISTRIBUTION SYSTEMS

In this chapter, the dynamic simulation used to study the performance and stability of the grid-connected converters and dynamic impact of CIGs in large scale distribution systems is discussed. The phasor extraction methods used in the interface between converter dynamic model and phasor network are introduced and compared. Dynamic simulations are conducted in OpenDSS for grid-connected converters with IEEE test feeder models as well as a detailed model of a real feeder. DLLs which can be used to conduct both static and dynamic simulations in OpenDSS are developed for dynamic models of grid-connected converter. The functions of DLLs are written based on the derived dynamic phasor model of the converter power stage circuit and controller.

3.1 Dynamic simulation of grid-connected converter by EMT-TS hybrid simulation and phasor extraction techniques

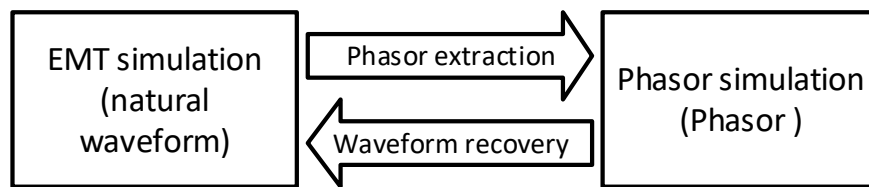


Figure 3.1 Data type conversion between EMT and phasor simulations

Phasors can be used to represent the magnitude and phase angle of fundamental frequency components in power system simulations where the fast transients are neglected. Power-flow can be solved to get the network solution in a phasor domain simulation which saves significant computational resources compared to pure EMT simulation. The conventional TS simulation is an example of such type of simulation in which the dynamics

of generators can be studied with network model solved by power-flow program. This can be done because the dynamic model of synchronous generators is also derived with phasors. However, the dynamic model of grid-connected converters is usually created with real valued signals, which means results will be generated as natural waveform rather than complex phasors. As shown in Figure 3.1, like most of the TS-EMT hybrid simulations, the data is required to be translated between phasor and instantaneous values if the converter model is interfaced to a phasor network model. As given in [48], the instantaneous value can be easily recreated based on the phasors when the reference frequency is known. However, the conversion in the opposite direction is more difficult where the phasor namely the magnitude and phase angle need to be extracted from the instantaneous value.

Common ways of implementing the phasor extraction are FFT based method [48] [49] and curve fitting based method [50]-[52]. They both require data of the instantaneous values over a time window (typically one fundamental cycle). Calculating FFT and curve fitting also add significant computation burden to the simulation, e.g, the curve fitting method in [50] is based on solving least square problem. There are other phasor extraction methods such as the rotating frame projection method [50] and instantaneous power based method [53] [54]. These methods do not require any historical data of the instantaneous values and the calculation involved is simpler compared with FFT and curve fitting methods. However, they can only be easily implemented in three-phase systems and cannot be used in unbalanced systems. This can be a main drawback in distribution system studies since the single-phase converters can be found in distribution system and the system is normally unbalanced. An alternative way of solving the data type mismatch is to model the

converter dynamics in phasor domain as described in [66]-[71]. The dynamic phasor modeling method [69]-[71] represents the system response with time-varying Fourier coefficients. The frequency adaptive network modeling method [66]-[68] uses complex analytic signal formed by Hilbert transform and frequency shifting to switch the simulation type between natural waveform and envelop waveform. Although the theoretical basis claimed in these two modeling methods are different, their mathematical implementations when modeling some systems are actually the same, including grid-connected converters. These modeling methods can be applied for systems with any number of phases. Thus, it can be used to model three-phase converters in unbalanced systems, as well as single-phase converter which are common in distribution systems. The phasor extraction techniques which are mentioned above will be briefly introduced in this section and a comparison will be given in the following section.

3.1.1 Phasor extraction based on sampled data over a sliding window

Since the phasor is equivalent to the first order Fourier series coefficient of the natural waveform, the phasor can be generated by calculating the fast Fourier transform (FFT) on the natural waveform data over a sliding window. With the sliding window length of the line frequency cycle and the sampling frequency of T_s , the formula of calculating the phasor can be given as

$$I_R + jI_I = \frac{2}{N} \sum_{k=0}^{N-1} i_k \cos(\omega_o(t - (N - 1 - k)T_s)) - j i_k \sin(\omega_o(t - (N - 1 - k)T_s)) \quad (3.1)$$

where N is the total number of samples in the sliding window. Since the phasor is written in rectangular form in the formula, it needs to be converted into polar form which consists of the magnitude and phase angle for most of the phasor domain simulations.

Similar to the FFT method, the magnitude and phase angle can be extracted by curve fitting. With N samples of the natural waveform over the line frequency cycle, the phasor can be evaluated by

$$I_R \min_{I, \theta_I} \sum_{k=0}^{N-1} (\sqrt{2}I \cos(\omega_0 t(k) + \theta_I) - i_k)^2 \quad (3.2)$$

where the error between the approximated and original waveform is minimized in the least square sense.

3.1.2 Phasor extraction based on direct-quadrature transformation

In conventional TS simulation, the abc to dq transformation is used to link the generator variables to the positive-sequence phasors of the external circuit. The same method can be used in EMT-TS hybrid simulations for balanced three-phase systems or when the unbalance can be neglected. The corresponding calculation is given as

$$\begin{bmatrix} I_R \\ I_I \end{bmatrix} = \frac{1}{\sqrt{2}} \begin{bmatrix} I_d \\ I_q \end{bmatrix} = T_1 \begin{bmatrix} i_a \\ i_b \\ i_c \end{bmatrix} \quad (3.3)$$

where

$$T_1 = \frac{2}{3\sqrt{2}} \begin{bmatrix} \cos(\omega_0 t) & \cos\left(\omega_0 t - \frac{2}{3}\pi\right) & \cos\left(\omega_0 t + \frac{2}{3}\pi\right) \\ -\sin(\omega_0 t) & -\sin\left(\omega_0 t - \frac{2}{3}\pi\right) & -\sin\left(\omega_0 t + \frac{2}{3}\pi\right) \end{bmatrix} \quad (3.4)$$

When a single-phase system needs to be simulated or all of phases in a three-phase system need to be modeled, the $\alpha\beta$ to dq transformation can be used:

$$\begin{bmatrix} I_R \\ I_I \end{bmatrix} = \frac{1}{\sqrt{2}} \begin{bmatrix} I_d \\ I_q \end{bmatrix} = T_2 \begin{bmatrix} i_\alpha \\ i_\beta \end{bmatrix} = \frac{1}{\sqrt{2}} \begin{bmatrix} \cos(\omega_o t) & \sin(\omega_o t) \\ -\sin(\omega_o t) & \cos(\omega_o t) \end{bmatrix} \begin{bmatrix} i_\alpha \\ i_\beta \end{bmatrix} \quad (3.5)$$

where the α axis value is the original value in the EMT simulation, the β axis value is a virtual parameter which is generated by delaying the original time-domain result in EMT simulation by a quarter cycle of the line frequency.

3.1.3 Complex analytical signal model/dynamic phasor model

Similar to the dq frame generator model in conventional TS simulations, the single-phase dynamic model can be represented in phasor domain by using the complex analytical signal model/dynamic phasor model. To derive the dynamic phasor model, the original real valued variables needs to be replaced by complex phasors. The relationship between the phasor and its real valued counterpart is given as (3.6) where $H(x(t))$ is the Hilbert transform of the original variable.

$$\bar{x}(t) = (x(t) + jH(x(t)))e^{-j\omega_o t} \quad (3.6)$$

The transform from real valued variable to complex phasor in frequency domain can be illustrated as Figure 3.2 [68]. The frequency spectrum of the signal becomes single-sided by adding an imaginary part of its own Hilbert transform. By a following frequency shift, the signal's frequency spectrum is centered at 0 Hz. It means dc components are dominant in the phasor model rather than fundamental frequency components unlike the case in the original real valued model. It has been reported that larger simulation time-step size can be

used to simulate the phasor model compared with the original model [68], which can be proved by Shannon's sampling theorem. The derivative formula of the phasors is given as

$$\frac{d\bar{x}_k}{dt} = -j\omega_o\bar{x}_k + f(\bar{x}_1, \dots, \bar{x}_n, \bar{u}_1, \dots, \bar{u}_m) \quad (3.7)$$

where

$$f(x_1, \dots, x_n, u_1, \dots, u_m) = \frac{dx_k}{dt} \quad (3.8)$$

x and u are system states and inputs respectively. \bar{x} and \bar{u} represent the corresponding complex phasor.

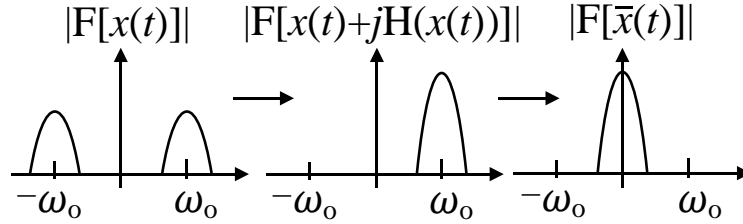


Figure 3.2 Application of Hilbert transform and frequency shifting

3.2 Comparison of the stability of the simulation using different phasor extraction techniques

A comparison will be made among the FFT, $\alpha\beta$ to dq transformation and dynamic phasor model based methods for single-phase systems. Note that the abc to dq transformation based method for three-phase systems can be considered equivalent to using dynamic phasor for single-phase systems. A simple system shown in Figure 3.3 is used for the discussion in this section. The EMT simulation contains a voltage source inverter followed by a grid side filter. The phasor simulation contains a simple two bus system. Infinite bus is not included in the network to emulate a standalone system.

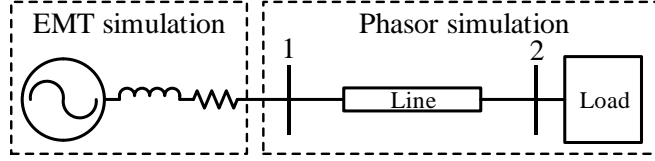


Figure 3.3 A simple system in EMT-TS hybrid simulation

3.2.1 Derivation of the analytical model of simulation

Analytical model of the phasor simulation

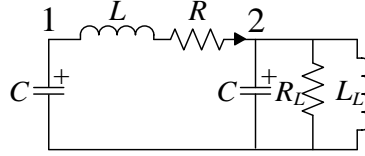


Figure 3.4 The simple system based on pi-section line model

As seen in Figure 3.4, the load at bus 2 is modeled as constant impedance and the distribution line is represented by the pi-section model. By written the real and imaginary part of the phasor separately, the phasor simulation can be represented by the algebraic equations:

$$\begin{bmatrix} V_{1R} \\ V_{1I} \\ V_{2R} \\ V_{2I} \\ I_{1R} \\ I_{1I} \\ I_{2R} \\ I_{2I} \end{bmatrix} = Z_{6 \times 2} \begin{bmatrix} I_{injR} \\ I_{injI} \end{bmatrix} = \begin{bmatrix} Z_{11} & Z_{12} \\ Z_{21} & Z_{22} \\ Z_{31} & Z_{32} \\ Z_{41} & Z_{42} \\ Z_{51} & Z_{52} \\ Z_{61} & Z_{62} \\ Z_{71} & Z_{72} \\ Z_{81} & Z_{82} \end{bmatrix} \begin{bmatrix} I_{injR} \\ I_{injI} \end{bmatrix} \quad (3.9)$$

where

$$Z_{6 \times 2} = \begin{bmatrix} 0 & \omega_o & 0 & 0 & -\frac{1}{C} & 0 & 0 & 0 \\ -\omega_o & 0 & 0 & 0 & 0 & -\frac{1}{C} & 0 & 0 \\ 0 & 0 & -\frac{1}{CR_L} & \omega_o & \frac{1}{C} & 0 & -\frac{1}{C} & 0 \\ 0 & 0 & -\omega_o & -\frac{1}{CR_L} & 0 & \frac{1}{C} & 0 & -\frac{1}{C} \\ \frac{1}{L} & 0 & -\frac{1}{L} & 0 & -\frac{R}{L} & \omega_o & 0 & 0 \\ 0 & \frac{1}{L} & 0 & -\frac{1}{L} & -\omega_o & -\frac{R}{L} & 0 & 0 \\ 0 & 0 & \frac{1}{L_L} & 0 & 0 & 0 & 0 & \omega_o \\ 0 & 0 & 0 & \frac{1}{L_L} & 0 & 0 & -\omega_o & 0 \end{bmatrix}^{-1} \begin{bmatrix} \frac{1}{C} & 0 \\ 0 & \frac{1}{C} \\ 0 & 0 \\ 0 & 0 \\ 0 & 0 \\ 0 & 0 \\ 0 & 0 \\ 0 & 0 \end{bmatrix} \quad (3.10)$$

The relationship between the current injection and bus voltage at bus 1 in phasor domain then can be written as

$$\begin{bmatrix} V_{1R} \\ V_{1I} \end{bmatrix} = \begin{bmatrix} Z_{11} & Z_{12} \\ Z_{21} & Z_{22} \end{bmatrix} \begin{bmatrix} I_{injR} \\ I_{injI} \end{bmatrix} = \begin{bmatrix} Z_1 & Z_2 \\ -Z_2 & Z_1 \end{bmatrix} \begin{bmatrix} I_{injR} \\ I_{injI} \end{bmatrix} = Z_{2 \times 2} \begin{bmatrix} I_{injR} \\ I_{injI} \end{bmatrix} \quad (3.11)$$

Analytical model of the EMT-TS simulation based on FFT phasor extraction

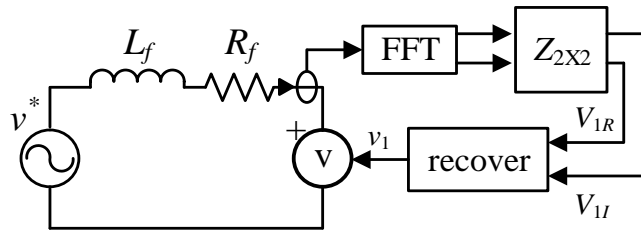


Figure 3.5 Equivalent representation of the EMT-TS simulation based on FFT phasor extraction

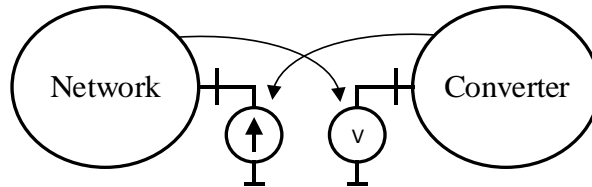


Figure 3.6 Representation of the network and dynamic model in the hybrid simulation

With FFT based phasor extraction at the interface, the EMT-TS simulation of the simple system can be represented by the block diagram in Figure 3.5. This arrangement complies with the hybrid simulation illustrated in Figure 3.6 in which the network is represented as a variable voltage source in the converter model and the converter is represented as a current injection in the network model. The network model is represented by the 2 by 2 matrix given in (3.11). The recovery of the instantaneous voltage from the phasor is calculated as

$$v(t) = \sqrt{2}V_R \cos(\omega_o t) - \sqrt{2}V_I \sin(\omega_o t) \quad (3.12)$$

The EMT system can be simply represented by the grid side filter dynamics:

$$i_f = \frac{di_f}{dt} = \frac{1}{L_f} v^* - \frac{1}{L_f} v_1 - \frac{R_f}{L_f} i_f \quad (3.13)$$

By assuming the number of samples used in the FFT calculation (3.1) is infinite, the FFT calculation can be written in s domain:

$$I_{injR}(s) = 2\mathcal{L}(i_f \cos(\omega_o t)) \frac{60 \left(1 - e^{-\frac{1}{60}s}\right)}{s} \quad (3.14)$$

$$I_{injI}(s) = 2\mathcal{L}(-i_f \sin(\omega_o t)) \frac{60 \left(1 - e^{-\frac{1}{60}s}\right)}{s} \quad (3.15)$$

where $\mathcal{L}(\cdot)$ is the Laplace transformation. To illustrate the effect of FFT, the EMT system is represented in dq frame by including a fictitious β axis EMT system in which all the parameters are the same as the original system. The hybrid simulation then can be

illustrated as the block diagram shown in Figure 3.7. The dq frame equations of the EMT system can be written as

$$\begin{bmatrix} \dot{i}_{fd} \\ \dot{i}_{fq} \end{bmatrix} = \begin{bmatrix} -\frac{R_f}{L_f} i_{fd} + \omega_o i_{fq} - \frac{1}{L_f} v_{1d} + \frac{1}{L_f} v_d^* \\ -\omega_o i_{fd} - \frac{R_f}{L_f} i_{fq} - \frac{1}{L_f} v_{1q} + \frac{1}{L_f} v_q^* \end{bmatrix} \quad (3.16)$$

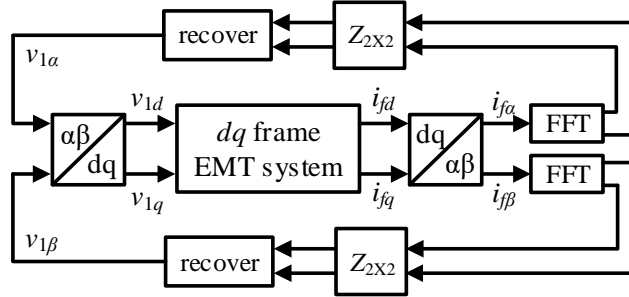


Figure 3.7 EMT-TS simulation based on FFT phasor extraction represented in dq frame

By writing the equations (3.14) and (3.15) with respect to dq frame variables, the equations become:

$$I_{injR}(s) = \mathcal{L}(i_{fd} + i_{fd} \cos(2\omega_0 t) - i_{fq} \sin(2\omega_0 t)) \frac{60 \left(1 - e^{-\frac{1}{60}s}\right)}{s} \quad (3.17)$$

$$I_{injI}(s) = \mathcal{L}(i_{fq} - i_{fq} \cos(2\omega_0 t) + i_{fd} \sin(2\omega_0 t)) \frac{60 \left(1 - e^{-\frac{1}{60}s}\right)}{s} \quad (3.18)$$

The term $\frac{60(1-e^{-1/60s})}{s}$ can be considered as taking the cycle-by-cycle average of the terms in the Laplace transformation. Thus, the equation can be simplified by neglecting the double line frequency terms:

$$I_{injR}(s) \approx i_{fd}(s) \frac{60 \left(1 - e^{-\frac{1}{60}s}\right)}{s} \quad (3.19)$$

$$I_{injI}(s) \approx i_{fq}(s) \frac{60 \left(1 - e^{-\frac{1}{60}s}\right)}{s} \quad (3.20)$$

Then the simulation can be represented as Figure 3.8. The equations combining the phasor network model and FFT phasor extraction can be written as

$$v_{1d}(s) = z_1 i_{fd}(s) \frac{60 \left(1 - e^{-\frac{1}{60}s}\right)}{s} + z_2 i_{fq}(s) \frac{60 \left(1 - e^{-\frac{1}{60}s}\right)}{s} \quad (3.21)$$

$$v_{1q}(s) = -z_2 i_{fd}(s) \frac{60 \left(1 - e^{-\frac{1}{60}s}\right)}{s} + z_1 i_{fq}(s) \frac{60 \left(1 - e^{-\frac{1}{60}s}\right)}{s} \quad (3.22)$$

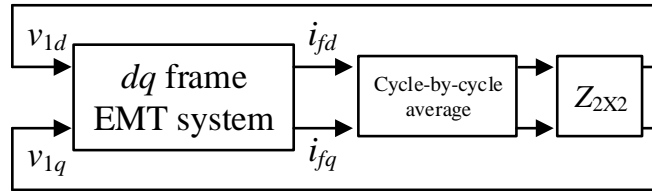


Figure 3.8 Equivalent representation of the EMT-TS simulation based on FFT phasor extraction

Analytical model of the EMT-TS simulation based on $\alpha\beta$ to dq transformation

The EMT-TS simulation based on $\alpha\beta$ to dq transformation can be represented as Figure 3.9. The quarter cycle delay can be represented as

$$i_{f\beta}(s) = i_f(s) e^{-\frac{1}{240}s} \quad (3.23)$$

The transfer function from i_f to v_1 can be derived:

$$\begin{aligned}
v_1 &= [\cos(\omega_o t) \quad -\sin(\omega_o t)] \begin{bmatrix} z_1 & z_2 \\ -z_2 & z_1 \end{bmatrix} \begin{bmatrix} \cos(\omega_o t) & \sin(\omega_o t) \\ -\sin(\omega_o t) & \cos(\omega_o t) \end{bmatrix} \begin{bmatrix} i_f \\ i_{f\beta} \end{bmatrix} \\
&= z_1 i_f + z_2 i_{f\beta} = i_f(s) \left(z_1 + z_2 e^{-\frac{1}{240}s} \right)
\end{aligned} \tag{3.24}$$

As seen in Figure 3.9, the bus voltage v_1 can be considered as a feedback to the EMT system. Combing (3.13) and (3.24), the closed loop transfer function of the EMT-TS simulation can be written as:

$$i_f(s) = \frac{\frac{1}{L_f}}{s + \frac{R_f + z_1}{L_f} + \frac{z_2}{L_f} e^{-\frac{1}{240}s}} v^*(s) \tag{3.25}$$

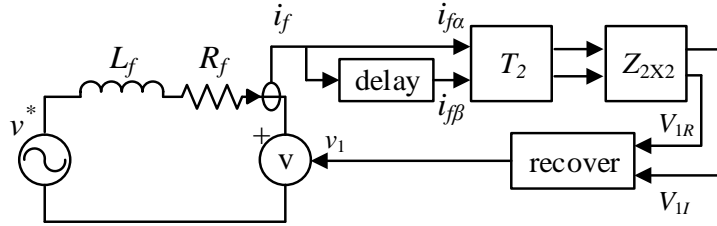


Figure 3.9 Simplified representation of the EMT-TS simulation based on $\alpha\beta$ to dq transformation

Analytical model of the EMT-TS simulation based on dynamic phasor

As shown in Figure 3.9, the dynamic phasor model of the EMT system is identical to the dq frame model given in (3.16). By combining the network matrix, the complete analytical model of the EMT-TS simulation based on dynamic phasor is

$$\begin{bmatrix} \dot{i}_{fd} \\ \dot{i}_{fq} \end{bmatrix} = \begin{bmatrix} -\frac{R_f + z_1}{L_f} & \omega_o - \frac{z_2}{L_f} \\ -\omega_o + \frac{z_2}{L_f} & -\frac{R_f + z_1}{L_f} \end{bmatrix} \begin{bmatrix} i_{fd} \\ i_{fq} \end{bmatrix} + \begin{bmatrix} \frac{1}{L_f} & 0 \\ 0 & \frac{1}{L_f} \end{bmatrix} \begin{bmatrix} v_d^* \\ v_q^* \end{bmatrix} \tag{3.26}$$

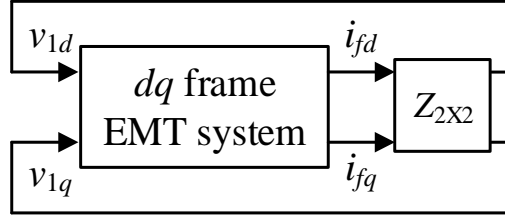


Figure 3.10 Equivalent representation of the EMT-TS simulation based dynamic phasor

3.2.2 Stability of EMT-TS simulation based on different phasor extraction methods

The stability of the EMT-TS simulation based on different phasor extraction methods is discussed based on the derived analytical models. Note that the system simply consists of a voltage source followed by a pass circuit which is stable. However, the EMT-TS hybrid simulation might generate unstable result as what will be illustrated in this section.

As shown in the derived analytical models, the dynamic phasor based simulation is the only one which doesn't introduce any phase delay to the system. Based on (3.26), the closed loop poles of the dynamic phasor based simulation are $-\frac{R_f+z_1}{L_f} \pm j \left| \omega_o - \frac{z_2}{L_f} \right|$.

It can be shown that z_1 is positive when the P load at bus 2 is positive. Thus, the system is always stable since the closed loop poles only have negative real part.

As seen in (3.25), the quarter cycle delay is introduced in the closed loop transfer function of the EMT-TS simulation based on $\alpha\beta$ to dq transformation by a factor of $\frac{z_2}{L_f}$. By using the second order Pade approximation, the delay can be represented as

$$e^{-\frac{1}{240}s} = \frac{s^2 - 1440s + 691200}{s^2 + 1440s + 691200} \quad (3.27)$$

Then the transfer function (3.25) can be written as

$$i_f(s) = \frac{\frac{1}{L_f}(s^2 + 1440s + 691200)v^*(s)}{\left(s + \frac{R_f + z_1}{L_f}\right)(s^2 + 1440s + 691200) + \frac{z_2}{L_f}(s^2 - 1440s + 691200)} \quad (3.28)$$

The root locus shown in Figure 3.11 is plotted by varying the value of $\frac{z_2}{L_f}$. It shows one of the closed loop poles can move to the right half plane as $\left|\frac{z_2}{L_f}\right|$ increases. This is the scenario when Q load at bus 2 is increased as the value of L_f is fixed.

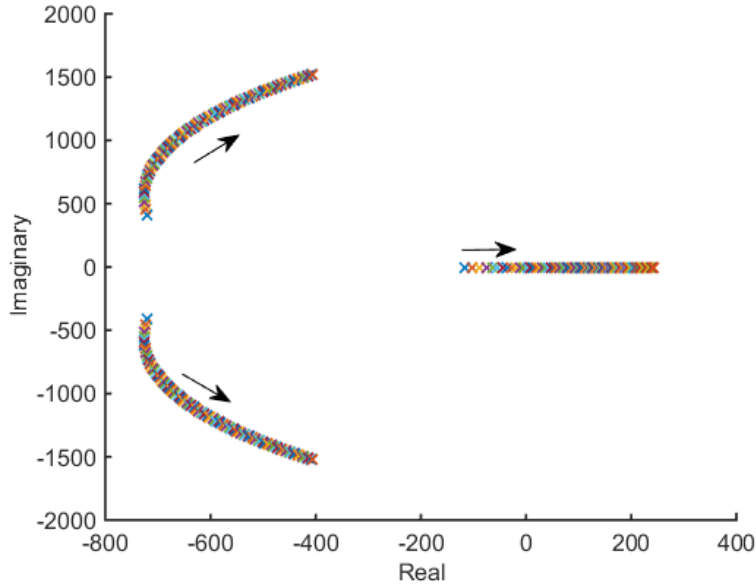


Figure 3.11 Root locus of EMT-TS simulation based on $\alpha\beta$ to dq transformation

In the analytical model of the EMT-TS simulation based on FFT phasor extraction, phase delay is introduced by the cycle-by-cycle averaging in both d and q axis loops. By representing the pure time delay by second order Pade approximation, the state-space equations of Figure 3.8 can be written as

$$\begin{bmatrix} \dot{i}_{fd} \\ \dot{i}_{fq} \\ \dot{x}_1 \\ \dot{x}_2 \\ \dot{x}_3 \\ \dot{x}_4 \end{bmatrix} = \begin{bmatrix} -\frac{R_f}{L_f} & \omega_o & 0 & \frac{-10.55z_1}{L_f} & 0 & \frac{-10.55z_2}{L_f} \\ -\omega_o & -\frac{R_f}{L_f} & 0 & \frac{10.55z_2}{L_f} & 0 & \frac{-10.55z_1}{L_f} \\ 16 & 0 & -360 & -168.4 & 0 & 0 \\ 0 & 0 & 256 & 0 & 0 & 0 \\ 0 & 16 & 0 & 0 & -360 & -168.4 \\ 0 & 0 & 0 & 0 & 256 & 0 \end{bmatrix} \begin{bmatrix} i_{fd} \\ i_{fq} \\ x_1 \\ x_2 \\ x_3 \\ x_4 \end{bmatrix} \quad (3.29)$$

where x_1, x_2, x_3, x_4 are the internal states from the Pade approximation of the time delay. To investigate the impact of network parameters to the system stability, the highest real part value among the system eigenvalues is plotted by varying the value of R_f, L_f, z_1 and z_2 . As shown in Figure 3.12, lower damping of the EMT system will make the system unstable. While as shown in Figure 3.13, smaller values of L_f will make the system unstable. Both figures show that large values of z_1 and z_2 will make the system unstable. This is the scenario when both P and Q load at bus 2 are low.

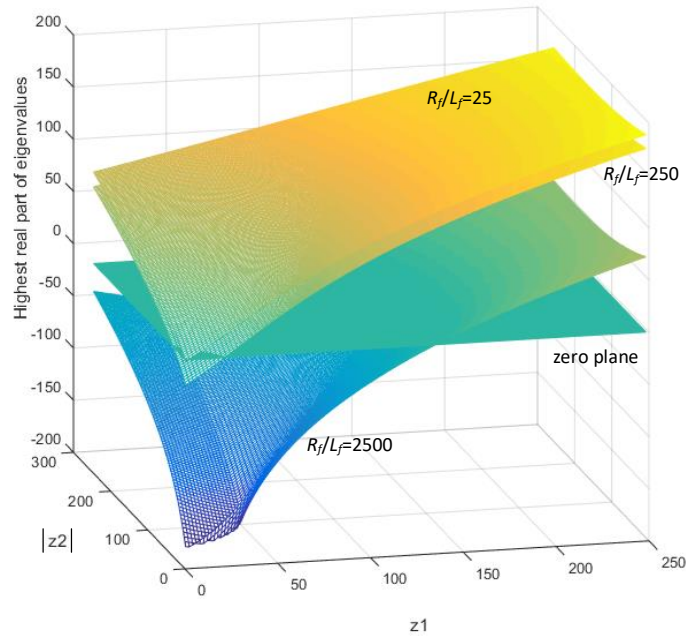


Figure 3.12 The highest real part of the closed loop poles of the EMT-TS simulation based FFT phasor extraction: $L_f = 200$ mH

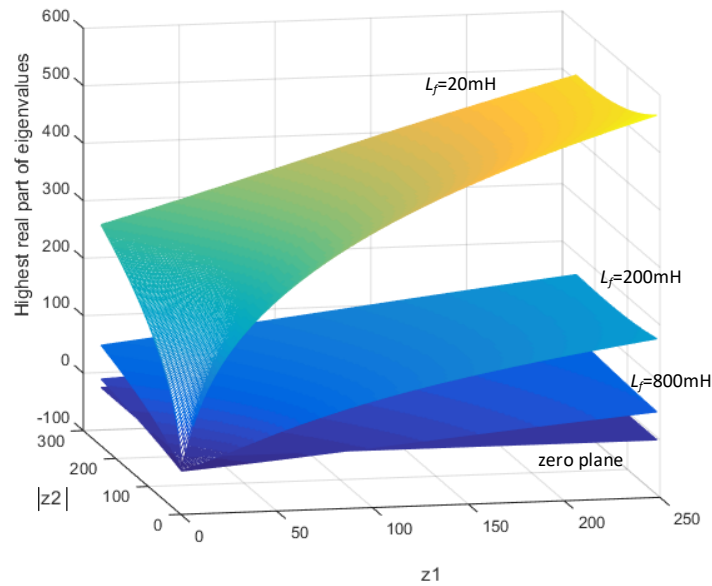


Figure 3.13 The highest real part of the closed loop poles of the EMT-TS simulation based FFT phasor extraction: $R_f/L_f = 25$

The closed loop poles of the system in FFT and $\alpha\beta$ to dq transformation based simulations are calculated based on the derived analytical models for several cases where the load at bus 2 is different. The common system parameters used in the calculation is given in Table 3.1. The calculated closed loop poles are plotted in Figure 3.14-Figure 3.17. As seen in the figures, the FFT based simulation is unstable in case 1 and case 4; the $\alpha\beta$ to dq transformation based simulation is unstable in case 3 and case 4; both methods are stable in case 2.

Table 3.1 Other system parameters used in the closed loop pole calculation

Nominal voltage	7.2 kV
pi-section line	$R = 0.173 \Omega$ $L = 1.08$ mH $C = 4.47$ nF
Inverter grid side filter	$L_f = 200$ mH $R_f = 5 \Omega$

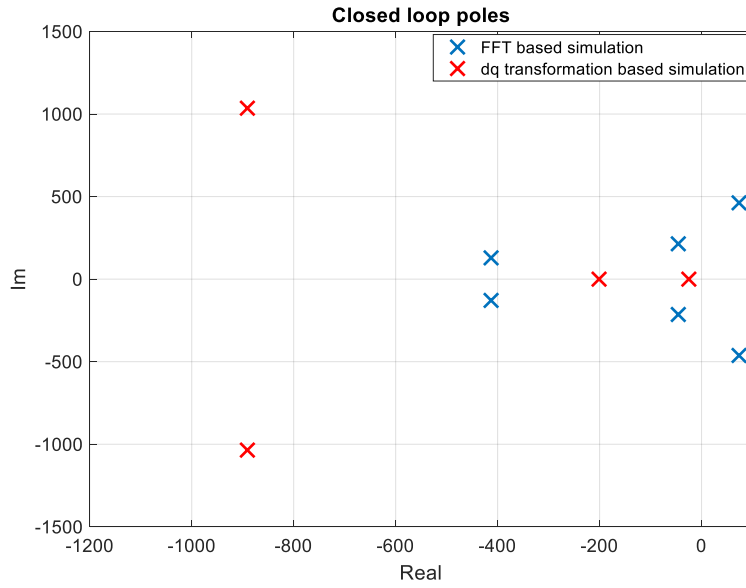


Figure 3.14 Case 1: P = 300 kW, Q = 100 kVAr ($z_1 = 155.72$, $z_2 = -52.17$)

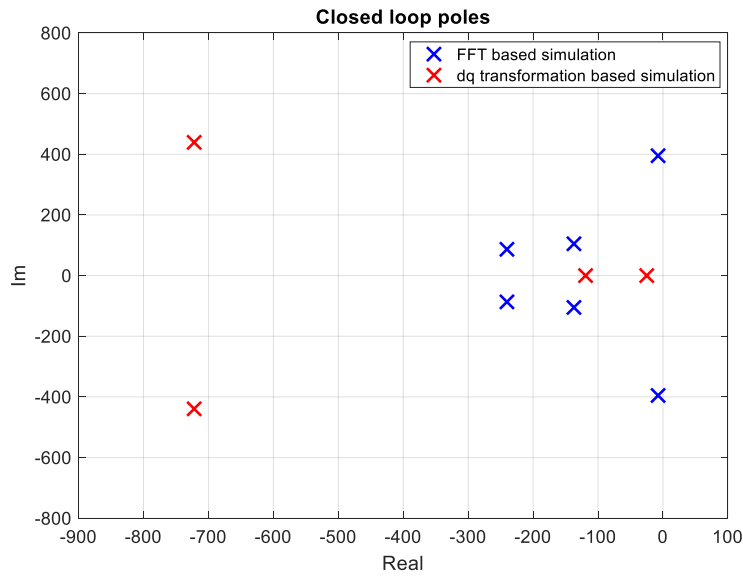


Figure 3.15 Case 2: P = 2500 kW, Q = 100 kVAr ($z_1 = 20.87$, $z_2 = -1.23$)

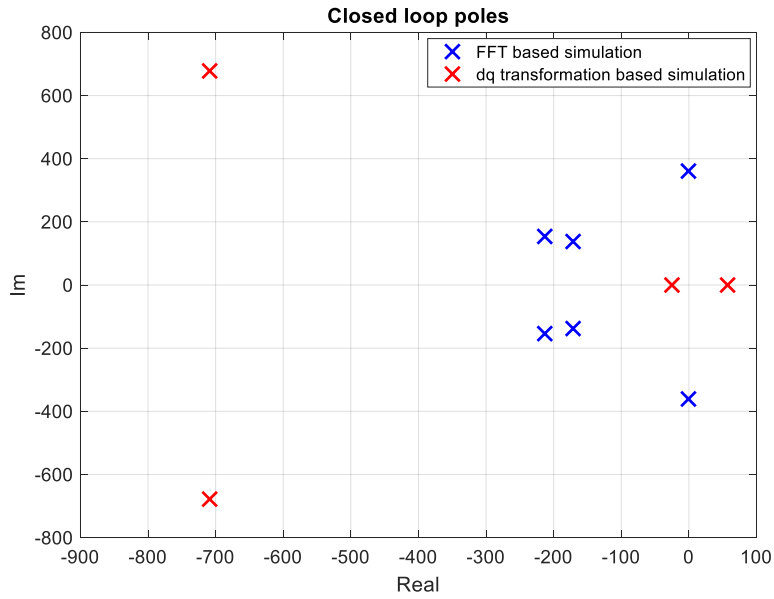


Figure 3.16 Case 3: $P = 2.5 \text{ kW}$, $Q = 2500 \text{ kVAr}$ ($z_1 = 0.19$, $z_2 = -21.14$)

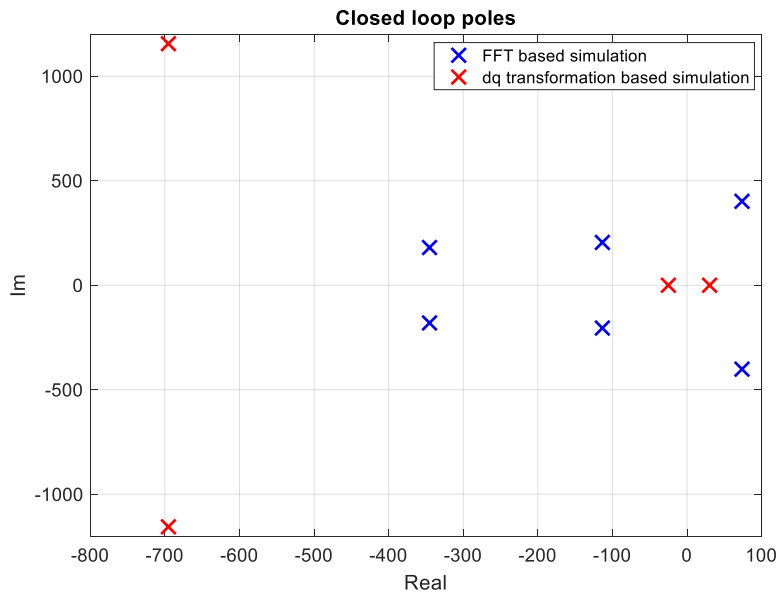


Figure 3.17 Case 4: $P = 300 \text{ kW}$, $Q = 400 \text{ kVAr}$ ($z_1 = 62.4$, $z_2 = -83.35$)

To validate the result, EMT-TS simulations are conducted through MATLAB and OpenDSS. The EMT simulation is emulated by MATLAB script where the integration loop is written based on equation (3.13) or (3.16). The phasor extraction methods are also implemented in the script to calculate the phasor of the filter current. The network model

is created in OpenDSS to provide the phasor solution of the network. In each integration step, OpenDSS is called by the MATLAB script to solve the power-flow to provide the newest voltage at bus 1. The filter current calculated in the previous step is used in the power-flow. With newest bus voltage, the filter current is updated for the current step based on the integration. The communication between MATLAB and OpenDSS is through the OpenDSS COM interface. The initial value of the filter current which is a state in the EMT model, is set to zero in the simulations. The simulation results corresponding to the cases of Figure 3.14-Figure 3.17 are shown in Figure 3.18. It shows that the stability of the simulation results match with prediction of the derived analytical models. Based on this comparison, the dynamic phasor model based EMT-TS simulation has the advantage in the simulation stability perspective as compared with the other two methods.

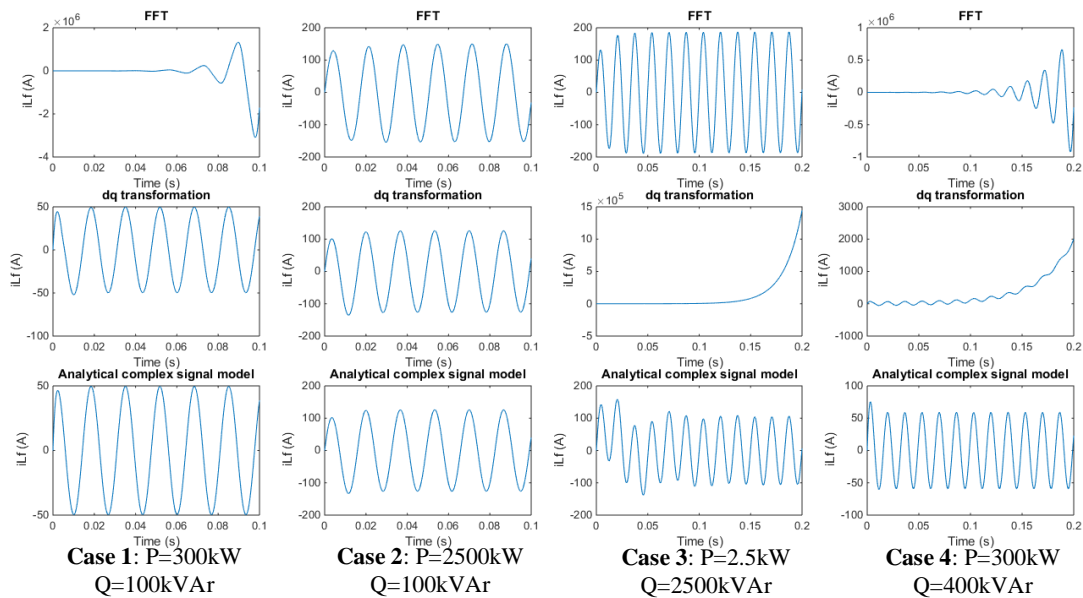


Figure 3.18 EMT-TS simulation results based on MATLAB and OpenDSS using three different phasor extraction methods

3.3 Dynamic phasor model of a single-phase grid-connected converter

The dynamic phasor model of the grid-connected converter has been derived in this work to study the dynamics of the converter in large-scale distribution systems. The EMT simulation model of a single-phase grid-connected converter is shown in Figure 3.19. The dynamic phasor model of the converter is derived based on (3.6) and (3.7).

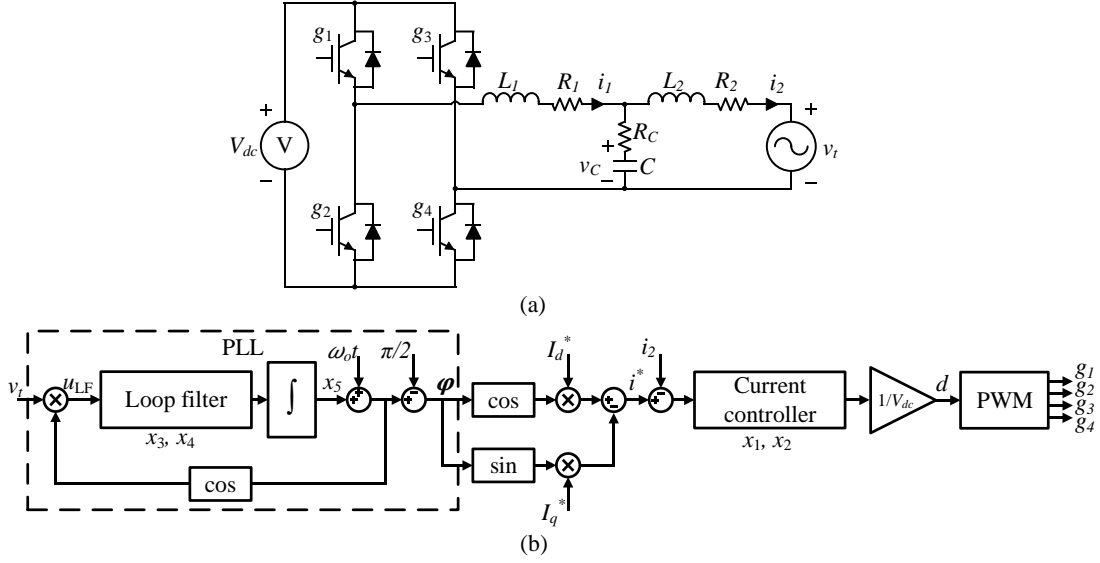


Figure 3.19 A single-phase grid-connected converter model [72]:

(a) power stage circuit (b) controller structure

Based on (3.7), the phasor equations of the LCL filter in the figure can be derived

as:

$$\frac{d\bar{i}_1}{dt} = -j\omega_o \bar{i}_1 - \frac{R_C + R_1}{L_1} \bar{i}_1 + \frac{R_C}{L_1} \bar{i}_2 - \frac{1}{L_1} \bar{v}_C + \frac{1}{L_1} \bar{e} \quad (3.30)$$

$$\frac{d\bar{i}_2}{dt} = -j\omega_o \bar{i}_2 - \frac{R_C + R_2}{L_2} \bar{i}_2 + \frac{R_C}{L_2} \bar{i}_1 + \frac{1}{L_1} \bar{v}_C - \frac{1}{L_1} \bar{v}_r \quad (3.31)$$

$$\frac{d\bar{v}_C}{dt} = -j\omega_o \bar{v}_C + \frac{1}{C} \bar{i}_1 - \frac{1}{C} \bar{i}_2 \quad (3.32)$$

The converter terminal voltage \bar{v}_i is considered as the input of the phasor state-space model.

The converter output current \bar{i}_2 is considered as both the state and output of the phasor model.

A proportional-resonant (PR) controller is modeled for the current controller to eliminate the steady state error of tracking the sinusoidal reference. The transfer function of the PR controller can be written as

$$d = \left(K_P + \frac{K_R s}{s + 0.6s + (2\pi 60)^2} \right) (\bar{i}^* - \bar{i}_2) \quad (3.33)$$

where K_P and K_R are the proportional gain and resonant gain respectively. Based on (3.7) and the corresponding state-space representation of the transfer function, the phasor equations of the current controller can be derived as

$$\frac{d\bar{x}_1}{dt} = -j\omega_o \bar{x}_1 - 0.6\bar{x}_1 - 277.6\bar{x}_2 + \bar{i}^* - \bar{i}_2 \quad (3.34)$$

$$\frac{d\bar{x}_2}{dt} = -j\omega_o \bar{x}_2 + 512\bar{x}_1 \quad (3.35)$$

$$\bar{d} = (K_R \bar{x}_1 + K_P (\bar{i}^* - \bar{i}_2)) / V_{dc} \quad (3.36)$$

where \bar{x}_1 and \bar{x}_2 are the phasors corresponding to the internal states of the PR controller.

The voltage at the switching pole can be expressed as the following equation by using the average model of the PWM converter.

$$\bar{e} = V_{dc} \bar{d} = K_R \bar{x}_1 + K_P (\bar{i}^* - \bar{i}_2) \quad (3.37)$$

States x_3 and x_4 in the PLL shown in Figure 3.19 come from a loop filter for filtering out the double frequency component from the input and an integrator for compensating the steady state error between the PLL output and the terminal voltage phase angle. The transfer function of such a second order loop filter can be given as

$$G_{LF} = \frac{4.7(s + 3.37)}{s(s + 46.9)} \quad (3.38)$$

where the bandwidth of the filter is set as 2Hz. Together with state x_5 in the figure, the state-space equations are given as

$$\begin{bmatrix} \dot{x}_3 \\ \dot{x}_4 \\ \dot{x}_5 \end{bmatrix} = \begin{bmatrix} -46.9 & 0 & 0 \\ 1 & 0 & 0 \\ 2.357 & 7.938 & 0 \end{bmatrix} \begin{bmatrix} x_3 \\ x_4 \\ x_5 \end{bmatrix} + \begin{bmatrix} 2u_{LF} \\ 0 \\ 0 \end{bmatrix} \quad (3.39)$$

To simplify the model and the model dc component dominant, the double frequency component can be neglected from the loop filter input as the following expression

$$\begin{aligned} u_{LF} &= v_t \cos(x_5 + \omega_o t) \\ &= (\text{Re}(\bar{v}_t) \cos(\omega_o t) - \text{Im}(\bar{v}_t) \sin(\omega_o t)) \cos(x_5 + \omega_o t) \\ &= \frac{\text{Im}(\bar{v}_t) \cos(x_5) - \text{Re}(\bar{v}_t) \sin(x_5)}{2} \dots \\ &\quad - \frac{\text{Im}(\bar{v}_t) \cos(x_5 + 2\omega_o t) + \text{Re}(\bar{v}_t) \sin(x_5 + 2\omega_o t)}{2} \\ &\approx \frac{\text{Im}(\bar{v}_t) \cos(x_5) - \text{Re}(\bar{v}_t) \sin(x_5)}{2} \end{aligned} \quad (3.40)$$

The equations of PLL are derived with the original real valued variables. However, the PLL output will be used to calculate the phasor of the current reference, as follows.

$$i^* = I_d^* \cos(\varphi) - I_q^* \sin(\varphi) \quad (3.41)$$

$$\begin{aligned}\bar{i}^* &= (i^* + jH(i^*))e^{-j\omega_s t} \\ &= I_d^* \cos(x_5) - I_q^* \sin(x_5) + j(I_d^* \sin(x_5) + I_q^* \cos(x_5))\end{aligned}\tag{3.42}$$

3.4 Dynamic simulation of grid-connected converters in large unbalanced distribution systems using OpenDSS

3.4.1 Dynamic simulation in OpenDSS by using DLLs

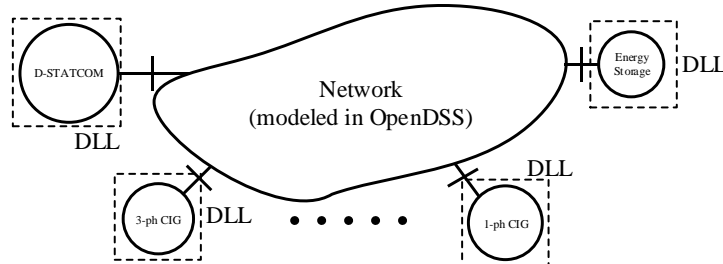


Figure 3.20 Dynamic simulation using DLL in OpenDSS

As shown in Figure 3.20, the dynamic model can be written in dynamic-link library (DLL) and used by OpenDSS for dynamic simulations. One of the merits of using DLL is that it can help protect the proprietary information for the device vendors who want to provide the dynamic model of their products. Using DLL also has the advantage of scalability, for example, only one DLL is needed when multiple instances of the same devices are in the system.

In OpenDSS, current carrying circuit elements including lines, reactors, capacitors and transformers are represented by primitive Y matrix. The power conversion elements such as CIGs are represented as compensation currents at the corresponding node. Figure 3.21 shows the system equivalent circuit of dynamic simulation in OpenDSS. In the network model, a CIG is represented as current injection or impedance at the corresponding node depending on whether the terminal current is modeled as a state in the CIG model. In

the CIG model, the external network is represented as variable voltage source at the output terminal.

The DLL structure including the interface with OpenDSS has been defined by the OpenDSS developers and can be found on the OpenDSS website [44]. As shown in Figure 3.22, **Init** (initialization), **Calc** (algebraic equations) and **Integrate** are the major functions where the device model is contained. Function **Calc** calculates the current injection to the network; it also calculates other internal variables of the CIG that are related to the terminal voltage with just algebraic equations. If the CIG terminal current is modeled as a state, the value updated in function Integrate will be used. If the relationship between terminal voltage and current is governed by just algebraic equations, the corresponding equations are written in function **Calc** to be used in the iterations for solving the node voltage. The integration of state variables happens in the function Integrate. The predefined integration method in OpenDSS is the two- step predictor-corrector method. The calculation of the state incremental value at each integration step is based on the differential equations (state space equations) derived from the CIG model. Function **Init** is used for the model initialization at the beginning of the dynamic simulation.

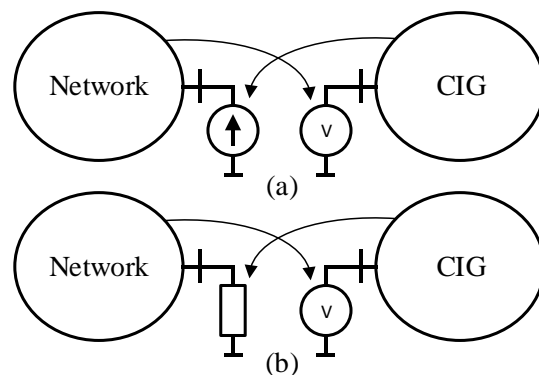


Figure 3.21 Representation of the network and dynamic model in OpenDSS:
 (a) CIG represented as current source (b) CIG represented as impedance

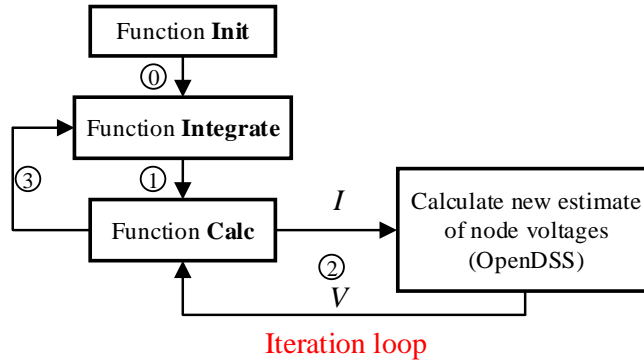


Figure 3.22 Interaction between OpenDSS and the main functions in DLL

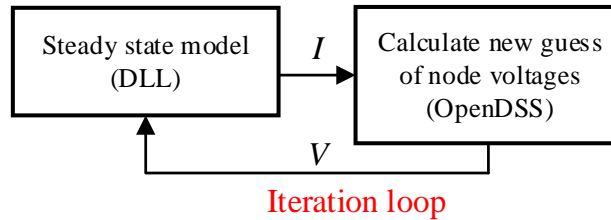


Figure 3.23 Solving power-flow by using the steady state model in DLL

At each time-step, the updated state values are sent to function **Calc** as shown by Step 1 and are kept as constants during the iteration in Step 2. After the network solution converges, in Step 3, the variables calculated in function **Calc** are sent back to function **Integrate** as the input of the state space equations. Function **Init** is called at the beginning of the dynamic simulation to determine the initial values of all of the states based on the terminal voltage. The terminal voltage at the start of each time-step comes from the latest power-flow result, which means that in order to get the terminal voltage value for the very first time-step, the system has to be solved in power-flow mode before the simulation goes into dynamic mode. As shown in Figure 3.23, a steady state model of the device is also stored in the DLL so that it can also be used in steady state and quasi-static simulations.

DLLs have been developed for CIG based on the dynamic phasor model derived in Section 3.4. The derived equations are used to write the **Integrate**. The equations for the steady state model and function **Init** are derived by setting the derivative of the state

variables to zero. Simulations have been conducted with small and large distribution system models. No calculation is needed in function **Cal** in this case since the terminal current is modeled as a state. A comparison is given between the result of OpenDSS and PLECS [42] for a small test system to validate the accuracy of the developed DLL.

3.4.2 Validation in IEEE 13-node test system

To validate the developed DLL of CIG model, a dynamic simulation is conducted in OpenDSS for the IEEE 13-node test system model which can be found in the OpenDSS website. The single-phase CIG is installed at phase A of bus 675 through a step-down transformer. The CIG is let controlled to generate both active and reactive power. The voltage and current at the CIG terminal and one of the remote lines in the system are monitored. Time domain results are generated to show the dynamic changes in currents and voltages as a step change is given to the CIG current command. The same system is also modeled in PLECS to conduct the full detailed EMT simulation. In PLECS, pi-section model is used for modeling the lines. The constant current and constant PQ loads in the system are modeled by variable current source synchronized with the bus voltage through a high bandwidth PLL. The instantaneous value of the currents and voltages from the EMT simulation are compared with the phasor results of the dynamic simulation in OpenDSS.

In the simulation, the current reference I_d^* is changed from 0 to 1021 A at 1s, which corresponds to 200 kW at the rated voltage of 277 V. The current reference I_q^* is kept as -510 A which corresponds to 100 kVAr of reactive power delivery. The voltage and current waveforms of the CIG terminal are shown in Figure 3.24 and Figure 3.25. The phasor results from OpenDSS can also be converted into instantaneous values by assuming the phase angle of the rotating reference frame. Figure 3.26 shows the instantaneous values

corresponding to Figure 3.24. Again, it shows a good agreement between the OpenDSS and PLECS results. The phase A voltage and current of the sending end of line 632-671 (bus 632) are shown in Figure 3.27 and Figure 3.28. Since OpenDSS does calculation in RMS values, the magnitude values from OpenDSS are multiplied by $\sqrt{2}$ before generating the plots in order to match the phasor results with the envelope of the sinusoidal waveforms. As shown in the figures, the dynamic simulation result shows a good match with the EMT simulation result. The simulation times of these two software are given in Table 3.2. The simulation time is 60% smaller than in PLECS even for the simple system considered. The advantages will be more striking for the larger systems where it may not be practical to simulate using PLECS.

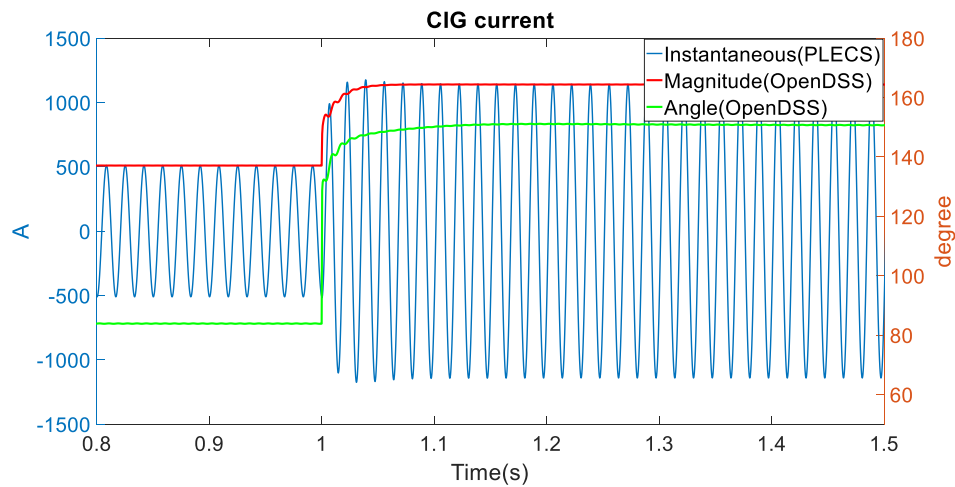


Figure 3.24 Comparison of proposed method and PLECS time domain simulation: CIG current during a step change in I_d^*

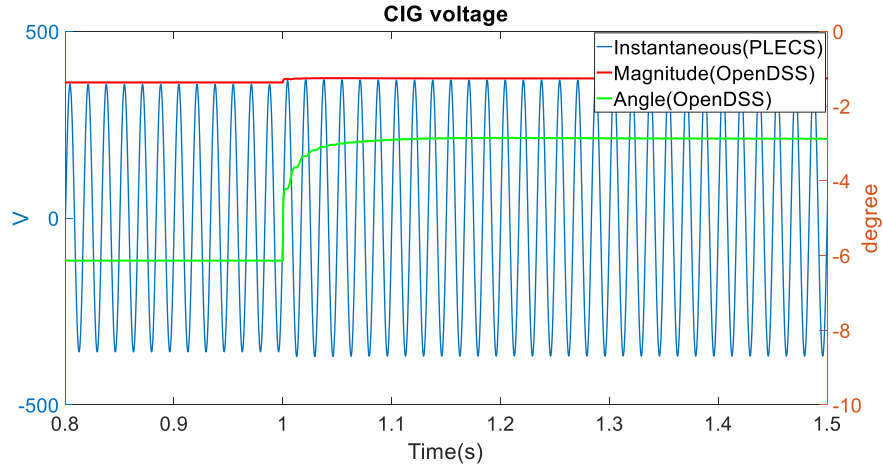


Figure 3.25 Comparison of proposed method and PLECS time domain simulation: CIG terminal voltage during a step change in I_d^*

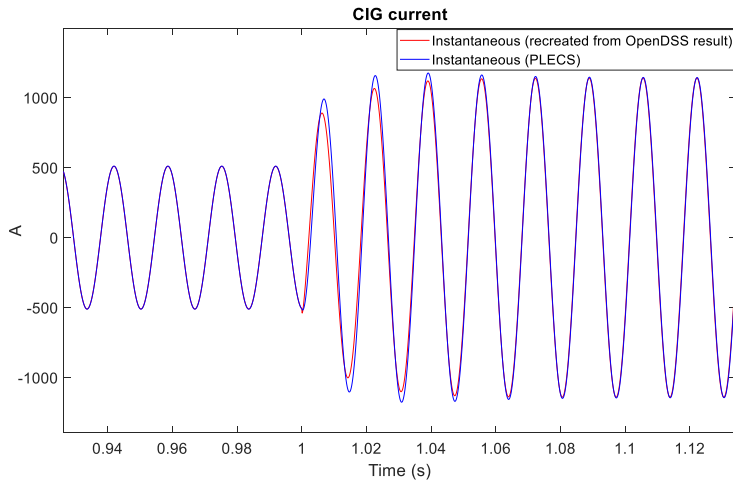


Figure 3.26 Instantaneous value of CIG current: OpenDSS vs PLECS

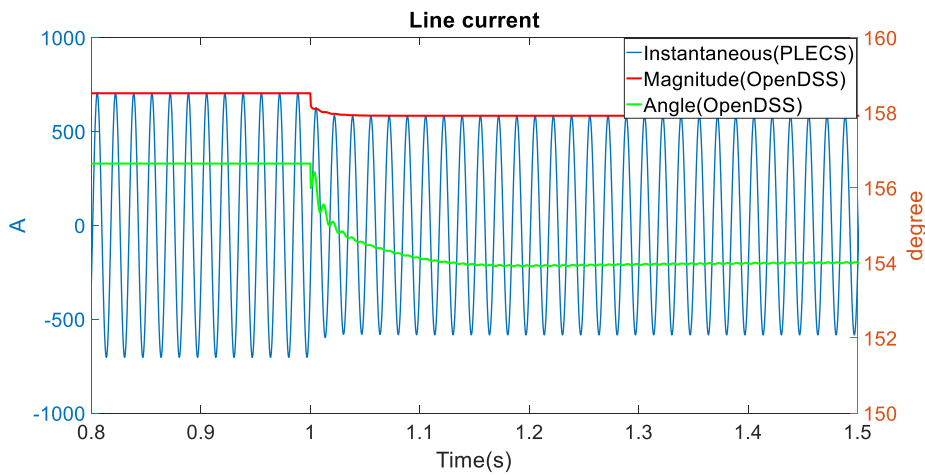


Figure 3.27 Comparison of proposed method and PLECS time domain simulation: line current during step change in I_d^*

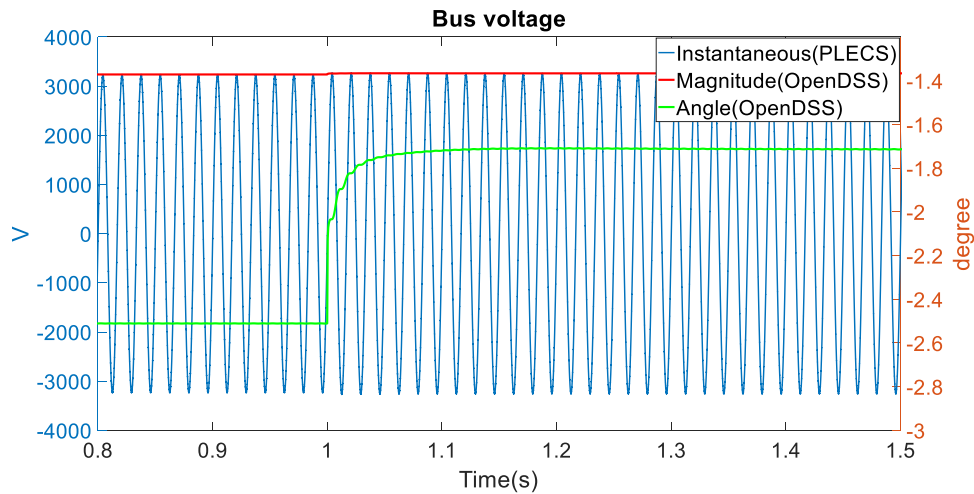


Figure 3.28 Comparison of proposed method and PLECS time domain simulation: bus voltage during step change in I_d^*

Table 3.2 Simulation time comparison

CPU model: Intel Core i7-6700 @ 3.4 GHz	
Length of the simulation: 2 s	
Simulation time-step size: 5 μ s	
Simulation time	
Dynamic simulation by OpenDSS	EMT simulation by PLECS
28 s	67 s

Three phase CIG models have also been developed based on the derived equations. A commonly seen three-phase PLL as shown in Figure 3.29 is modeled instead of the single-phase scheme. Figure 3.30 shows the CIG current waveform when a single-phase to ground fault is applied to the primary side of the transformer. The OpenDSS phasor result is converted to instantaneous value to compare with the result obtained in a detailed time domain simulation in PLECS. Both simulations show the same result where the inverter regulates the current at the maximum allowable value. The current distortion is caused by the double frequency noise at the PLL output when the three-phase voltage is unbalanced. Figure 3.30 also shows the waveform obtained by using conventional positive-sequence inverter model in OpenDSS. It shows that the developed CIG model is able to be used in

unbalanced cases while the conventional positive-sequence inverter model can only generate balanced result.

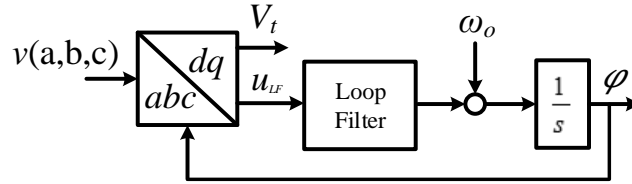


Figure 3.29 Three-phase SRF-PLL

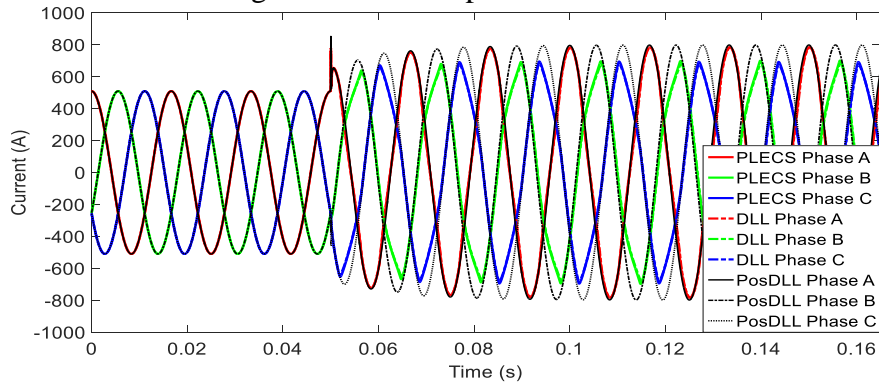


Figure 3.30 Comparison with PLECS time domain simulation and positive sequence model: three-phase CIG response to single-phase fault

As stated in [75], the CIG behavior when connected to a weak grid is greatly affected by the PLL dynamics. Moreover, under islanded condition, which is the extreme case of weak grid, the PLL frequency will start to drift away from the nominal value for most of the load conditions. This mechanism has been used in many of the islanding detection schemes in the grid-connected converters [76]. To show that the PLL dynamics have been properly included in the CIG model, a test case is conducted by opening the switch between bus 671 and 692. Figure 3.31 shows the simulation results of the PLL frequency from OpenDSS and PLECS. The switch is opened at 1 s which makes the branch with CIG under islanded condition. Both OpenDSS and PLECS show similar result in which the PLL frequency starts to decrease after the switch is opened. The results of OpenDSS and PLECS are slightly different when PLL frequency becomes significantly

lower than the nominal value since the OpenDSS does not take the change of load and line impedance with respect to frequency into account.

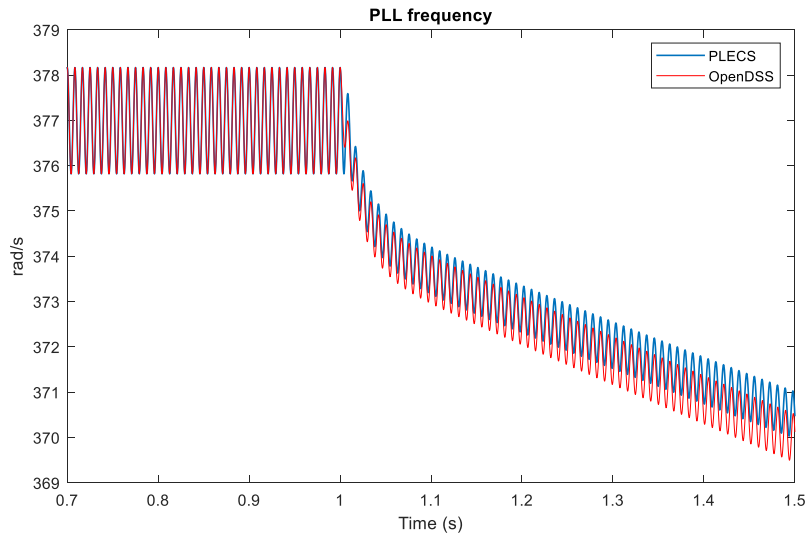


Figure 3.31 PLL frequency after disconnecting the feeder from the grid

3.4.3 Volt-VAr control implementation in a large, real feeder

As shown in Figure 3.32, the network model of the distribution system located in Flagstaff, AZ is modeled in OpenDSS based on the provided GIS data [73]. In this test case, two 700 kW PV systems as well as over 100 residential PV system with small power ratings are modeled in the system by using the developed CIG DLL. The three-phase PVs are represented by three single-phase CIG DLLs installed on three phases. The volt-VAr control [74] is added to the CIG model to adjust the reactive current reference based on the terminal voltage magnitude.

A snap shot simulation is initially conducted to obtain the steady state voltage profile along the feeder as shown in Figure 3.33. As seen, without the volt-VAr control, over-voltage happens on certain lines under the impact of PV contribution. Figure 3.34 shows the dynamic simulation result where the volt-VAr function are enabled for all of the

PVs modeled in the system at 2 ms. As seen, the feeder voltages gradually dip after the volt-VAr function is enabled, and no over-voltage is seen after 2.4 ms.

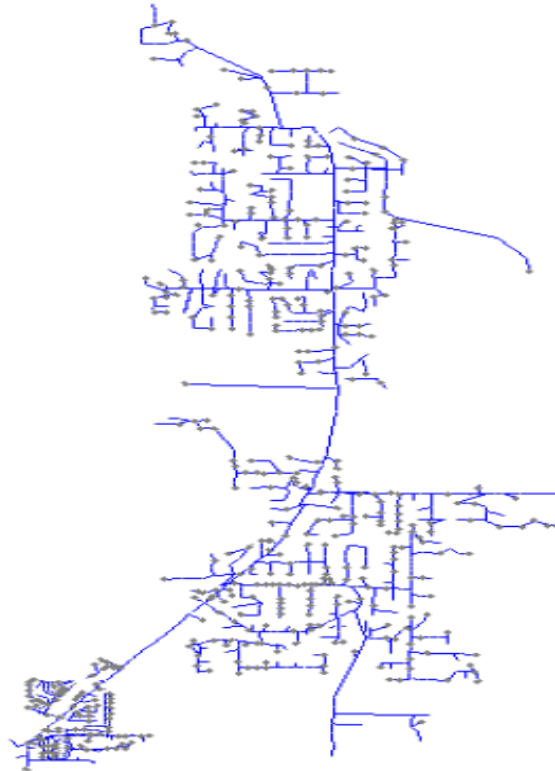


Figure 3.32 OpenDSS model of the distribution feeder in Flagstaff, AZ

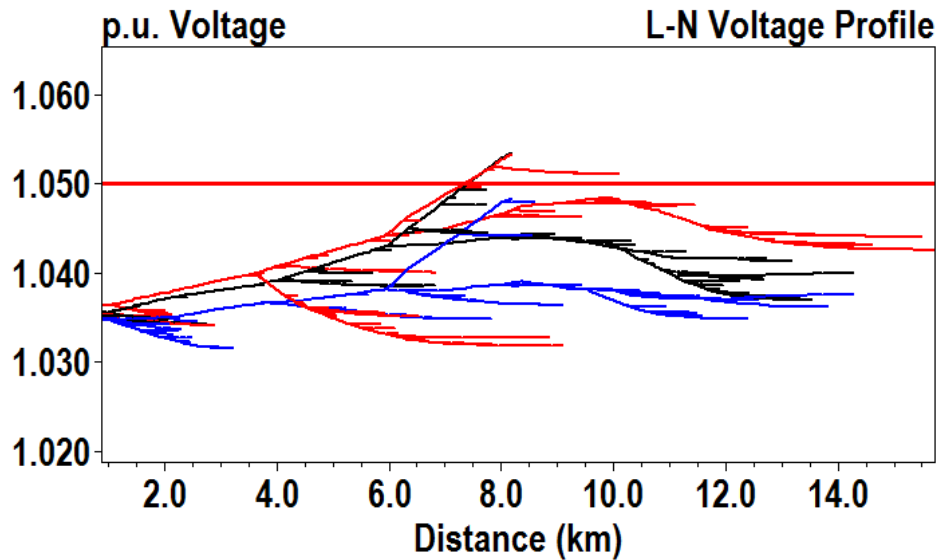


Figure 3.33 Voltage profile along the feeder in snapshot simulation

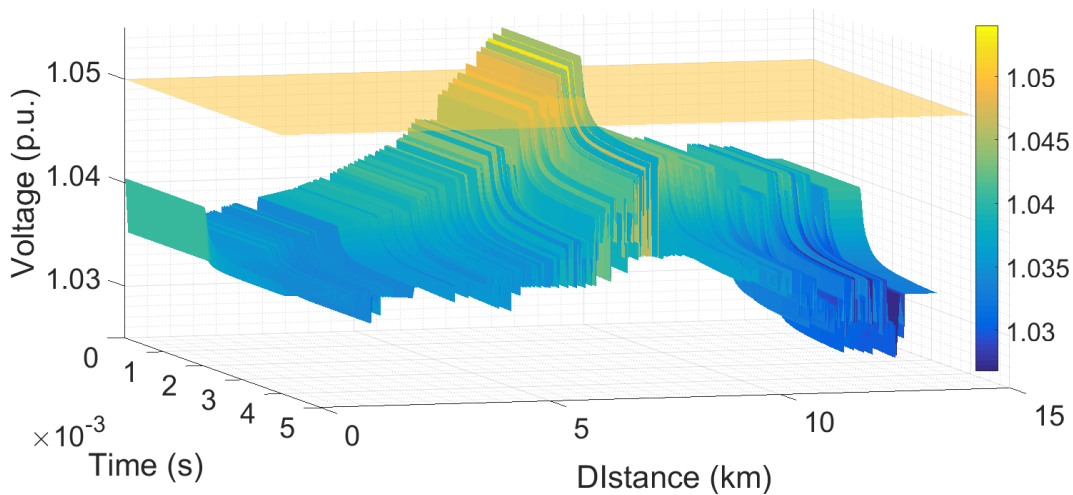


Figure 3.34 Voltage profile changing with time in dynamic simulation

3.4.4 CIG based microgrid control in IEEE 123-node test feeder

In CIG based microgrid operation, a feeder is energized by both the substation and the installed CIGs. Dynamic simulations are needed to evaluate the performance of the controllers during grid-connected and grid-islanded modes. Hence, DLL based on the CIG control structure shown in Figure 3.35 is developed based on the corresponding dynamic phasor model. The IEEE 123-bus test feeder model available in OpenDSS is used in this test case. Three CIGs are added to the system at bus 1, bus 7, and bus 47 respectively.

With microgrid mode controller, the frequency and magnitude of the CIG output voltage are constantly adjusted by the CIG controller based on a set of P-f and Q-V droop characteristics. The breaker near the substation is opened at 1s. The simulation results are shown in Figure 3.36-Figure 3.38. As shown in Figure 3.36, before the breaker opens, the CIGs supply active power based on their ratings. After the breaker opens, the lost generation due to the lack of the main grid is picked up by the CIGs based on the P-f droop characteristics. With the same droop coefficients and power ratings, the total loads are shared equally among three of the CIGs. As shown in Figure 3.37, the reactive power

outputs are different among the CIGs. This is expected since the CIGs are installed at different locations in the system causing the impedance seen by each CIG at its terminal as well as the voltage to be different. Figure 3.38 shows the reference frequency of one of the CIGs, which droops as the active power output increases with a transient lasting approximately 0.5 s.

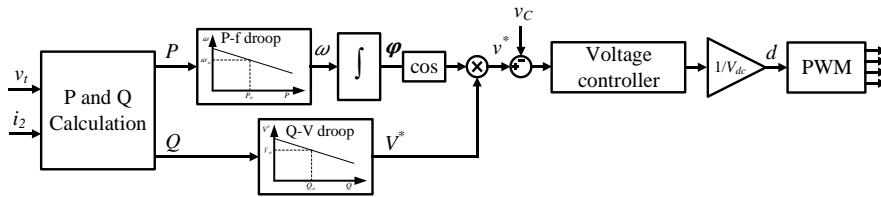


Figure 3.35 Droop based microgrid control of single-phase CIG

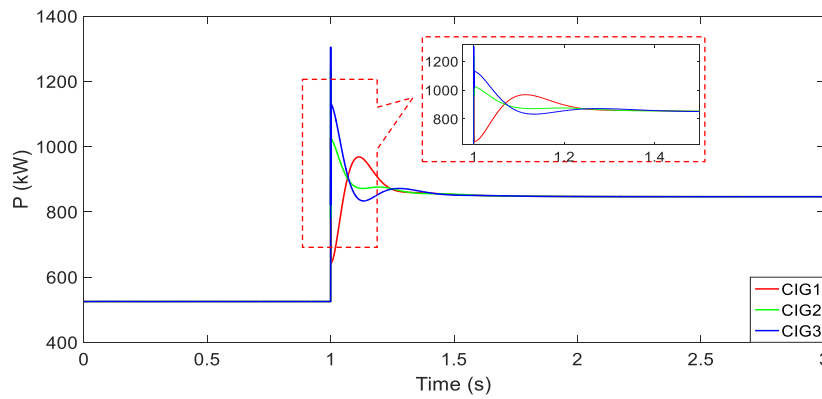


Figure 3.36 Active power outputs from the CIGs in the 123-bus test feeder by disconnecting the grid at 1 s

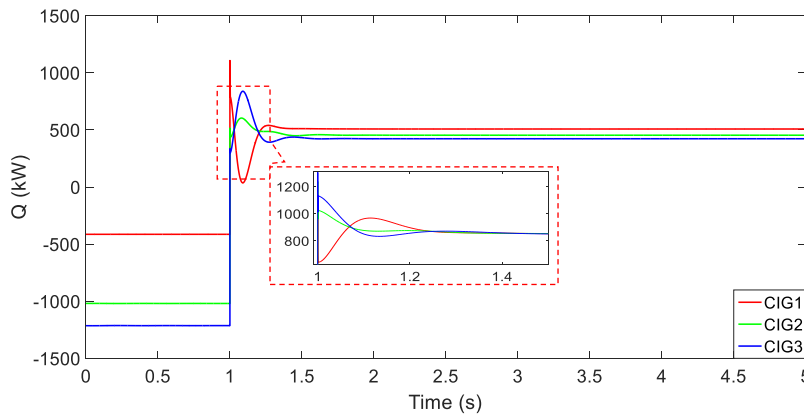


Figure 3.37 Reactive power outputs from the CIGs in the 123-bus test feeder by disconnecting the grid at 1s

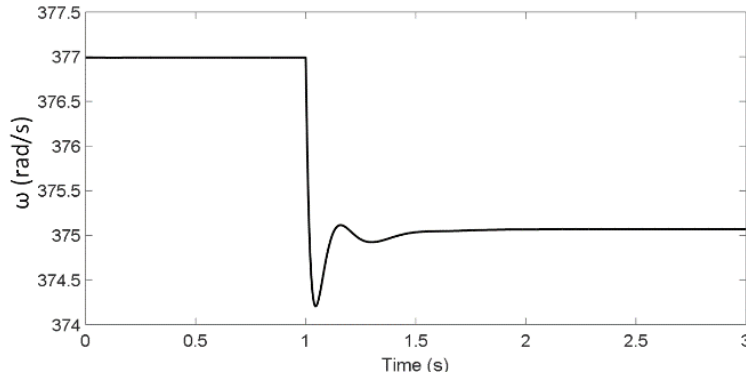


Figure 3.38 CIG frequency change after islanding

3.4.5 Discussion

As described in the literature [48]-[54], the dynamic mode simulation in OpenDSS has two issues in simulating the CIG. The first issue is that the same time-step size is used for solving the network and detailed model. However, it is reasonable to use a larger time-step size to solve the network when the time-step size needed by the detailed model is very small (e.g. 5 μ s used in the IEEE 13-node test system simulation). Unfortunately, OpenDSS doesn't support different time-step sizes in the simulation. The second issue is the less accurate equivalent circuit of external network used in the dynamic model. Equivalent impedance other than the ideal source has been recommended to be included in the representation of the external network to increase the model accuracy. The multi-port impedance network in [77] can be used when there are more than one CIGs in the system. This requires some information to be shared among several CIG models, which is not supported by using DLL. A possible solution to implement multi time-step sizes simulation and the equivalent multi-port impedance network is by using the COM interface with MATLAB provided in OpenDSS.

CHAPTER 4 REAL-TIME SIMULATION OF A MICROGRID

POWERED BY CONVERTER-INTERFACED GENERATORS

In this chapter, a real-time simulation of an inverter based microgrid is demonstrated. The proposed microgrid is powered by energy cells consisting of renewable energy resource, energy storage and inverter interface. A hierarchical control including a microgrid central controller and inverter level local controllers is proposed for the microgrid. The proposed controls including the communication between the central controller and local controllers are simulated in a multi-platform, real-time simulation testbed based on Opal-RT, EZDSP F28335 and Modbus communication protocol. The concept of EMT-TS hybrid simulation in Chapter 3 is used to build a large-scale system for real-time simulation in Opal-RT. Other than the dynamic modeling of the inverters, load side dynamic modeling is also included by modeling the air conditioner compressor single-phase induction motor.

4.1 Hierarchical control of CIG based microgrids

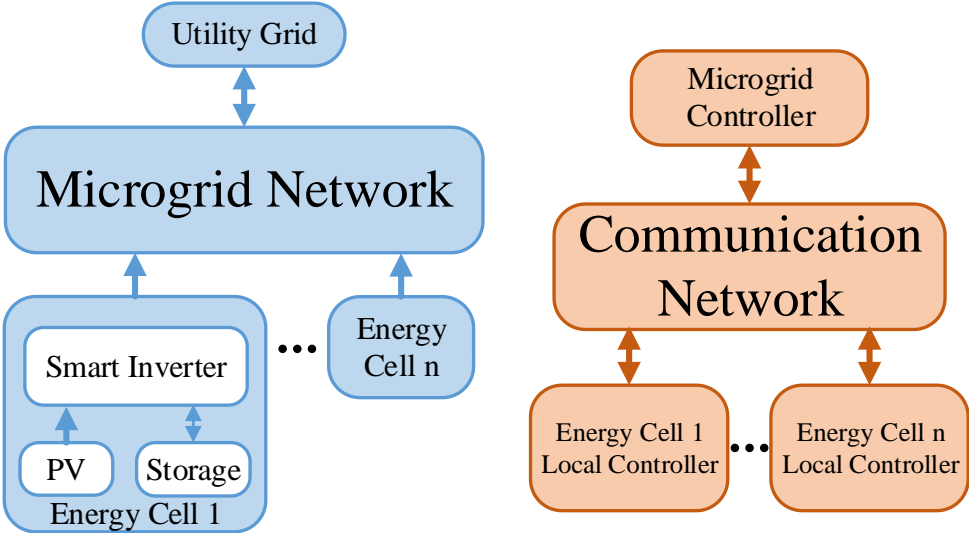


Figure 4.1 The physical layer and control structure of a microgrid

Figure 4.1 shows the structure of a microgrid which is powered by energy cells consisting of PV generator and energy storage system. The energy cells are connected to the microgrid network through a smart inverter which controls the active and reactive power injected to the microgrid. The microgrid is connected to the utility grid at one point and can become an islanded grid by breaking the connection. Each energy cell contains a local controller which communicates with the microgrid central controller through a communication network. For better system reliability, a hierarchical control structure can be used in which the commands from the upper level controls don't significantly impact the stability of the control loops in the lower level. For example, the energy cell local controllers should be able to operate under temporary loss of the communication with the central controller. Literature [104] and [105] have suggested a standard hierarchical control structure for the converter based microgrid. By modifying the suggested control structure, a three-level control scheme is proposed for the real-time simulation of the CIG based microgrid. Level 1 control establishes the AC voltage with multiple inverters in the network, without confliction. Level 2 control provides the voltage and frequency regulation which compensates the voltage/frequency variations with respect to different load conditions in the level 1 control. Level 2 control also provides the power sharing adjustment among the energy cells. Level 3 control is used for grid-connected operation when the system is connected to the utility grid.

4.1.1 Level 1 control

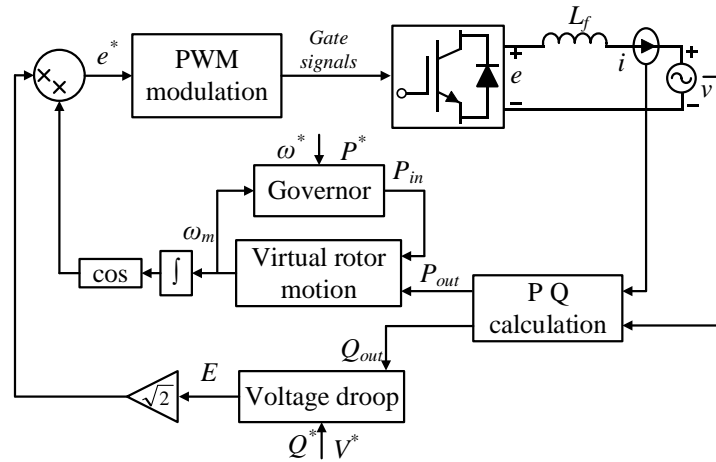


Figure 4.2 Virtual synchronous generator control

The level 1 control is proposed based on the virtual synchronous generator (VSG) control in [101]. The block diagram of the VSG control is given in Figure 4.2. The smart inverter controls its terminal voltage such that the dynamic response of a synchronous generator is emulated. In such a way, multiple inverters can coexist in an islanded network without an infinite bus; droop method can also be used to control the load sharing among the VSGs as how a synchronous generator is controlled.

In the VSG control scheme, the motion of the synchronous machine is emulated to provide the inverter a virtual inertia. The angular speed of the virtual rotor namely the frequency of the inverter side voltage is determined by the swing equation:

$$J\omega_m \frac{d\omega_m}{dt} = P_{in} - P_{out} \quad (4.1)$$

where J is the virtual inertia, P_{in} is virtual shaft power given by the governor, P_{out} is the inverter active power output. The inverter output power can be calculated with the corresponding phasors:

$$P_{out} = \sum_{p=a,b,c} v_{pd}i_{pd} + v_{pq}i_{pq} \quad (4.2)$$

where v_d, v_q, i_d, i_q are the phasors of inverter terminal voltage and current in direct and quadrature axes. The virtual governor is a droop controller which determines the virtual shaft power based on the frequency ω_m :

$$P_{in} = P^* + (\omega^* - \omega_m)/m_p \quad (4.3)$$

where P^* is the reference value of the energy cell power output, m_p is the droop coefficient, ω^* is the system reference frequency. The inverter reactive power output is regulated by a voltage droop:

$$E = V^* + m_q(Q^* - Q_{out}) \quad (4.4)$$

where V^* is the voltage reference of the inverter, Q^* is reactive power reference of the energy cell, m_q is the droop coefficient. The inverter reactive power output Q_{out} can be calculated by

$$Q_{out} = \sum_{p=a,b,c} v_{qp}i_{dp} - v_{dp}i_{qp} \quad (4.5)$$

The instantaneous inverter side voltage is

$$\begin{aligned} e_a &= E \cos(\omega_m t) \\ e_b &= E \cos(\omega_m t - 2\pi/3) \\ e_c &= E \cos(\omega_m t + 2\pi/3) \end{aligned} \quad (4.6)$$

Assuming the rotating angle of a common network reference frame is $\omega_o t$, the inverter side voltage in the common reference frame can be derived as

$$\begin{aligned} \begin{bmatrix} e_{ad} \\ e_{aq} \end{bmatrix} &= \begin{bmatrix} E \cos(\theta) \\ E \sin(\theta) \end{bmatrix} \\ \begin{bmatrix} e_{bd} \\ e_{bq} \end{bmatrix} &= \begin{bmatrix} E \left(\frac{\sqrt{3}\sin(\theta)}{2} - \frac{\cos(\theta)}{2} \right) \\ E \left(-\frac{\sqrt{3}\cos(\theta)}{2} - \frac{\sin(\theta)}{2} \right) \end{bmatrix} \\ \begin{bmatrix} e_{cd} \\ e_{cq} \end{bmatrix} &= \begin{bmatrix} E \left(-\frac{\sqrt{3}\sin(\theta)}{2} - \frac{\cos(\theta)}{2} \right) \\ E \left(\frac{\sqrt{3}\cos(\theta)}{2} - \frac{\sin(\theta)}{2} \right) \end{bmatrix} \end{aligned} \quad (4.7)$$

where

$$\theta = \int (\omega_m - \omega_o) dt \quad (4.8)$$

The relationship between the inverter output current, terminal voltage and inverter side voltage is governed by the grid filter dynamics:

$$\begin{aligned} \begin{bmatrix} \dot{i}_{ad} \\ \dot{i}_{aq} \end{bmatrix} &= \begin{bmatrix} -\frac{R_f}{L_f} & \omega_o \\ -\omega_o & -\frac{R_f}{L_f} \end{bmatrix} \begin{bmatrix} i_{ad} \\ i_{aq} \end{bmatrix} + \begin{bmatrix} \frac{1}{L_f} & 0 \\ 0 & \frac{1}{L_f} \end{bmatrix} \begin{bmatrix} e_{ad} - v_{ad} \\ e_{aq} - v_{aq} \end{bmatrix} \\ \begin{bmatrix} \dot{i}_{bd} \\ \dot{i}_{bq} \end{bmatrix} &= \begin{bmatrix} -\frac{R_f}{L_f} & \omega_o \\ -\omega_o & -\frac{R_f}{L_f} \end{bmatrix} \begin{bmatrix} i_{bd} \\ i_{bq} \end{bmatrix} + \begin{bmatrix} \frac{1}{L_f} & 0 \\ 0 & \frac{1}{L_f} \end{bmatrix} \begin{bmatrix} e_{bd} - v_{bd} \\ e_{bq} - v_{bq} \end{bmatrix} \end{aligned} \quad (4.9)$$

$$\begin{bmatrix} \dot{i}_{cd} \\ \dot{i}_{cq} \end{bmatrix} = \begin{bmatrix} -\frac{R_f}{L_f} & \omega_o \\ -\omega_o & -\frac{R_f}{L_f} \end{bmatrix} \begin{bmatrix} i_{cd} \\ i_{cq} \end{bmatrix} + \begin{bmatrix} \frac{1}{L_f} & 0 \\ 0 & \frac{1}{L_f} \end{bmatrix} \begin{bmatrix} e_{cd} - v_{cd} \\ e_{cq} - v_{cq} \end{bmatrix}$$

The level 1 controls are implemented in the energy cell local controller, while the reference values ω^* and V^* are generated in the level 2 control in the central controller.

4.1.2 Level 2 control

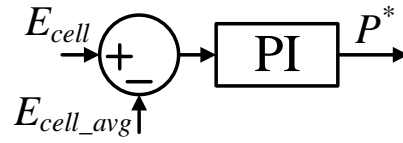


Figure 4.3 Dynamic power sharing control

The active and reactive power sharing among the VSGs can be adapted by changing the value of power references and droop coefficients. The active power sharing scheme based on battery charging level is proposed in [105] by changing the active power droop coefficient. However, changing the droop coefficient might cause stability problem [106] which makes it difficult to find a feasible range for the droop coefficient to adapt. In this work, a dynamic power sharing scheme is proposed based on adapting the power references P^* . Assuming the energy level of the cell which is determined by

$$E_{cell} = \int (P_{PV} - P_{out}) dt \quad (4.10)$$

is measured by the local controller, the active power shared by the energy cell can be adapted based on its stored energy level. As shown in Figure 4.3, the cell stored energy level is compared with the average energy level in the system, the error is passed to a PI controller to generate the active power reference for the VSG control. With the proposed

control, the active power sharing among the energy cells is dynamically adapted with respect to the PV generations. The energy level of all the energy cells will be balanced and be charged/discharged under identical rate of energy (power) in steady-state. To adapt the reactive power sharing among the inverters, the V-Q droop coefficient is scaled by a factor based on

$$m_q = \frac{m_{qo}}{k} \quad (4.11)$$

where

$$k = \frac{\sqrt{S_{rated}^2 - P^{*2}}}{S_{rated}} \quad (4.12)$$

Consequently, the energy cell which provides less active power will produce more reactive power considering it has higher margin to generate reactive power. The controller will be running in the local controllers while E_{cell_avg} is received from the central controller.

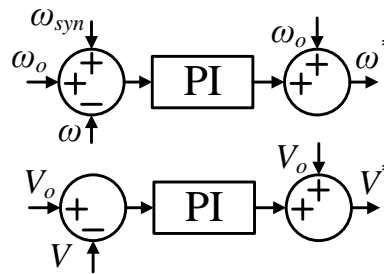


Figure 4.4 Voltage/frequency regulation control

The system voltage and frequency will deviate from the nominal value along with the system load change with the VSG control. Smaller droop coefficients help to reduce the steady state error, however, cause less power sharing accuracy. A low bandwidth control loop is introduced in the level 2 control to regulate the system voltage and

frequency for all the load conditions by adjusting the reference values ω^* , V^* in the level 1 control. The block diagram of the proposed control is given in Figure 4.4. One of the VSGs is picked to provide the measurement values ω and V (magnitude of the terminal voltage), while the generated reference values ω^* , V^* are used in all the VSGs.

4.1.2 Level 3 control

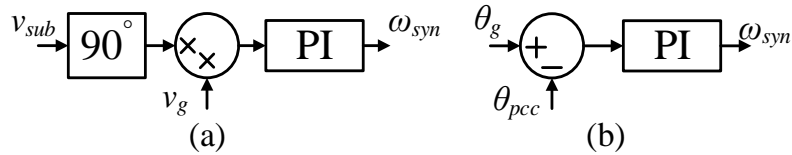


Figure 4.5 Grid synchronization loop

The level 3 control is included to deal with the swapping between islanded and grid-connected operation. Under grid-connected operation, the active and reactive power of the energy cells are directly controlled by the central controller for the power trading between the utility. In this case, the level 2 control need to be bypassed to avoid confliction of the controls. The active power command from central controller is directly assigned to P^* in Figure 4.2 and ω^* is set to the nominal value. As shown in Figure 4.6, a PI controller is used to adjust the voltage reference V^* in Figure 4.2 for tracking the reactive power command from the central controller. The value of Q^* in Figure 4.2 is set to zero in this case.

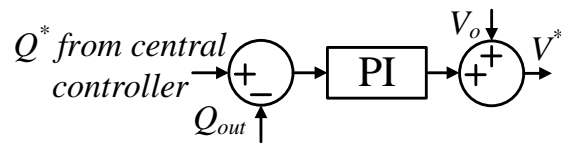


Figure 4.6 Reactive power controller under grid-connected operation

As shown in Figure 4.5 (a), a grid synchronization loop [105] is used to synchronize the voltage with the grid at the coupling point before establishing the grid connection. A

simplified representation of the synchronization loop is given as Figure 4.5 (b) which will be used in the real-time simulation. The central controller needs to send a signal to the local controllers indicating the current operating mode. Figure 4.7 shows all the information in the communication between the central controller and energy cell local controllers. Note that the main part of the grid synchronization control runs in a local controller which has the access to the voltages at the grid coupling point (before and after the breaker). The generated frequency perturbation action ω_{syn} is sent to the central controller through communication.

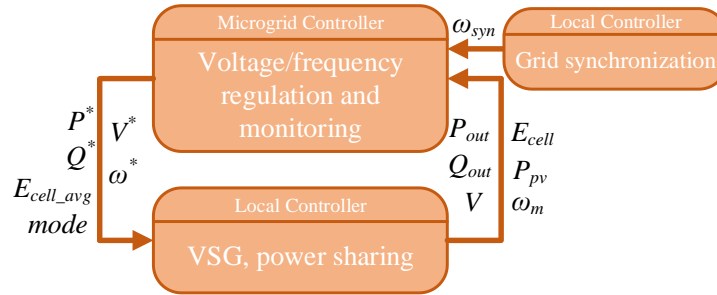


Figure 4.7 Communication between the central and local controller

4.2 Multi-platform microgrid real-time simulation testbed

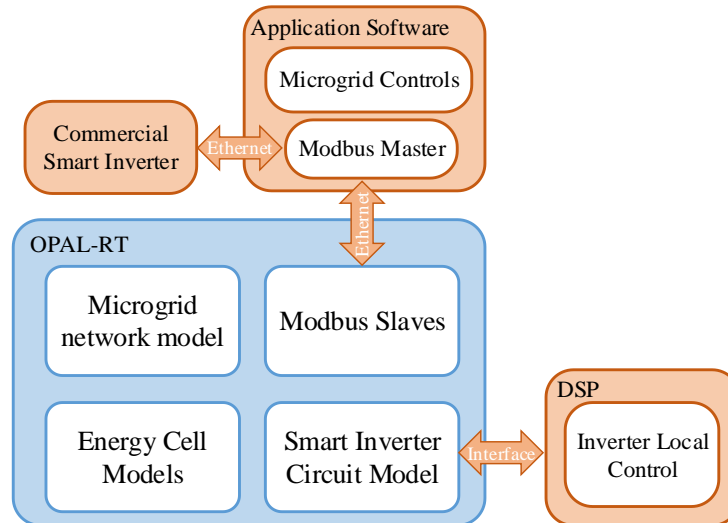


Figure 4.8 Multi-platform microgrid real-time simulation testbed

In this work, a multi-platform real-time simulation testbed is developed to validate and demonstrate the microgrid operation based on the VSGs. The overall structure of the real-time simulation testbed is shown in Figure 4.8. The testbed is developed based on a commercial power systems/power electronics real-time simulator — Opal-RT. The microgrid circuit including the network, loads and energy cells is simulated in Opal-RT while interacting with external devices such as inverter controllers and microgrid central controller. The multi-platform real-time simulation allows better validation of the proposed microgrid controls with realistic controller implementations as compared to pure software-in-loop simulation where both the controller and control target are simulated in the simulator. It is also possible to include real power hardware in the simulation loop such as a commercial smart inverter.

4.2.1 EMT-TS hybrid dynamic simulation in Opal-RT

	A	B	C	D	E	F	G	H	I	J	K
1	Bus A	Bus B	Bus C	ID	P_a (kW)	Q_a (kVAr)	P_b (kW)	Q_b (kVAr)	P_c (kW)	Q_c (kVAr)	V (kV)
2	6_a	6_b	6_c	Load_1	12.5	3.1325	12.5	3.1325	12.5	3.1325	7.2
3	21_a	21_b	21_c	Load_2	1.5333333	0.3842533	1.5333333	0.3842533	1.5333333	0.3842533	7.2
4	22_a	22_b	22_c	Load_3	32.2666667	8.0860267	32.2666667	8.0860267	32.2666667	8.0860267	7.2
5	54_a	54_b	54_c	Load_4	14.5333333	3.6420533	14.5333333	3.6420533	14.5333333	3.6420533	7.2
6	50_a	50_b	50_c	Load_5	1.4666667	0.3675467	1.4666667	0.3675467	1.4666667	0.3675467	7.2
7	24_a	24_b	24_c	Load_6	10.1	2.53106	10.1	2.53106	10.1	2.53106	7.2
8	61_a	61_b	61_c	Load_7	1.1333333	0.2840133	1.1333333	0.2840133	1.1333333	0.2840133	7.2
9	63_a	63_b	63_c	Load_8	14.2	3.55852	14.2	3.55852	14.2	3.55852	7.2
10	30_a	30_b	30_c	Load_9	33.9966667	8.5195647	33.9966667	8.5195647	33.9966667	8.5195647	7.2
11	67_a	67_b	67_c	Load_10	2.3566667	0.5905807	2.3566667	0.5905807	2.3566667	0.5905807	7.2
12	83_a	83_b	83_c	Load_11	5.0666667	1.2697067	5.0666667	1.2697067	5.0666667	1.2697067	7.2
13	35_a	35_b	35_c	Load_12	6.7333333	1.6873733	6.7333333	1.6873733	6.7333333	1.6873733	7.2
14	31_a	31_b	31_c	Load_13	9.3	2.33058	9.3	2.33058	9.3	2.33058	7.2
15	44_a	44_b	44_c	Load_14	39.4666667	9.8903467	39.4666667	9.8903467	39.4666667	9.8903467	7.2
16	48_a	48_b	48_c	Load_15	23.9666667	6.0060467	23.9666667	6.0060467	23.9666667	6.0060467	7.2
17	45_a	45_b	45_c	Load_16	34.8333333	8.7292333	34.8333333	8.7292333	34.8333333	8.7292333	7.2

Figure 4.9 Microgrid network parameters in excel sheet to be imported to ePHASORsim model

Opal-RT offers TS simulation for balanced and unbalanced power systems by the ePHASORsim software suite. As shown in Figure 4.9, the circuit parameters are prepared in Excel spreadsheet and can be automatically loaded to the simulation model. Similar to

the proposed OpenDSS simulation in Chapter 3, EMT-TS hybrid dynamic simulation illustrated in Figure 4.10 is implemented in Opal-RT to simulate the microgrid circuit. eMEGAsim is used to simulate the dynamic model of the energy cells. The dynamics related to AC quantities in the energy cells are modeled as dynamic phasors such as (4.9) for ease of interfacing with the network model. Opal-RT allows multi step size simulation in which ePHASORSim model can be solved in a larger step size than eMEGAsim model. In this work, a step size of 25 us is used for eMAGAsim model and 200 us is used for ePHASORSim model. The hybrid simulation saves tremendous computing power needed compared to the pure EMT simulation so that the system scale which can be simulate in real-time is increased.

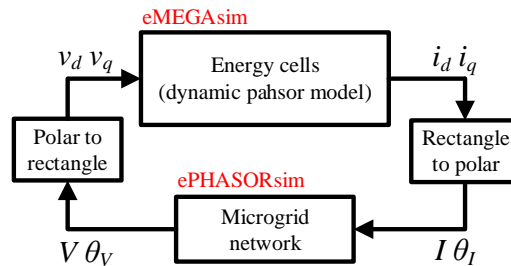


Figure 4.10 EMT-TS hybrid dynamic simulation in Opal-RT

4.2.2 Controller-hardware-in-loop (CHIL) simulation

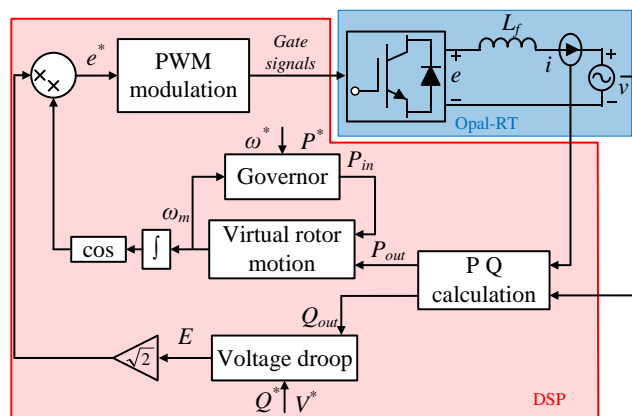


Figure 4.11 CHIL simulation of the energy cell

As shown in Figure 4.11, the proposed energy cell controls are implemented in an external real-time digital controller to control the smart inverter being simulated in Opal-RT. The simulation setup based on the real-time digital controller board EZDSP F28335 is shown in Figure 4.12. The simulated circuit voltage and current values are scaled and generated at the Opal-RT analog output to be sent to the controller board. The control signals, namely the gate signals for the smart inverter, are generated at the controller board PWM outputs to be sent back to the Opal-RT through the Opal-RT digital input ports. A customized interface board is built for signal conditioning between Opal-RT and the EZDSP F28335 controller board. A customized interface board is built for signal conditioning between Opal-RT and the EZDSP F28335 controller board.

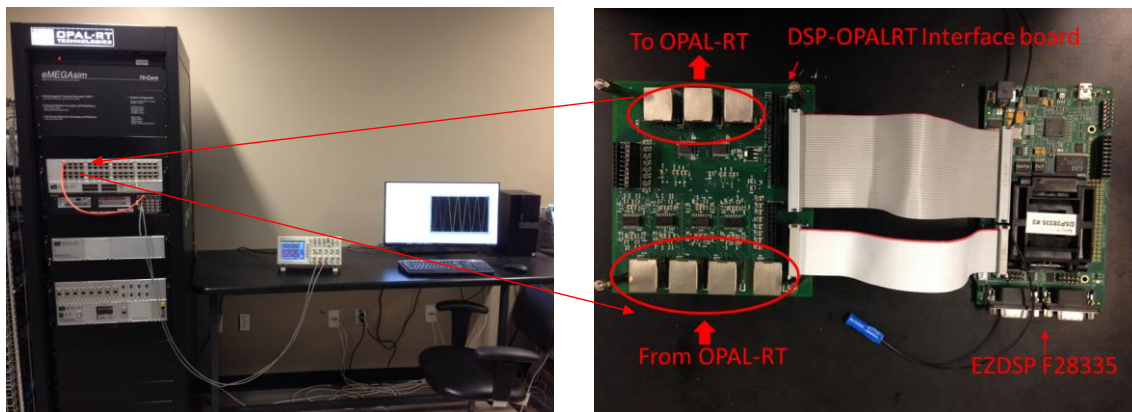


Figure 4.12 CHIL simulation setup for validating the inverter local controls

4.2.3 Simulation with remote microgrid central controller

A communication network is needed between the microgrid controller and the smart inverters at different locations in the microgrid. To simulate the realistic scenario, a realistic communication network based on Modbus [103] is established in the real-time simulation testbed. With the communication network, the microgrid controller running on a remote system can communicate with the smart inverters being simulated in Opal-RT.

Moreover, real smart inverters which support the same communication protocol can be included in the testbed through the communication network.

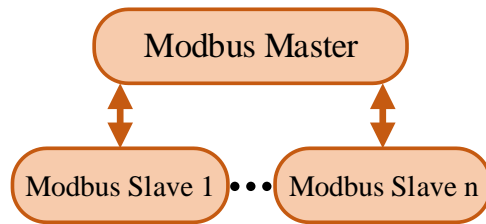


Figure 4.13 Modbus based communication network

Modbus is an open source communication protocol which is widely used to connect electronic devices in many industries. Modbus is supported by many of the commercial PV inverters from manufacturers such as ABB, SMA and Fronius. It is being used for system communication in PV power plants. As shown in Figure 4.13, a master-slave communication structure is proposed where the Modbus master is implemented for the microgrid central controller and the Modbus slaves are implemented for the local controllers. The Ethernet based Modbus (Modbus TCP) is used where the master can find the slaves through IP address. There can be up to 247 slaves in a Modbus communication network. The master can request data from the slave units and write data to the registers of slave units. The Modbus slaves are implemented in Opal-RT by using OpModbus and combined with the energy cell model by connecting the OpModbus block with the corresponding measurements and control signals. As shown in Table 4.1, a register mapping is used for both the Modbus master and slaves to identify the data in corresponding registers. The block diagrams of the implemented Opal-RT models are given in the Appendix.

Table 4.1 Energy cell Modbus mapping

Holding Registers	Description	Input Registers	Description	Input Registers	Description
1	Control mode (1: islanded mode, 0: grid-connected mode)	1	$ I_A $ in A	8	P_{pv} in kW
2	P_o in kW	2	$\angle I_A$ in degree	9	E_{cell} in kWh
3	Q_o in kVAr	3	$ V_A $ in V		
4	ω_o in 0.01 rad/s	4	$\angle V_A$ in degree		
5	V_o in V	5	P_{out} in kW		
6	E_{avg} in kWh	6	Q_o in kVAr		
		7	ω_m in 0.01 rad/s		

4.3 A microgrid test case based on IEEE 123 node test feeder

4.3.1 Microgrid configuration

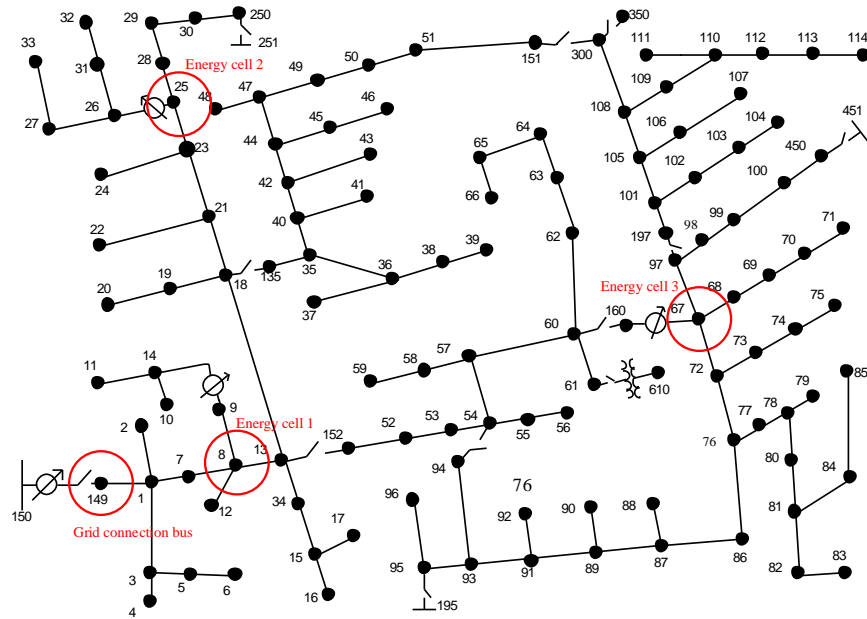


Figure 4.14 IEEE 123 node test feeder based microgrid

A microgrid based on IEEE 123 node test feeder has been modeled to demonstrate the proposed microgrid controls in the real-time simulation testbed. As shown in Figure 4.14, energy cells are put at buses near the locations of voltage regulators in the original feeder. For simplicity, the voltage regulators are not modeled in the simulation. A Modbus

slave is modeled for each of the local controllers in the energy cells and the grid synchronization controller at the grid connection. The connection to the utility grid is controlled by a switch modeled between bus 150 and 149.

4.3.2 Energy cell specifications

The energy cell specifications are given in Table 4.2. The MVA and voltage ratings are picked from typical values of commercial grid-connected inverters. The virtual inertia is calculated based on an inertia constant of 2.5 [107]. The impact of the droop coefficients and inverter output impedance on system stability has been discussed in [101], however, the systematic design method of the actual values has not been reported in the literature. In this work, these values are tuned in simulations to ensure the system stability. Large and inductive inverter output impedance is preferred to ensure system stability and power sharing accuracy of the droop controls in low voltage distribution network. The output impedance of the inverter can be modified without changing the actual grid filter value, such as the control-based method in which the different inverter output impedance is achieved by emulating a virtual impedance in the control scheme [108]. For simplicity, the inverter output impedance is modified by changing the passive grid filter value in the simulation. To match the system load level in the simulation, the output current of the inverters is scaled by 10 to represent MW level energy cells at bus 8, 25, 67.

Table 4.2 Energy cell specifications

Power rating S_{rate}	300 kVA
Nominal voltage	480 V _{L-L}
Droop coefficient m_p	5e-3 rad/s/kW
Droop coefficient m_{qo}	5e-2 V/kVAr
Output impedance z_o	0.1 + j0.8 Ω
Virtual inertia J	5*S _{rate} /(2 π 60) ²
Nominal storage level E_o	S _{rate} * 10 mins

4.3.3 Controller design

The voltage regulation controller in level 2 control compensates the steady state error of the system voltage under different load conditions. A step change is applied to the voltage reference V^* and the response of the system voltage is shown in Figure 4.15. Based on the step response, the small signal transfer function from the voltage reference to the system voltage is estimated by

$$G_{V^* \rightarrow V} = \frac{415}{s + 750} \quad (4.13)$$

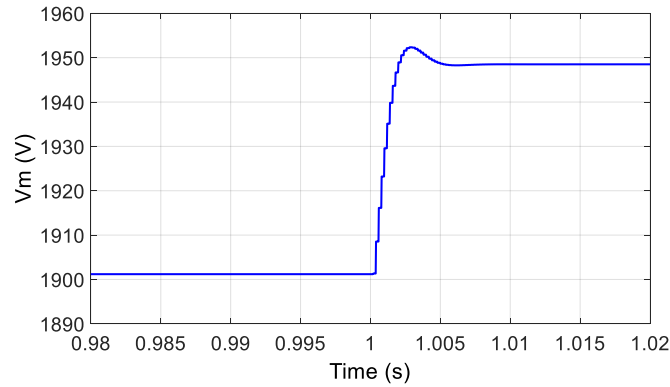


Figure 4.15 Step response of system voltage by changing the voltage reference

Considering a transfer function G_{c1} as the voltage regulation controller, the voltage regulation loop gain is $G_{c1}G_{V^* \rightarrow V}$. By designing the loop bandwidth as 2 rad/s and 90° phase margin, G_{c1} can be calculated as

$$G_{c1} = \frac{0.0047s + 3.6}{s} \quad (4.14)$$

The closed-loop stability needs to be checked considering the impact of communication delay in the control loop. Assuming the communication delay is 250 ms, the induced phase

delay at the crossover frequency is less than 30° . The closed-loop system is stable since the designed phase margin is 90° .

The frequency regulation controller is used to compensate the steady state error of the system frequency under different load conditions. To design the controller, the transfer function from the frequency reference to the system frequency is estimated based on the step response shown in Figure 4.16:

$$G_{\omega^* \rightarrow \omega} = \frac{60}{s + 60} \quad (4.15)$$

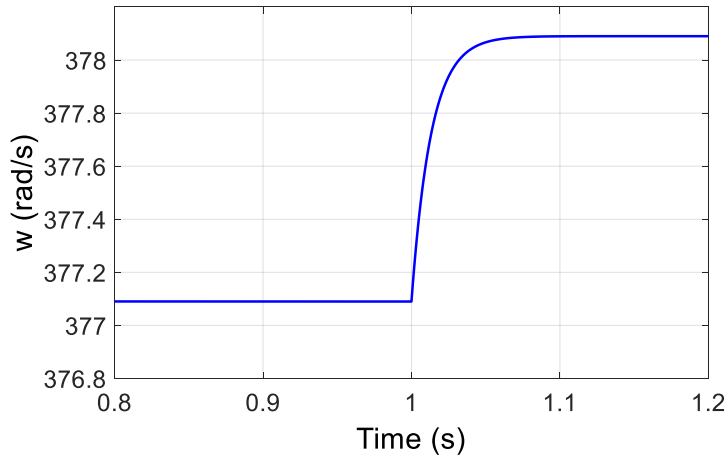


Figure 4.16 Step response of system frequency by changing the frequency reference
Assuming the desired loop bandwidth is 2 rad/s and the phase margin is 90° , the calculated controller transfer function of the frequency regulation controller is

$$G_{c2} = \frac{0.034s + 2}{s} \quad (4.16)$$

To design the dynamic power sharing controller, the small-signal transfer function from the power reference P^* to the inverter power output is estimated based on the step response shown in Figure 4.17. The estimated transfer function is

$$G_{P^* \rightarrow P} = \frac{1}{s + 1.5} \quad (4.17)$$

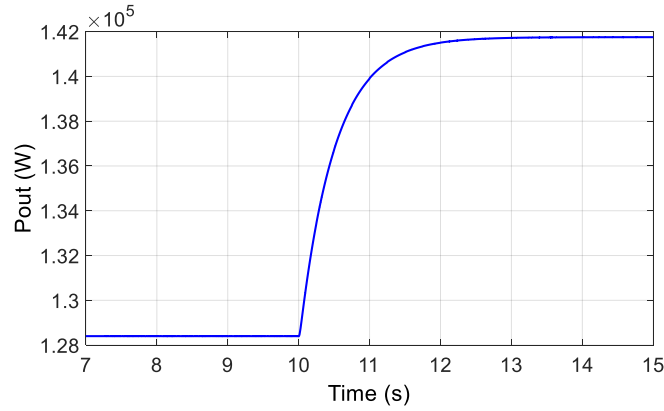


Figure 4.17 Step response of inverter power output by changing the power reference

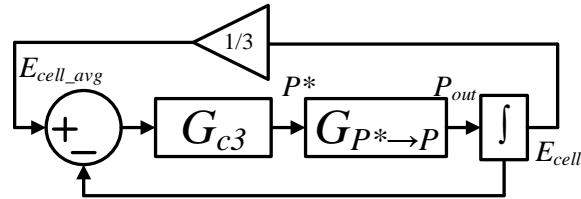


Figure 4.18 Small-signal model of the dynamic power sharing loop

As shown in Figure 4.18, the loop transfer function of the dynamic power sharing loop is

$\frac{2}{3} G_{c3} G_{P^* \rightarrow P}$. The loop bandwidth is designed as 0.02 rad/s. The following controller transfer

function corresponds to a phase margin of 60° :

$$G_{c3} = \frac{0.039s + 0.00044}{s} \quad (4.18)$$

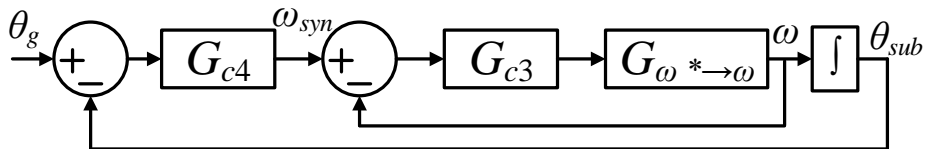


Figure 4.19 Small-signal model of the grid synchronization loop

The small-signal model of the grid synchronization loop is shown in Figure 4.19. The

bandwidth of the outer loop is designed as one fifth of the inner loop bandwidth, which is

0.2 rad/s. To achieve a 60° phase margin, the grid synchronization controller is designed as

$$G_{c4} = \frac{0.176s + 0.016}{s} \quad (4.19)$$

4.4 Simulation results of IEEE 123 node test feeder configured as microgrid

4.4.1 Grid-connected operation

The grid-connected operation of the microgrid is simulated with the switch between bus 149 and 150 closed. The total number of the active power load and reactive power load in the network are 3.4 MW and 1.2 MVAR respectively. In Figure 4.20, a step change of the active power command from {1000 kW, 800 kW, 500 kW} to {1200 kW, 800 kW, 500 kW} is given to the energy cell controllers. In Figure 4.21, a step change of the reactive power command from {0 kVAr, 0 kVAr, 0 kVAr} to {100 kVAr, 0 kVAr, 0 kVAr} is given to the energy cell controllers. The simulation result shows a perfect tracking of the power commands for the energy cells under grid-connected operation mode.

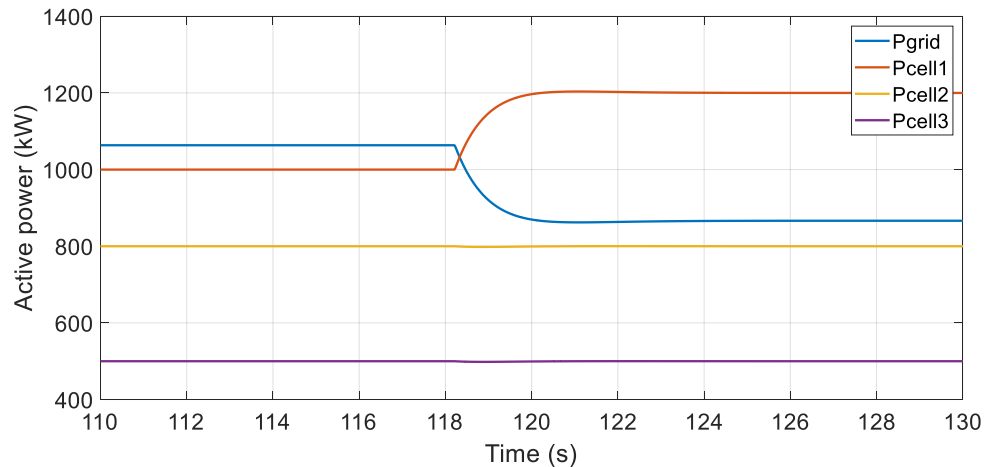


Figure 4.20 Step change of inverter active power output under grid-connected operation

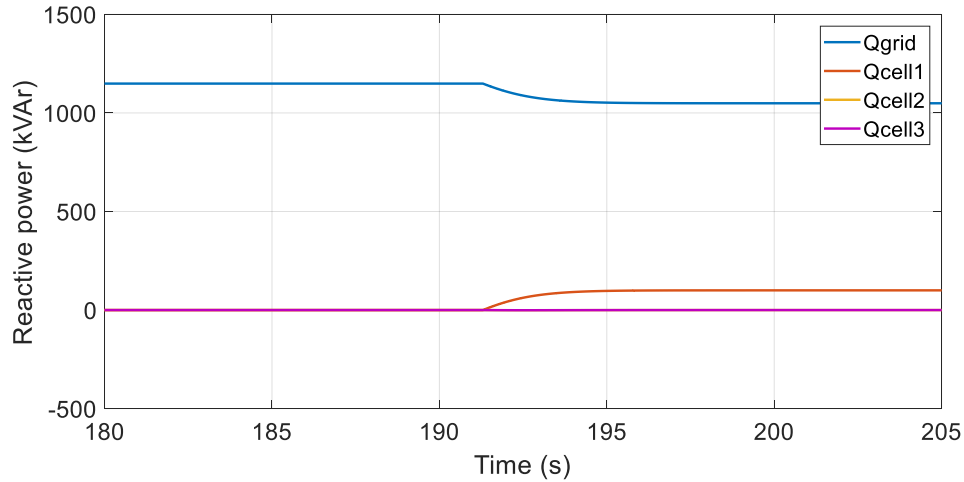


Figure 4.21 Step change of inverter reactive power output under grid-connected operation

4.4.2 Islanded microgrid operation

System voltage and frequency regulation

The islanded microgrid operation is simulated with the switch between bus 149 and 150 open. In the simulation, the angular frequency and terminal voltage of the inverter in energy cell 1 (at bus 8) are taken as the measurement for system frequency and voltage regulation. The load at bus 47, 48, 49, 65 and 76 are firstly switched off and then switched on in the simulation. The total number of the switching load is 840 kW + 600 kVAr. The frequency and voltage response of the load step change are shown in Figure 4.22 and Figure 4.23. The corresponding inverter power outputs are shown in Figure 4.24 and Figure 4.25. As shown in the simulation results, both the system voltage and frequency are well regulated by the proposed controls.

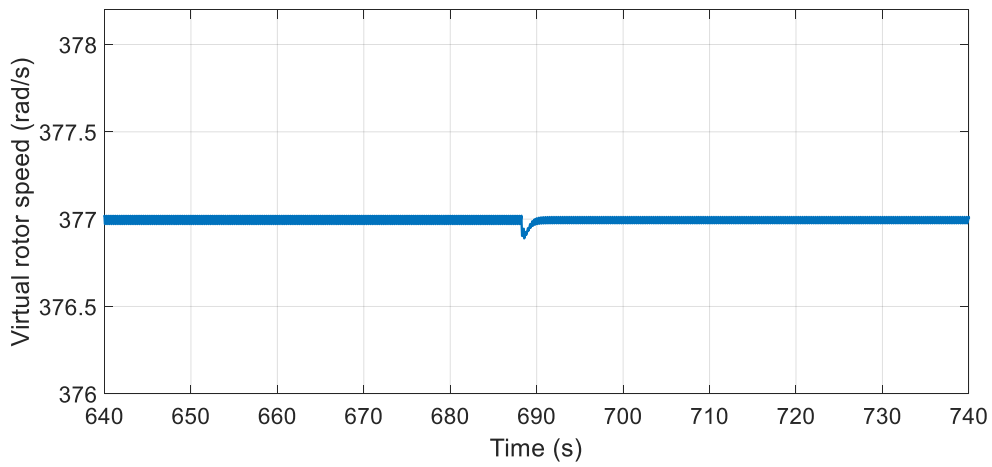


Figure 4.22 Inverter angular frequency under system load step change

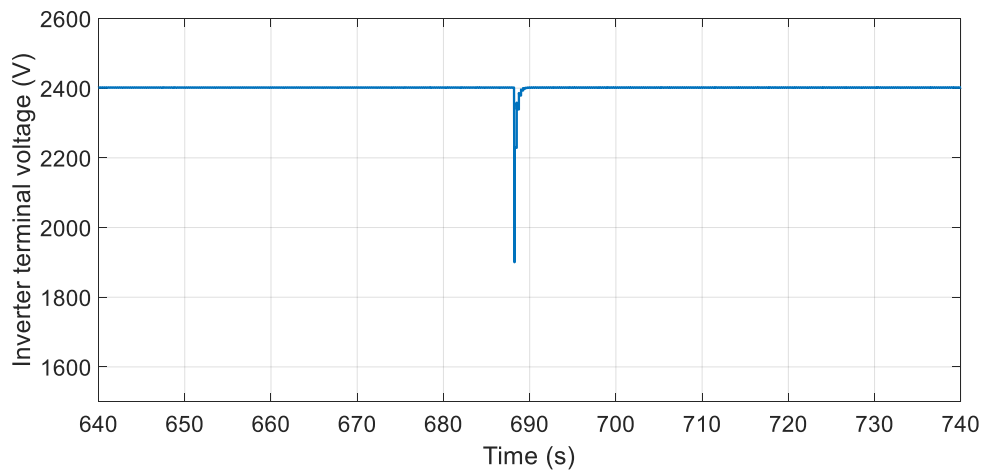


Figure 4.23 Inverter terminal voltage under system load step change

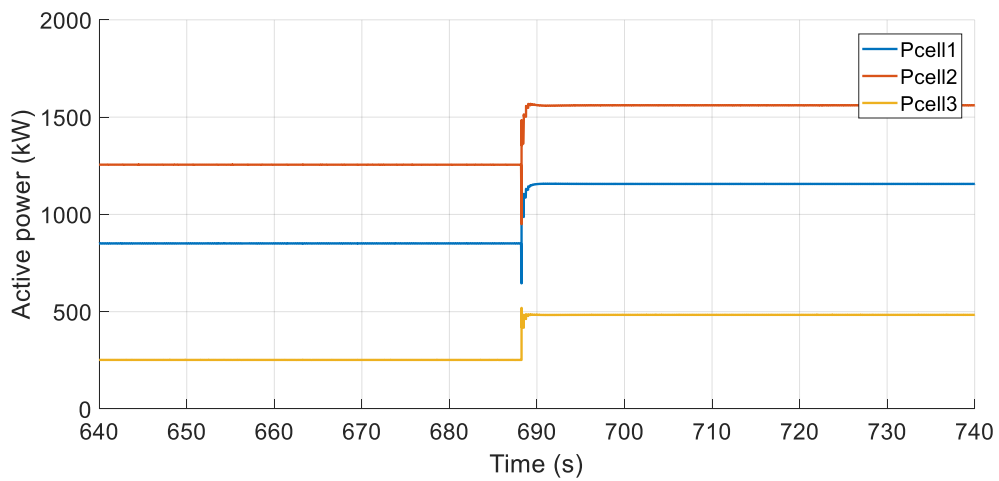


Figure 4.24 Inverter active power output under system load step change

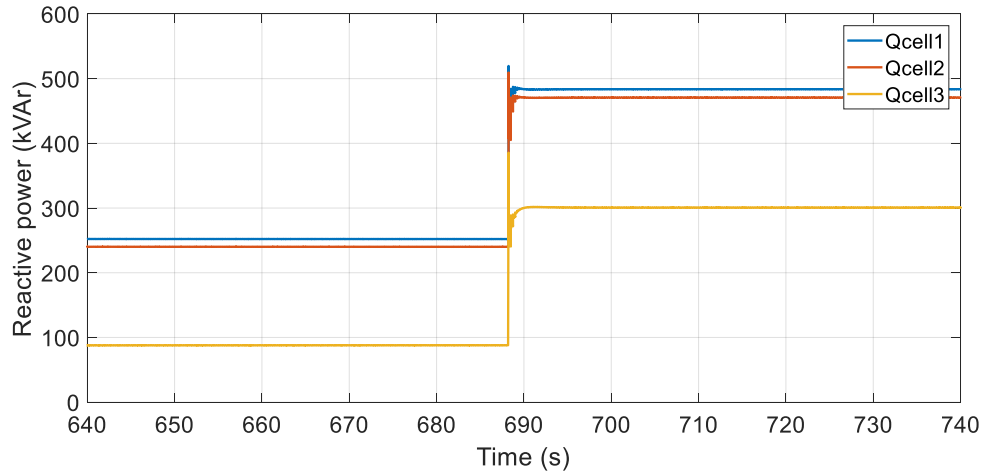


Figure 4.25 Inverter reactive power output under system load step change

Dynamic power sharing among the energy cells

As shown in Figure 4.26, three different PV generation profiles are used for the energy cells to demonstrate the dynamic power sharing control. The PV generation profiles are created based on one-day historical data of three real power plants [102]. The power values are scaled up to match the system load level. The time scale of the generation data is compressed 100 times faster (24 hours into 14 minutes) for simulation. The simulation result of inverter active power output and the energy storage level of the energy cells are given in Figure 4.27 and Figure 4.28. As seen in the result, the active power sharing among the energy cells is constantly adapted by the power sharing controller to achieve a balanced charging/discharging of the energy cells. In the meantime, the reactive power sharing is adapted based on (4.11) and (4.12). Figure 4.29 shows the waveform of the inverter reactive power outputs in the simulation.

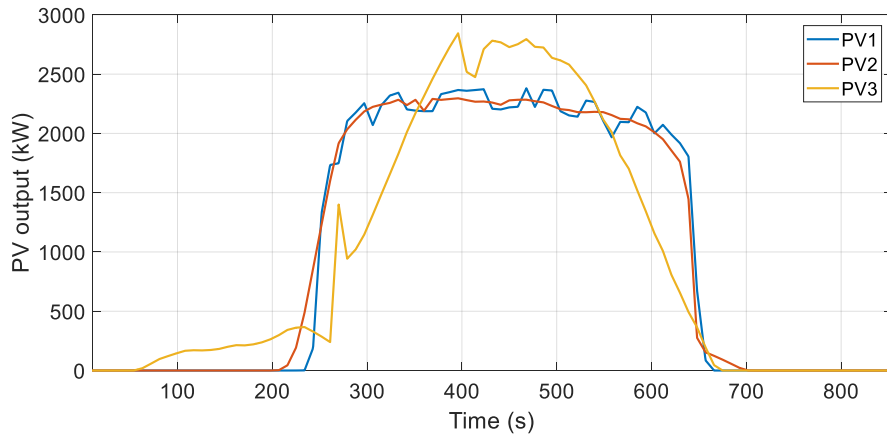


Figure 4.26 PV generation profile

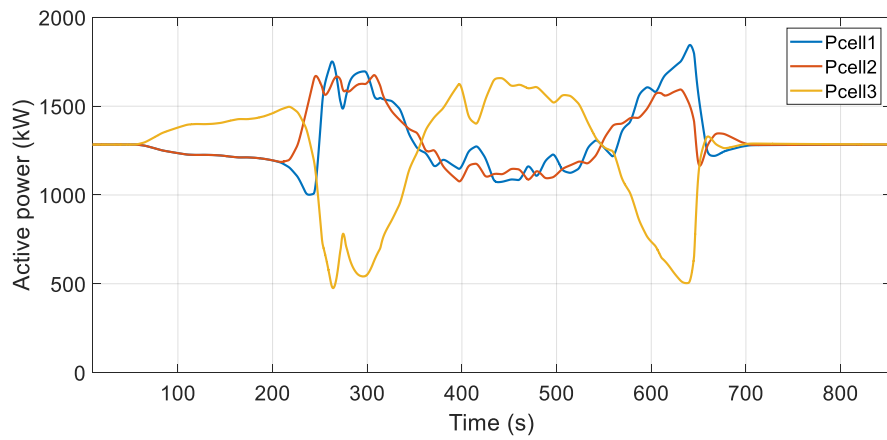


Figure 4.27 Inverter active power output varying with PV generation

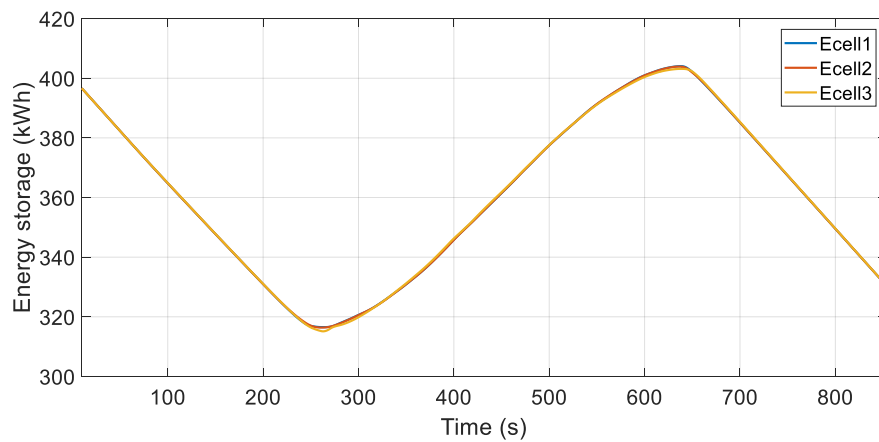


Figure 4.28 Cell energy level varying with PV generation

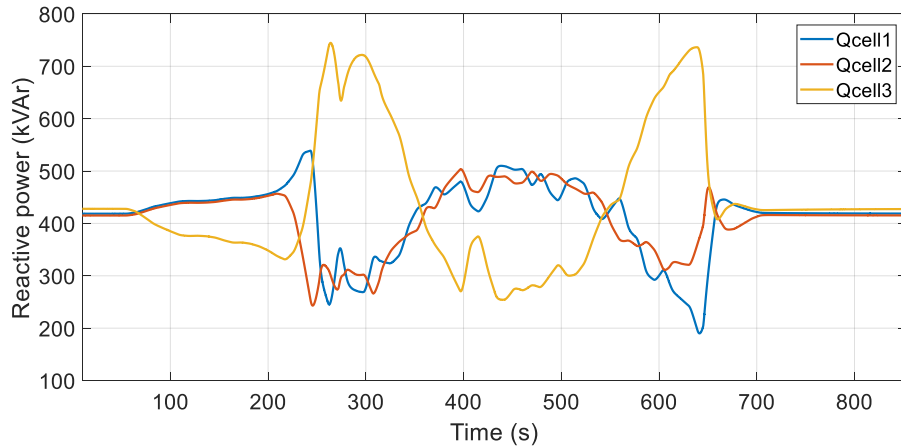


Figure 4.29 Inverter reactive power output varying with PV generation

Grid synchronization control

The simulation result of the grid synchronization control is shown in Figure 4.30. In the beginning of the simulation, a 60° phase difference is created between the voltage at bus 149 and 150 and the grid synchronization loop is deactivated until 60 s. The simulation result shows that the voltage angle at bus 149 becomes synchronized with the grid in about 1 minute after the grid synchronization loop is activated.

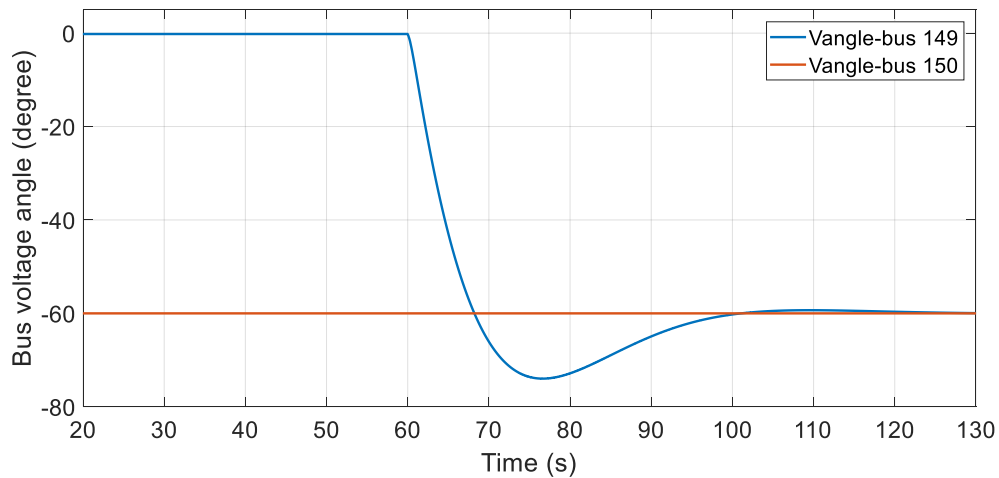


Figure 4.30 Simulation result of grid synchronization control

4.5 Dynamic load modeling

The common load models used in system level simulation includes constant impedance load, constant current load and constant power load. However, these models are not always suitable in dynamic studies especially when the dynamic interaction of a specific load type has significant impact on the system response. A famous example is the stalling effect of air conditioner compressor motors under system faults. The impact of the air conditioner loads on the proposed inverter based microgrid is explored by including the dynamic model of air conditioner compressor motors in the simulation.

4.5.1 Modeling of AC compressor motor

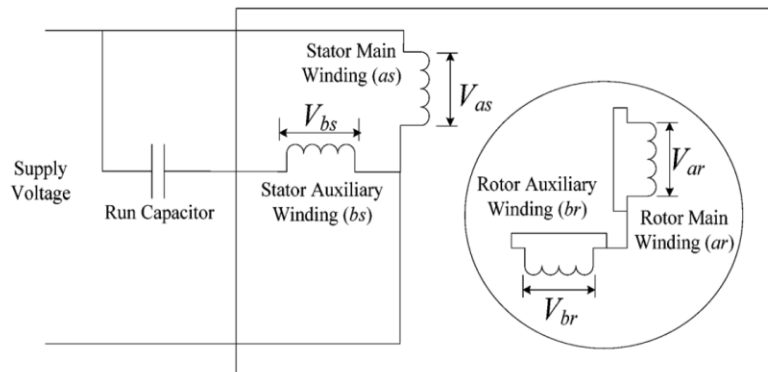


Figure 4.31 Structure of air-conditioner compressor single-phase induction motor [109]

The structure of air-conditioner compressor single-phase induction motor is shown in Figure 4.31. It is a permanent-split capacitor motor where a second phase (stator auxiliary winding) is added to the motor in which a run capacitor is connected in series with the coil. The auxiliary stator winding current leads the main winding current by 90° . The equations of the winding voltages with respect to flux linkage and winding currents can be given as

$$\begin{bmatrix} v_{as} \\ v_{bs} \\ v_{ar} \\ v_{br} \end{bmatrix} = \begin{bmatrix} \frac{d\lambda_{as}}{dt} \\ \frac{d\lambda_{bs}}{dt} \\ \frac{d\lambda_{ar}}{dt} \\ \frac{d\lambda_{br}}{dt} \end{bmatrix} + \begin{bmatrix} r_s & 0 & 0 & 0 \\ 0 & r_s & 0 & 0 \\ 0 & 0 & r_{cage} & 0 \\ 0 & 0 & 0 & r_{cage} \end{bmatrix} \begin{bmatrix} i_{as} \\ i_{bs} \\ i_{ar} \\ i_{br} \end{bmatrix} \quad (4.20)$$

where r_s is the stator winding resistance and r_{cage} is the rotor resistance. The flux linkage vector in (4.20) can be written as

$$\begin{bmatrix} \lambda_{as} \\ \lambda_{bs} \\ \lambda_{ar} \\ \lambda_{br} \end{bmatrix} = \begin{bmatrix} L_m + L_s & 0 & L_m \cos \theta & L_m \sin \theta \\ 0 & N^2 L_m + N^2 L_s & -NL_m \sin \theta & NL_m \cos \theta \\ L_m \cos \theta & -NL_m \sin \theta & L_m + L_r & 0 \\ L_m \sin \theta & NL_m \cos \theta & 0 & L_m + L_r \end{bmatrix} \begin{bmatrix} i_{as} \\ i_{bs} \\ i_{ar} \\ i_{br} \end{bmatrix} \quad (4.21)$$

where L_m is the mutual inductance between the stator main winding and the rotor winding, L_s is the leakage inductance of the stator winding; N is the turns ratio from the stator auxiliary winding to the stator main winding, θ is the rotor position relative to the stator structure. Substitute the flux linkage in (4.20) by (4.21), the voltage equations become

$$\begin{bmatrix} v_{as} \\ v_{bs} \\ v_{ar} \\ v_{br} \end{bmatrix} = \begin{bmatrix} L_m + L_s & 0 & L_m \cos \theta & L_m \sin \theta \\ 0 & N^2 L_m + N^2 L_s & -NL_m \sin \theta & NL_m \cos \theta \\ L_m \cos \theta & -NL_m \sin \theta & L_m + L_r & 0 \\ L_m \sin \theta & NL_m \cos \theta & 0 & L_m + L_r \end{bmatrix} \begin{bmatrix} \frac{di_{as}}{dt} \\ \frac{di_{bs}}{dt} \\ \frac{di_{ar}}{dt} \\ \frac{di_{br}}{dt} \end{bmatrix} + \begin{bmatrix} 0 & 0 & -\omega L_m \sin \theta & \omega L_m \cos \theta \\ 0 & 0 & -\omega NL_m \cos \theta & -\omega NL_m \sin \theta \\ -\omega L_m \sin \theta & -\omega NL_m \cos \theta & 0 & 0 \\ \omega L_m \cos \theta & -\omega NL_m \sin \theta & 0 & 0 \end{bmatrix} \begin{bmatrix} i_{as} \\ i_{bs} \\ i_{ar} \\ i_{br} \end{bmatrix} + \begin{bmatrix} r_s & 0 & 0 & 0 \\ 0 & r_s & 0 & 0 \\ 0 & 0 & r_{cage} & 0 \\ 0 & 0 & 0 & r_{cage} \end{bmatrix} \begin{bmatrix} i_{as} \\ i_{bs} \\ i_{ar} \\ i_{br} \end{bmatrix} \quad (4.22)$$

The stator auxiliary winding voltage can be expressed by the voltage difference between the stator main winding and the run capacitor:

$$v_{bs} = v_{as} - v_c \quad (4.23)$$

The equation between the run capacitor voltage and the stator auxiliary winding current is

$$\frac{dv_c}{dt} = \frac{1}{C} i_{bs} \quad (4.24)$$

Combining (4.22)-(4.24) and rearrange the equation, the dynamic equation of the permanent split-capacitor motor is written as

$$\begin{bmatrix} \frac{di_{as}}{dt} \\ \frac{di_{bs}}{dt} \\ \frac{di_{ar}}{dt} \\ \frac{di_{br}}{dt} \\ \frac{dv_c}{dt} \end{bmatrix} = [A_{5 \times 5}] \begin{bmatrix} i_{as} \\ i_{bs} \\ i_{ar} \\ i_{br} \\ v_c \end{bmatrix} + [B_{5 \times 5}] \begin{bmatrix} v_s \\ v_s \\ 0 \\ 0 \\ 0 \end{bmatrix} \quad (4.25)$$

where

$$[A_{5 \times 5}] = \begin{bmatrix} L_m + L_s & 0 & L_m \cos \theta & L_m \sin \theta & 0 \\ 0 & N^2(L_m + L_s) & -NL_m \sin \theta & NL_m \cos \theta & 0 \\ L_m \cos \theta & -NL_m \sin \theta & L_m + L_r & 0 & 0 \\ L_m \sin \theta & NL_m \cos \theta & 0 & L_m + L_r & 0 \\ 0 & 0 & 0 & 0 & C \end{bmatrix}^{-1} \begin{bmatrix} -r_s & 0 & \omega L_m \sin \theta & -\omega L_m \cos \theta & 0 \\ 0 & -r_s & \omega NL_m \cos \theta & \omega NL_m \sin \theta & -1 \\ \omega L_m \sin \theta & \omega NL_m \cos \theta & -r_{cage} & 0 & 0 \\ -\omega L_m \cos \theta & \omega NL_m \sin \theta & 0 & -r_{cage} & 0 \\ 0 & 1 & 0 & 0 & 0 \end{bmatrix} \quad (4.26)$$

$$[B_{5 \times 5}] = \begin{bmatrix} L_m + L_s & 0 & L_m \cos \theta & L_m \sin \theta & 0 \\ 0 & N^2(L_m + L_s) & -NL_m \sin \theta & NL_m \cos \theta & 0 \\ L_m \cos \theta & -NL_m \sin \theta & L_m + L_r & 0 & 0 \\ L_m \sin \theta & NL_m \cos \theta & 0 & L_m + L_r & 0 \\ 0 & 0 & 0 & 0 & C \end{bmatrix}^{-1} \quad (4.27)$$

The corresponding dynamic phasor model can be derived based on (3.7) (3.8) and (4.25).

The rotor resistance r_{cage} is function of the rotor angular velocity (ω):

$$r_{cage} = \begin{cases} rr & \omega \geq \omega_o \\ rr \left(k_1 - k_2 \frac{\omega}{\omega_o} \right) & \omega < \omega_o \end{cases} \quad (4.28)$$

where rr is the static rotor winding resistance, k_1 and k_2 are the characteristic constants.

The saturation effect of the mutual inductance L_m is modeled by

$$L_m = \frac{L_{unsat}}{1 + S(\lambda)} \quad (4.29)$$

$$S(\lambda) = \begin{cases} a(\lambda - b)^2 & \lambda > b \\ 0 & \lambda \leq b \end{cases} \quad (4.30)$$

where a and b are the characteristic constants which can be determined based on the saturation curve, λ is calculated by

$$\lambda = \frac{\sqrt{\lambda_{as}^2 + \lambda_{bs}^2}}{\lambda_{base}} \quad (4.31)$$

The electro-magnetic torque is calculated by

$$\begin{aligned} T_e = & (\lambda_{as} - L_s i_{as})(-i_{ar} \sin \theta + i_{br} \cos \theta) \\ & - (\lambda_{bs} - N^2 L_s i_{bs})(i_{ar} \cos \theta + i_{br} \sin \theta) \end{aligned} \quad (4.32)$$

The rotor motion equations are given by

$$\frac{d\omega}{dt} = \frac{T_e - T_{mech}}{H_r} \quad (4.33)$$

$$\frac{d\theta}{dt} = \omega \quad (4.34)$$

where H_r is the rotor moment of inertia and T_{mech} is the mechanical load torque. As shown Figure 4.32, the mechanical load torque varies with the rotor position when rotor is spinning at constant speed. The MATLAB function of the air conditioner compressor motor dynamic phasor model is given in the Appendix.

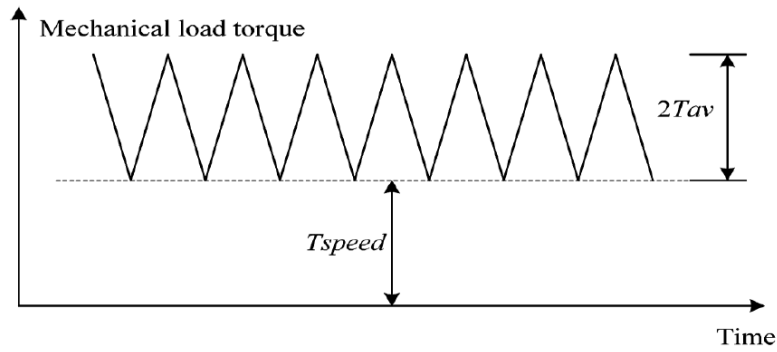


Figure 4.32 Mechanical load torque at constant speed [109]

4.5.2 Inverter current limiting scheme under fault condition

The air conditioner compressor motor can stall when the terminal voltage drops below 60% of the nominal voltage, which can be caused by system fault [110]. Once the motor goes into stall mode, it won't restart even after the terminal voltage is recovered. The stalled motor draws a higher current than the normal operation. This phenomenon could stop the system from recovering after fault is cleared in a network with high penetration of air conditioner loads. To show the impact of the air conditioner loads on the inverter based microgrid, a current limiting scheme for the smart inverter to ride through faults is modeled. Without the current limiting scheme, the inverter is likely to be tripped off during the fault due to the limited capability of operating under overcurrent condition.

The current limiting is realized by increasing the output impedance of the inverter during fault condition. The variable impedance can be realized by external hardware [111] [112] or the inverter itself [113]. Figure 4.33 shows a fault current limiting scheme added to the VSG control based on the virtual impedance scheme in [113]. To emulate an inductive impedance in series with the inverter, a voltage-drop term e_{vi} calculated by

$$e_{vi} = L_{vi} \frac{sp}{s+p} i \quad (4.35)$$

is subtracted from the original voltage reference. p in (4.35) is a high frequency pole which is included in the real implement of derivative calculation. Expressed with phasors, (4.35) is written in two-dimension state space form:

$$\begin{bmatrix} \dot{x}_1 \\ \dot{x}_2 \end{bmatrix} = \begin{bmatrix} -p & \omega_o \\ -\omega_o & -p \end{bmatrix} \begin{bmatrix} x_1 \\ x_2 \end{bmatrix} + \begin{bmatrix} i_d \\ i_q \end{bmatrix} \quad (4.36)$$

$$\begin{bmatrix} e_{vid} \\ e_{viq} \end{bmatrix} = \begin{bmatrix} -L_{vi}p^2 & 0 \\ 0 & -L_{vi}p^2 \end{bmatrix} \begin{bmatrix} x_1 \\ x_2 \end{bmatrix} + \begin{bmatrix} L_{vi}p & 0 \\ 0 & L_{vi}p \end{bmatrix} \begin{bmatrix} i_d \\ i_q \end{bmatrix} \quad (4.37)$$

The virtual impedance L_{vi} is given by

$$L_{vi} = \begin{cases} k_{vi} \frac{(I - I_{max})}{I_{max}} L_{base} & I > I_{max} \\ 0 & I \leq I_{max} \end{cases} \quad (4.38)$$

where I is the magnitude of the inverter output current and I_{max} is the threshold value. L_{base} is inductance value by which the inverter short circuit current equals to I_{max} . k_{vi} is large gain which limits the inverter output current close to I_{max} under fault or overloading conditions. In the end, the maximum L_{vi} value is limited to L_{base} . To avoid confliction between the controls, the voltage regulation in the level 2 control needs to be disabled.

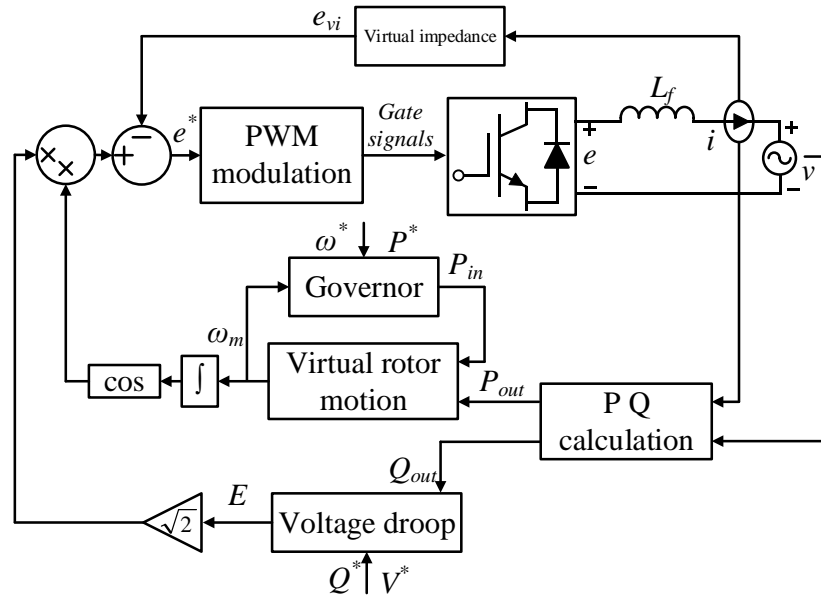


Figure 4.33 Fault current limiting based on virtual impedance control

4.5.3 Simulation results

Machine model validation

The parameters in [109] is used to create a dynamic phasor model of the air conditioner compressor motor, the main parameters are given in Table 4.3. A comparison with the simulation result obtained from the original machine model [109] is carried out to validate the accuracy of the developed model. Figure 4.34 shows the simulation results of the stator main winding current. Figure 4.35 shows the rotor angular speed. In the simulation, a voltage dip to 40% of the rated voltage is applied to the machine terminal at 10 s. The machine stalls in a very short time after the voltage drop is applied. The machine terminal voltage is recovered at 10.2 s, however, the machine stays in stall mode and draws even higher current than that during the voltage dip. As seen in the simulation results, the developed dynamic phasor model generates very similar results as the original model.

Table 4.3 Air conditioner compressor induction machine parameters

Rated voltage	$V_{rated} = 230 \text{ V}$	Unsaturated mutual inductance between stator main winding and rotor winding	$L_{m_unsat} = 79.58 \text{ mH}$
Rated current	$I_{rated} = 23 \text{ A}$	Saturation function coefficients	$a = 0.511 \quad b = 0.758$
Rated speed	$\omega_{rated} = 377 \text{ rad/s}$	Stator winding leakage inductance	$L_s = 1.33 \text{ mH}$
Load power	$P_{rated} = 5.3 \text{ kW}$ ($T_{speed} = 6 \text{ Nm}$, $T_{av} = 8 \text{ Nm}$)	Rotor winding leakage inductance	$L_r = 0.53 \text{ mH}$
Stator winding resistance	$r_s = 0.3 \text{ ohms}$	Turns ratio of stator auxiliary winding to stator main winding	$N = 1.4$
Static rotor winding resistance	$r_r = 0.3 \text{ ohms}$	Run capacitor	$C = 40 \text{ uF}$
Rotor cage resistance coefficients	$k_1 = 5 \text{ p.u.}$ $k_2 = 4 \text{ p.u.}$	Rotor moment of inertia	$H_r = 0.00273 \text{ kgm}^2$

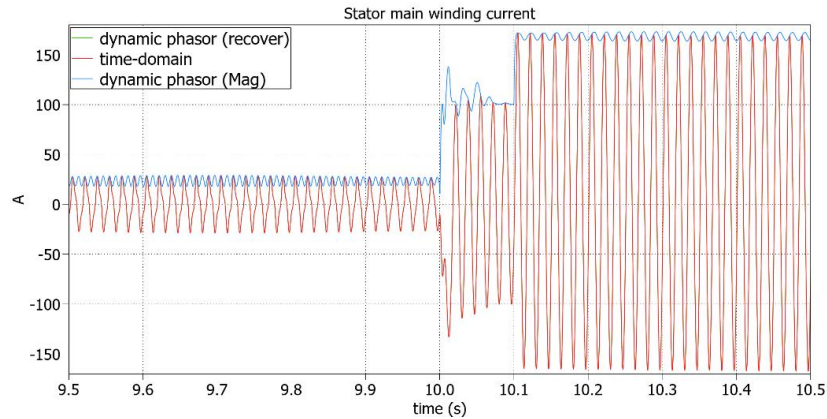


Figure 4.34 Simulation result comparison: stator main winding current under terminal voltage drop

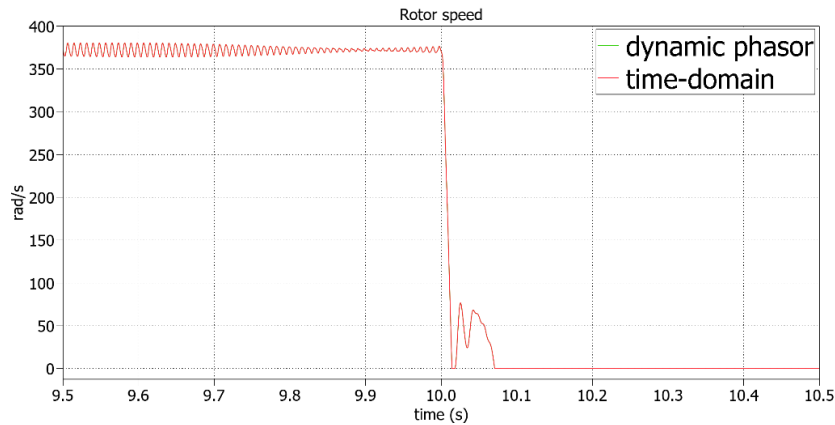


Figure 4.35 Simulation result comparison: rotor angular speed under terminal voltage drop

Fault response in inverter based microgrid

A single-phase to ground fault on phase A of bus 149 is applied on the IEEE 123 node test feeder microgrid which includes three inverters as shown in Figure 4.14. In the first case, the original feeder model is used where the loads are modeled by static load models including constant I , constant Z and constant P loads. The simulation results are shown in Figure 4.36 and Figure 4.37. The fault is applied at around 3.7 s and is cleared after 0.2 s. Figure 4.36 shows the phase A output current magnitude of the inverters. The inverter output current is well limited to the threshold value during the fault which is 277.5 A for all the inverters. Figure 4.37 shows the inverter terminal voltages of phase A. As shown in figure, the inverter terminal voltages drop to less than 15% of the nominal value during the fault. The virtual impedance is set to zero after the fault is cleared and both the current and voltage come back to the values before the fault.

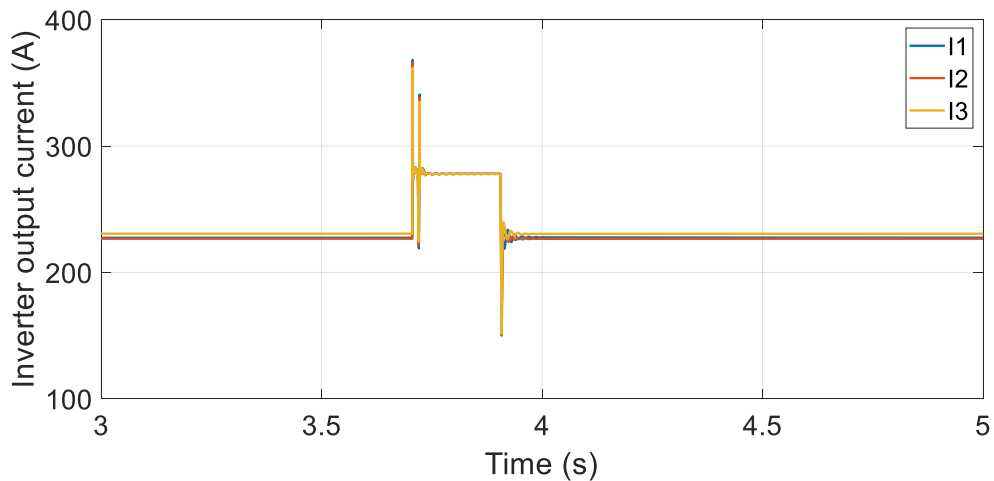


Figure 4.36 Inverter output current under system fault with constant impedance, constant current and constant power load

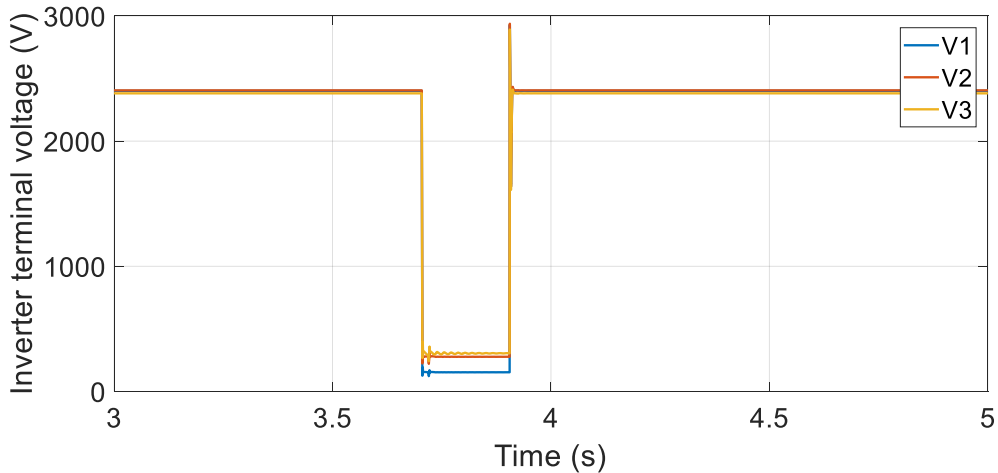


Figure 4.37 Inverter terminal voltage under system fault with constant impedance, constant current and constant power load

In the second case, 220 kW load on bus 76 is modeled as the air conditioner load by using the developed dynamic phasor model. The machine terminal current is scaled to match the power level. The machine electro-magnetic torque, mechanical torque and the rotor angular speed following the same fault as the first case are shown in Figure 4.38 and Figure 4.39. The machine stalls during the fault and stay in the stall mode after the fault is cleared. The machine terminal voltage and current are shown in Figure 4.40. It shows that the machine draws four times higher current after the fault is cleared than the normal condition due to stalling. As shown in Figure 4.41 and Figure 4.42, the inverters continue to operate under current limiting mode after the fault is cleared to prevent inverter overloading. As seen in the simulation results, the inverter behaves distinctly different from the first case where the load on bus 76 is represented by traditional load model. To limit the inverter output current, the inverter terminal voltage stays lower than 80% of the nominal value. This undervoltage cannot be recovered unless the air conditioner load on bus 76 is tripped off.

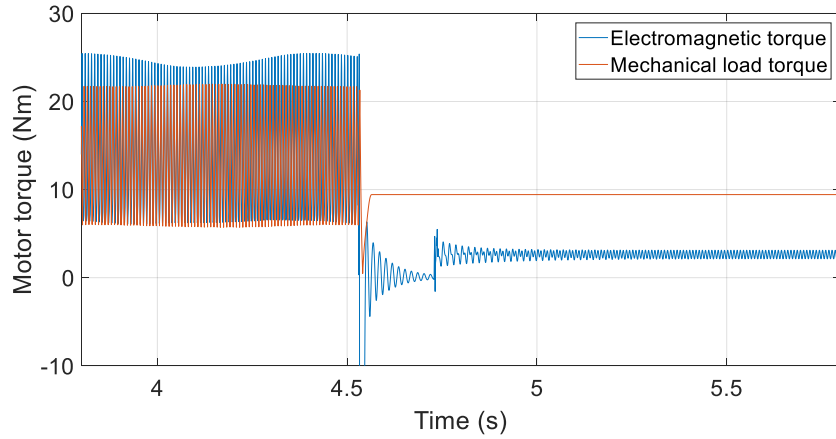


Figure 4.38 Electromagnetic torque and mechanical load torque under system fault

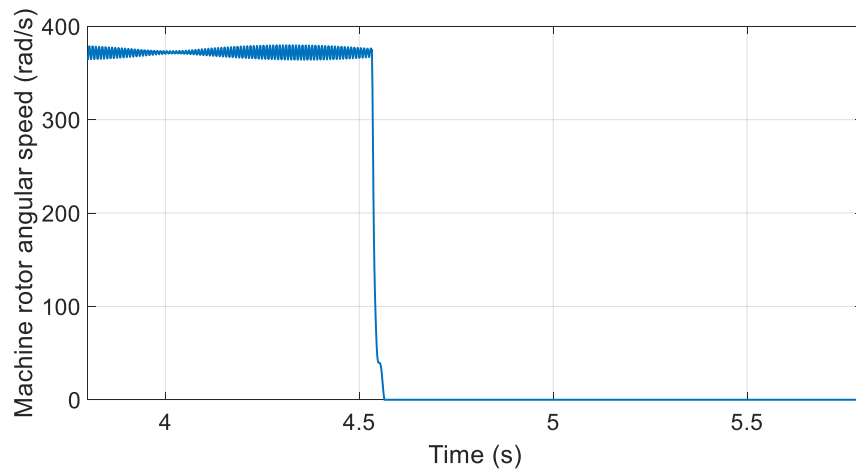


Figure 4.39 Air conditioner compressor motor rotor speed under system fault

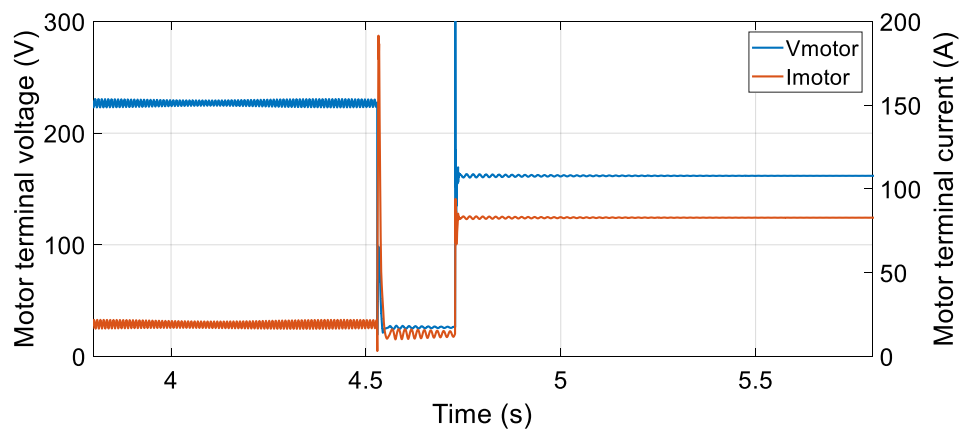


Figure 4.40 Air conditioner compressor motor terminal voltage and current under system fault

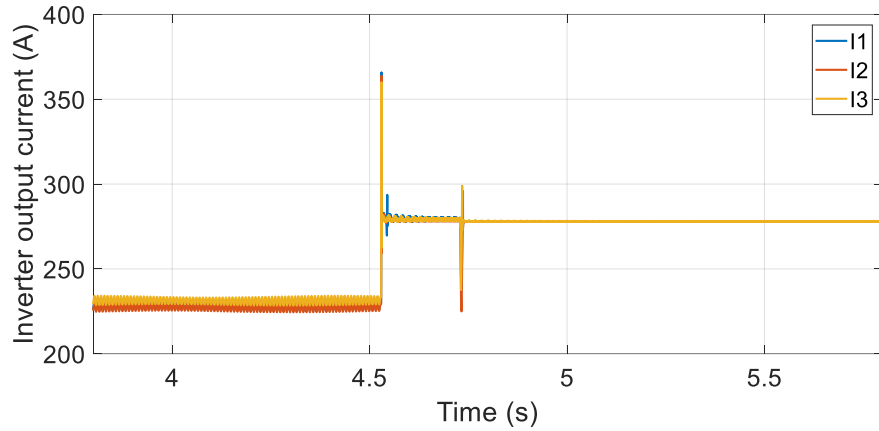


Figure 4.41 Inverter terminal current under system fault with air conditioner load

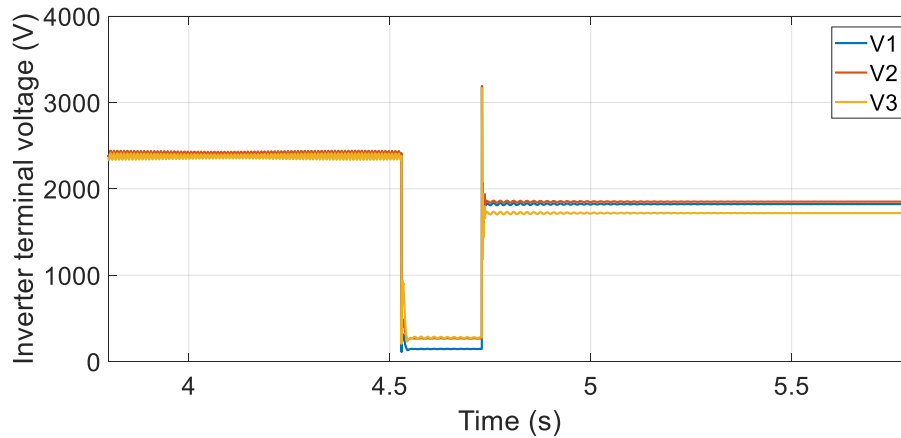


Figure 4.42 Inverter terminal voltage under system fault with air conditioner load

In this chapter, the converter based microgrid concept and implementation are demonstrated with IEEE 123 test feeder in a multi-platform real-time simulation testbed. The feeder and converter interfaced generators are simulated in Opal-RT by EMT-TS hybrid simulation method proposed in Chapter 3. A communication network based on Modbus protocol is developed for the communication between the converter local controllers being simulated in Opal-RT and a microgrid central controller running as an independent application software in a remote computer. EZDSP F28335 which can be used as the actual digital controller platform in converter hardware is included in the simulation loop by CHIL simulation to control the converter being simulated in Opal-RT. A

hierarchical converter based microgrid control scheme is proposed to enable the islanded microgrid operation with voltage/frequency regulation, dynamic power sharing and grid synchronization functions. The load side dynamic modeling is demonstrated with modeling the air conditioner compressor single-phase induction machine. The converter response during system fault is studied with the developed air conditioner load model. The simulation shows that the air conditioner loads can prevent converter from recovering to the normal operating mode after the fault is cleared while the static load model does not cause the same issue.

CHAPTER 5 Conclusions and future work

5.1 Conclusions

This thesis has covered the design, dynamic modeling and control of power converters for renewable interface and microgrids. In Chapter 2, a design of high efficiency high frequency grid-connected inverter is illustrated, with a simple soft-switching technique. The switching node current of the full-bridge inverter is manipulated at switching transitions to eliminate or reduce the turn-on loss of the main switches. The timing control of the auxiliary circuit is studied based on the detailed transient waveforms and the transition loss calculation. The circuit parameter and controller design of the proposed circuit is carried out for a 2.4 kW hardware prototype. The prototype circuit is assembled and tested in hardware experiments. The result shows approximately 2% efficiency improvement compared to the conventional full-bridge inverter at 400 kHz switching frequency by adopting the proposed soft-switching technique. The switching frequency is four times higher than most of the recent full-bridge inverters/PFCs at similar power level.

In Chapter 3, dynamic simulation of grid-connected converters in large-scale distribution systems is illustrated. Several phasor extraction methods in EMT-TS hybrid simulation are introduced and compared. The analysis shows that the dynamic phasor model based method has the advantage of better simulation numerical stability. Dynamic simulation of grid-connected converters in large scale distribution systems is implemented in an open source distribution analysis tool by using DLLs containing the converter dynamic model. DLLs corresponding to converter model with different control

configurations are developed based on the derived dynamic phasor models. Various simulation test cases including unbalanced fault, volt-VAr control and microgrid operation have been carried out. The simulations have shown the usefulness of the proposed method on studying converter dynamics in large distribution systems.

In Chapter 4, the EMT-TS hybrid simulation is extended to real-time simulation of a converter based microgrid. A hierarchical microgrid control scheme is proposed which enables the automated control of islanded microgrid with 100% penetration level of converter interfaced generations. A multi-platform real-time simulation testbed including Opal-RT, external digital controller board and a remote controller hosting computer is developed to simulate the microgrid, microgrid controllers and the communication network. The microgrid operation has been simulated for the IEEE 123 node test feeder with various test cases including voltage and frequency regulation, dynamic load sharing and grid synchronization. The load side dynamic modeling has also been carried out by modeling air conditioner compressor single-phase induction machines. The impact of the air conditioner loads on the voltage recovery after system fault has been simulated with the developed load model. The developed microgrid real-time simulation can be used as a testbed for system level controls of converter based microgrid, as well as converter response to other types of system contingency.

5.2 Future work

Possible topics for future work in the area of ZVS full-bridge inverter are listed below:

- Optimization of the filter inductor design considering size and efficiency, exploring other magnetic materials
- Shrinking the converter size by conducting a better thermal design
- Building a hardware prototype based on GaN device to further shrink the converter size and improve the efficiency
- Exploring solution for the voltage ringing across the auxiliary switches

Possible topics for future work in the area of large scale real-time simulation of converter based microgrids are listed below:

- Better representation of the network model in EMT system which reflects the high frequency interactions between the inverter, network and other inverters
- Complete the development of the remote microgrid central controller
- Power-hardware-in-loop (PHIL) simulation for including power stage circuit hardware in the simulation loop such as a commercial inverter
- Large scale real-time simulation of converter based microgrids

Possible topics for future work in the area of inverter controls for microgrid automation are listed below:

- Exploring systematic design method to determine the inverter output impedance and droop coefficients
- Robust controller design method considering uncertainty of the network parameter
- Involving system level controls under grid-connected operating mode

Reference

- [1] V. Calderaro, V. Galdi, F. Lamberti and A. Piccolo, "A Smart Strategy for Voltage Control Ancillary Service in Distribution Networks," *IEEE Transactions on Power Systems*, vol. 30, no. 1, pp. 494-502, Jan. 2015.
- [2] N. R. Ullah, K. Bhattacharya and T. Thiringer, "Wind Farms as Reactive Power Ancillary Service Providers—Technical and Economic Issues," *IEEE Transactions on Energy Conversion*, vol. 24, no. 3, pp. 661-672, Sept. 2009.
- [3] A. Cagnano, E. De Tuglie, M. Liserre and R. A. Mastromauro, "Online Optimal Reactive Power Control Strategy of PV Inverters," *IEEE Transactions on Industrial Electronics*, vol. 58, no. 10, pp. 4549-4558, Oct. 2011.
- [4] V. Calderaro, G. Conio, V. Galdi, G. Massa and A. Piccolo, "Optimal Decentralized Voltage Control for Distribution Systems with Inverter-Based Distributed Generators," *IEEE Transactions on Power Systems*, vol. 29, no. 1, pp. 230-241, Jan. 2014.
- [5] H. Sugihara, K. Yokoyama, O. Saeki, K. Tsuji and T. Funaki, "Economic and Efficient Voltage Management Using Customer-Owned Energy Storage Systems in a Distribution Network with High Penetration of Photovoltaic Systems," *IEEE Transactions on Power Systems*, vol. 28, no. 1, pp. 102-111, Feb. 2013.
- [6] M. Nick, R. Cherkaoui and M. Paolone, "Optimal Allocation of Dispersed Energy Storage Systems in Active Distribution Networks for Energy Balance and Grid Support," *IEEE Transactions on Power Systems*, vol. 29, no. 5, pp. 2300-2310, Sept. 2014.
- [7] Pengfei Wang, D. H. Liang, Jialiang Yi, P. F. Lyons, P. J. Davison and P. C. Taylor, "Integrating Electrical Energy Storage into Coordinated Voltage Control Schemes for Distribution Networks," *IEEE Transactions on Smart Grid*, vol. 5, no. 2, pp. 1018-1032, March 2014.
- [8] H. Zhou, T. Bhattacharya, D. Tran, T. Siew and A. Khambadkone, "Composite Energy Storage System Involving Battery and Ultracapacitor With Dynamic Energy Management in Microgrid Applications", *IEEE Transactions on Power Electronics*, vol. 26, no. 3, pp. 923-930, 2011.
- [9] J. Carrasco, L. Franquelo, J. Bialasiewicz, E. Galvan, R. PortilloGuisado, M. Prats, J. Leon and N. Moreno-Alfonso, "Power-Electronic Systems for the Grid Integration of Renewable Energy Sources: A Survey", *IEEE Transactions on Industrial Electronics*, vol. 53, no. 4, pp. 1002-1016, 2006.

- [10] J. Millan, P. Godignon, X. Perpina, A. Perez-Tomas and J. Rebollo, "A Survey of Wide Bandgap Power Semiconductor Devices", *IEEE Transactions on Power Electronics*, vol. 29, no. 5, pp. 2155-2163, 2014.
- [11] F. Katiraei and M. Iravani, "Power Management Strategies for a Microgrid With Multiple Distributed Generation Units", *IEEE Transactions on Power Systems*, vol. 21, no. 4, pp. 1821-1831, 2006.
- [12] M. Delghavi and A. Yazdani, "An Adaptive Feedforward Compensation for Stability Enhancement in Droop-Controlled Inverter-Based Microgrids", *IEEE Transactions on Power Delivery*, vol. 26, no. 3, pp. 1764-1773, 2011.
- [13] J. Guerrero, J. Vasquez, J. Matas, M. Castilla and L. de Vicuna, "Control Strategy for Flexible Microgrid Based on Parallel Line-Interactive UPS Systems", *IEEE Transactions on Industrial Electronics*, vol. 56, no. 3, pp. 726-736, 2009.
- [14] S. Ashabani and Y. Mohamed, "General Interface for Power Management of Micro-Grids Using Nonlinear Cooperative Droop Control", *IEEE Transactions on Power Systems*, vol. 28, no. 3, pp. 2929-2941, 2013.
- [15] Yun Wei Li and Ching-Nan Kao, "An Accurate Power Control Strategy for Power-Electronics-Interfaced Distributed Generation Units Operating in a Low-Voltage Multibus Microgrid", *IEEE Transactions on Power Electronics*, vol. 24, no. 12, pp. 2977-2988, 2009.
- [16] P. Piagi and R. H. Lasseter, "Autonomous control of microgrids," *IEEE Power Engineering Society General Meeting*, pp. 8, 2006.
- [17] N. Pogaku, M. Prodanovic and T. C. Green, "Modeling, analysis and testing of autonomous operation of an inverter-based microgrid," *IEEE Transactions on Power Electronics*, vol. 22, no. 2, pp. 613-625, March 2007.
- [18] R. Teodorescu, M. Liserre and P. Rodríguez Cortés, *Grid converters for photovoltaic and wind power systems*. Chichester, West Sussex: Wiley, 2011.
- [19] L. Cong and H. Lee, "High-voltage high-frequency non-isolated multiphase DC-DC converters with passive-saving two-phase QSW-ZVS technique," *Journal of Analog Integrated Circuits and Signal Processing*, vol. 88, no. 2, pp. 303 – 317, Aug. 2016.
- [20] L. Cong and H. Lee, "A 110 – 250V 2MHz isolated DC-DC converter with integrated high-speed synchronous gate drive," in *Proc. IEEE Energy Conversion Congress and Exposition*, Montreal, Canada, Sep. 2015, pp. 1479 - 1484.

- [21] Y. Xia and R. Ayyanar, "Optimal variable switching frequency scheme to reduce combined switching loss and inductor core loss of single phase grid-connected inverter," *2015 IEEE Energy Conversion Congress and Exposition (ECCE)*, Montreal, QC, 2015, pp. 1534-1540.
- [22] Q. Zhang, H. Hu, D. Zhang, X. Fang, J. Shen, and I. Bartarseh, "A controlled-type ZVS technique without auxiliary components for the low power DC/AC inverter," *IEEE Trans. Power Electron.*, vol. 28, no. 7, pp. 3287–3296, Jul. 2013.
- [23] A. Amirahmadi, H. Hu, A. Grishina, Q. Zhang, L. Chen, U. Somani, and I. Batarseh, "Hybrid ZVS BCM current controlled three-phase microinverter," *IEEE Trans. Power Electron.*, vol. 29, no. 4, pp. 2124–2134, Apr. 2014.
- [24] W. McMurray, "Resonant snubbers with auxiliary switches," *IEEE Trans. Ind. Appl.*, vol. 29, no. 2, pp. 355–362, Apr. 1993.
- [25] R. W. De Doncker and J. P. Lyons, "The auxiliary resonant commutated pole converter," in *Proc. IEEE Int. Conf. Ind. Appl. Soc.*, 1990, pp. 1228– 1235.
- [26] J. Lai, S. R. W. Young, J. G. W. Ott, J. W. McKeever, and Z. Fang, "A delta-configured auxiliary resonant snubber inverter," *IEEE Trans. Ind. Appl.*, vol. 32, no. 3, pp. 518–525, Jun. 1996.
- [27] J. Lai, "Practical design methodology of auxiliary resonant snubber inverters," in *Proc. 27th Annu. IEEE Power Electron. Spec. Conf.*, Baveno, Italy, Jun. 1996, pp. 432–437.
- [28] H. Yamamoto, M. Kaneda, and M. Nakaoka, "Three-phase soft-switching inverter resonant with unique resonant snubbers," in *Proc. IEEE Int. Conf. Power Electron. Drive Syst.*, 1999, pp. 1078–1083.
- [29] J. Lai, J. Zhang, H. Yu, and H. Kouns, "Source and load adaptive design for a high-power soft-switching inverter," *IEEE Trans. Power Electron.*, vol. 21, no. 6, pp. 1667–1675, Nov. 2006.
- [30] J. L. Russi, M. L. D. S. Martins, and H. L. Hey, "Coupled-filter-inductor soft-switching techniques: Principles and topologies," *IEEE Trans. Ind. Electron.*, vol. 55, no. 9, pp. 3361–3373, Sep. 2008.
- [31] D. M. Divan, "The resonant DC link converter-a new concept in static power conversion," *IEEE Trans. Ind. Appl.*, vol. 25, no. 2, pp. 317–325, Apr. 1989.

- [32] R. W. De Doncker and J. P. Lyons, "The auxiliary quasi-resonant DC link inverter," in Proc. 22th Annu. IEEE Power Electron. Spec. Conf., Cambridge, U.K., 1991, pp. 248–253.
- [33] C.-M. Wang, C.-H. Su, M.-C. Jiang, and Y.-C. Lin, "A ZVS-PWM single phase inverter using a simple ZVS-PWM commutation cell," *IEEE Trans. Ind. Electron.*, vol. 55, no. 2, pp. 758–766, Feb. 2008.
- [34] H. Chung, S. Hui and K. Tse, "Reduction of EMI emission from power converter using soft-switching techniques", *Electronics Letters*, vol. 32, no. 11, p. 977, 1996.
- [35] J. Shao, R. L. Lin, F. C. Lee, and D. Y. Chen, "Characterization of EMI performance for hard and soft-switched inverters," in Applied Power Electronics Conference and Exposition, 2000. APEC 2000. Fifteenth Annual IEEE, 2000, pp. 1009-1014.
- [36] M. Liserre, F. Blaabjerg and S. Hansen, "Design and Control of an LCL-Filter-Based Three-Phase Active Rectifier", *IEEE Transactions on Industry Applications*, vol. 41, no. 5, pp. 1281-1291, 2005.
- [37] S. Parker, B. McGrath and D. Holmes, "Regions of Active Damping Control for LCL Filters", *IEEE Transactions on Industry Applications*, vol. 50, no. 1, pp. 424-432, 2014.
- [38] Texas Instruments, "High-Efficiency, 1.6-kW High-Density GaN-Based 1-MHz CrM Totem-Pole PFC Converter Reference Design" TIDUDT3-January 2018, Available: <http://www.ti.com/tool/TIDA-00961>.
- [39] Texas Instruments, "98.5% Efficiency, 6.6-kW Totem-Pole PFC Reference Design for HEV/EV Onboard Charger" TIDUE54-March 2018, Available: <http://www.ti.com/tool/TIDA-01604>.
- [40] H. F. Xiao, L. Zhang and Y. Li, "A Zero-Voltage-Transition HERIC-Type Transformerless Photovoltaic Grid-Connected Inverter," in *IEEE Transactions on Industrial Electronics*, vol. 64, no. 2, pp. 1222-1232, Feb. 2017.
- [41] Y. Chen *et al.*, "A ZVS Grid-Connected Full-Bridge Inverter With a Novel ZVS SPWM Scheme," in *IEEE Transactions on Power Electronics*, vol. 31, no. 5, pp. 3626-3638, May 2016.
- [42] PLECS, electrical engineering software, [Online]. Available: <http://www.plexim.com/>
- [43] Manitoba HVDC Research Centre, PSCAD Software, 2014 [Online]. Available: <https://hvdc.ca/pscad>

- [44] OpenDSS, Distribution System Simulator, [Online]. Available: <https://sourceforge.net/projects/electricdss/>
- [45] P.Kunder, *Power System Stability and Control*. New York: McGraw-Hill, 1994.
- [46] A. Nagarajan and R. Ayyanar, "Dynamic analysis of distribution systems with high penetration of PV generators using differential algebraic equations in OpenDSS," *North American Power Symposium (NAPS), 2014*, Pullman, WA, 2014, pp. 1-6.
- [47] T. E. McDermott, "Modeling PV for unbalanced, dynamic and quasistatic distribution system analysis," *Power and Energy Society General Meeting, IEEE*, San Diego, CA, 2011, pp. 1-3.
- [48] B. Kasztenny and M. Kezunovic, "A method of linking different modeling techniques for accurate and efficient simulation," *IEEE Transactions on Power Systems*, vol. 15, no. 1, pp. 65-72, Feb. 2000.
- [49] Arjen A. van der Meer, Madeleine Gibescu, Mart A. M. M. van der Meijden, Wil L. Kling, Jan A. Ferreira, "Advanced Hybrid Transient Stability and EMT Simulation for VSC-HVDC Systems," *IEEE Transactions on Power Delivery*, vol. 30, no. 3, pp. 1057-1066, June 2015.
- [50] F. Plumier, P. Aristidou, C. Geuzaine and T. Van Cutsem, "Co-Simulation of Electromagnetic Transients and Phasor Models: A Relaxation Approach," *IEEE Transactions on Power Delivery*, vol. 31, no. 5, pp. 2360-2369, Oct. 2016.
- [51] G. W. Anderson, N.R. Waston, C. P. Arnold, and J. Arrillaga, "A new hybrid algorithm for analysis of HVDC and FACTS systems," *Proceedings of the International Conference on Energy Management and Power Delivery*, vol. 2, pp. 462-467, 1995.
- [52] H. Su, K. W. Chan, L. A. Snider, and J. C. Soumagne, "Advancement on the integration of electromagnetic transients simulator and transient stability simulator," *International Conference on Power Systems Transients*, no. IPST05-238, pp. 1-6, Montreal, QC, Canada, June 2005.
- [53] Yi Zhang, Aniruddha M. Gole, Wenchuan Wu, Boming Zhang, and Hongbin Sun, "Development and Analysis of Applicability of a Hybrid Transient Simulation Platform Combining TSA and EMT Elements," *IEEE Transactions on Power Systems*, vol. 28, no. 1, Feb. 2013.
- [54] Xi Lin, A. M. Gole, and Ming Yu, "A wide-Band Multi-Port System Equivalent for Real-Time Digital Power System Simulator," *IEEE Transactions on Power Systems*, vol. 24, no. 1, Feb. 2009.

- [55] S. Mishra, D. Ramasubramanian, and P. Sekhar, "A seamless control methodology for a grid-connected and isolated pv-diesel microgrid," *IEEE Transactions on Power Systems.*, vol. 28, no. 4, pp. 4393–4404, Nov 2013.
- [56] R. de Almeida and J. Péc,as Lopes, "Participation of doubly fed induction wind generators in system frequency regulation," *IEEE Transactions on Power Systems*, vol. 22, no. 3, pp. 944–950, Aug 2007.
- [57] J. F. Conroy and R. Watson, "Frequency response capability of full converter wind turbine generators in comparison to conventional generation," *IEEE Transactions on Power Systems*, vol. 23, no. 2, pp. 649–656, May 2008.
- [58] K. Clark, R. Walling, N. Miller, "Solar photovoltaic (pv) plant models in pslf," 2011 IEEE Power and Energy Society General Meeting, pp. 1-5, July 2011.
- [59] N. W. Miller, J. J. Sanchez-Gasca, W. W. Price, R. W. Delmerico, "Dynamic modeling of GE 1.5 and 3.6 MW wind turbine-generators for stability simulations," 2003 IEEE Power and Energy Society General Meeting, vol. 3, pp. 1977-1983, July 2003.
- [60] S. Cole, B. Haut, "Robust Modeling Against Model-Solver Interactions for High-Fidelity Simulation of VSC HVDC Systems in EUROSTAG," *IEEE Transactions on Power Systems*, vol. 28, pp. 2632-2638, Dec. 2012.
- [61] M. A. Elizondo, F. K. Tuffner and K. P. Schneider, "Three-Phase Unbalanced Transient Dynamics and Power-flow for Modeling Distribution Systems with Synchronous Machines," *IEEE Transactions on Power Systems*, vol. 31, no. 1, pp. 105-115, Jan. 2016.
- [62] CYME by Cooper power systems, [Online]. Available: <http://www.cyme.com/software/cymdist/>, 2013.
- [63] GridLab-D, power distribution system simulation and analysis tool, [Online]. Available: <http://www.gridlabd.org/>
- [64] J. W. Smith, R. Dugan, M. Rylander and T. Key, "Advanced distribution planning tools for high penetration PV deployment," 2012 IEEE Power and Energy Society General Meeting, San Diego, CA, 2012, pp. 1-7.
- [65] R. C. Dugan and T. E. McDermott, "An open source platform for collaborating on smart grid research," Power and Energy Society General Meeting, 2011 IEEE, San Diego, CA, 2011, pp. 1-7.

- [66] Hua Ye and Kai Strunz, "Multi-scale and Frequency-dependent Modeling of Electric Power Transmission Lines," *IEEE Transactions on Power Delivery*, vol. PP, no. 99, pp. 1-1, March 2017.
- [67] Kai Strunz, Rachel Shintaku, and Feng Gao, "Frequency-Adaptive Network Modeling for Integrative Simulation of Natural and Envelope Waveforms in Power Systems and Circuits," *IEEE Transactions on Circuit and Systems I: Regular Papers*, vol. 53, no. 12, pp. 2788-2803, Dec. 2006.
- [68] Feng Gao and Kai Strunz, "Frequency-Adaptive Power System Modeling for Multiscale Simulation of Transients," *IEEE Transactions on Power Systems*, vol. 24, no. 2, pp. 561-571, April 2009.
- [69] Zhixin Miao, Lakshan Piyasinghe, Javad Khazaei, and Lingling Fan, "Dynamic Phasor-Based Modeling of Unbalanced Radial Distribution Systems," *IEEE Transactions on Power Systems*, vol. 30, no. 6, Nov. 2015.
- [70] A. M. Stankovic, B.C. Lesieutre, and T. Aydin, "Modeling and Analysis of Single-Phase Induction Machines with Dynamic Phasors," *IEEE Transactions on Power Systems*, vol. 14, no. 1, Feb. 1999.
- [71] Aleksandar M. Stankovic and Timur Aydin, "Analysis of Asymmetrical Faults in Power Systems Using Dynamic Phasors," *IEEE Transactions on Power Systems*, vol. 15, no. 3, Aug. 2000.
- [72] Remus Teodorescu, Marco Liserre, and Pedro Rodriguez, *Grid Converters for Photovoltaic and Wind Power Systems*, Hoboken, New Jersey: John Wiley & Sons, 2011.
- [73] Y. Tang, X. Mao and R. Ayyanar, "Distribution system modeling using CYMDIST for study of high penetration of distributed solar photovoltaics," North American Power Symposium (NAPS), 2012, Champaign, IL, 2012, pp. 1-6.
- [74] J. W. Smith, W. Sunderman, R. Dugan and B. Seal, "Smart inverter volt/var control functions for high penetration of PV on distribution systems," Power Systems Conference and Exposition (PSCE), 2011 IEEE/PES, Phoenix, AZ, 2011, pp. 1-6.
- [75] D. Dong, B. Wen, D. Boroyevich, P. Mattavelli, and Y. Xue, "Analysis of Phase-Locked Loop Low-Frequency Stability in Three-Phase Grid-Connected Power Converters Considering Impedance Interactions," *IEEE Transactions on Industrial Electronics*, vol. 62, no. 1, pp. 310-321, January 2015.
- [76] X. Wang and W. Freitas, "Impact of positive-feedback anti-islanding methods on small-signal stability of inverter-based distributed generation," *IEEE Transactions on Energy Conversion*, vol. 23, no. 3, pp. 923-931, July 2008.

- [77] Xuegong Wang, P. Wilson, and D. Woodford, "Interfacing transient stability program to EMTDC program," Proceedings. International Conference on Power System Technology, vol. 2, pp. 1264-1269, 2002.
- [78] M. D. Omar Faruque et al., "Real-Time Simulation Technologies for Power Systems Design, Testing, and Analysis," in *IEEE Power and Energy Technology Systems Journal*, vol. 2, no. 2, pp. 63-73, June 2015.
- [79] R. Kuffel, J. Giesbrecht, T. Maguire, R. P. Wierckx, and P. McLaren, "RTDS—A fully digital power system simulator operating in real time," in Proc. ICDS, College Station, TX, Apr. 1995, pp. 19–24
- [80] L. Pak, M. Faruque, X. Nie and V. Dinavahi, "A Versatile Cluster-Based Real-Time Digital Simulator for Power Engineering Research", *IEEE Transactions on Power Systems*, vol. 21, no. 2, pp. 455-465, 2006.
- [81] dSPACE GmbH, Paderborn, Germany. (2014). dSPACE Product Manual. [Online]. Available: <http://www.dspace.com>
- [82] A. Myaing and V. Dinavahi, "FPGA-Based Real-Time Emulation of Power Electronic Systems With Detailed Representation of Device Characteristics", *IEEE Transactions on Industrial Electronics*, vol. 58, no. 1, pp. 358-368, 2011.
- [83] M. Matar and R. Iravani, "FPGA Implementation of the Power Electronic Converter Model for Real-Time Simulation of Electromagnetic Transients", *IEEE Transactions on Power Delivery*, vol. 25, no. 2, pp. 852-860, 2010.
- [84] G. Parma and V. Dinavahi, "Real-Time Digital Hardware Simulation of Power Electronics and Drives", *IEEE Transactions on Power Delivery*, vol. 22, no. 2, pp. 1235-1246, 2007.
- [85] A. Monti, E. Santi, R. Dougal and M. Riva, "Rapid prototyping of digital controls for power electronics", *IEEE Transactions on Power Electronics*, vol. 18, no. 3, pp. 915-923, 2003.
- [86] B. Lu, X. Wu, H. Figueroa and A. Monti, "A Low-Cost Real-Time Hardware-in-the-Loop Testing Approach of Power Electronics Controls", *IEEE Transactions on Industrial Electronics*, vol. 54, no. 2, pp. 919-931, 2007.
- [87] A. Bouscayrol, "Different types of hardware-in-the-loop simulation for electric drives," in Proc. IEEE ISIE, Cambridge, U.K., Jun. 2008, pp. 2146–2151.

- [88] Wei Li, G. Joos and J. Belanger, "Real-Time Simulation of a Wind Turbine Generator Coupled With a Battery Supercapacitor Energy Storage System", *IEEE Transactions on Industrial Electronics*, vol. 57, no. 4, pp. 1137-1145, 2010.
- [89] W. Qiao, G. Venayagamoorthy and R. Harley, "Real-Time Implementation of a STATCOM on a Wind Farm Equipped With Doubly Fed Induction Generators", *IEEE Transactions on Industry Applications*, vol. 45, no. 1, pp. 98-107, 2009.
- [90] H. Kojabadi, L. Chang and T. Boutot, "Development of a Novel Wind Turbine Simulator for Wind Energy Conversion Systems Using an Inverter-Controlled Induction Motor", *IEEE Transactions on Energy Conversion*, vol. 19, no. 3, pp. 547-552, 2004.
- [91] H. Li, M. Steurer, K. Shi, S. Woodruff and D. Zhang, "Development of a Unified Design, Test, and Research Platform for Wind Energy Systems Based on Hardware-in-the-Loop Real-Time Simulation", *IEEE Transactions on Industrial Electronics*, vol. 53, no. 4, pp. 1144-1151, 2006.
- [92] R. J. Yinger, S. S. Venkata, and V. A. Centeno, "Fault locating, prediction and protection (FLPPS)," submitted by Southern California Edison to the U.S. Department of Energy, Contract No. DE-FC02-06CH11352, Final Rep., Sep. 30, 2010.
- [93] R. Yinger, S. Venkata and V. Centeno, "Southern California Edison's Advanced Distribution Protection Demonstrations", *IEEE Transactions on Smart Grid*, vol. 3, no. 2, pp. 1012-1019, 2012.
- [94] D. Jakominich, R. Krebs, D. Retzmann and A. Kumar, "Real time digital power system simulator design considerations and relay performance evaluation", *IEEE Transactions on Power Delivery*, vol. 14, no. 3, pp. 773-781, 1999.
- [95] M. Kezunovic, J. Domaszewicz, V. Skendzic, M. Aganagic, J. Bladow, S. McKenna and D. Hamai, "Design, implementation and validation of a real-time digital simulator for protection relay testing", *IEEE Transactions on Power Delivery*, vol. 11, no. 1, pp. 158-164, 1996.
- [96] Y. Li, D. Vilathgamuwa and P. Loh, "Design, Analysis, and Real-Time Testing of a Controller for Multibus Microgrid System", *IEEE Transactions on Power Electronics*, vol. 19, no. 5, pp. 1195-1204, 2004.
- [97] M. Park and I. Yu, "A Novel Real-Time Simulation Technique of Photovoltaic Generation Systems Using RTDS", *IEEE Transactions on Energy Conversion*, vol. 19, no. 1, pp. 164-169, 2004.

- [98] T. Logenthiran, D. Srinivasan, A. Khambadkone and H. Aung, "Multiagent System for Real-Time Operation of a Microgrid in Real-Time Digital Simulator", *IEEE Transactions on Smart Grid*, vol. 3, no. 2, pp. 925-933, 2012.
- [99] Jin-Hong Jeon, Jong-Yul Kim, Hak-Man Kim, Seul-Ki Kim, Changhee Cho, Jang-Mok Kim, Jong-Bo Ahn and Kee-Young Nam, "Development of Hardware In-the-Loop Simulation System for Testing Operation and Control Functions of Microgrid", *IEEE Transactions on Power Electronics*, vol. 25, no. 12, pp. 2919-2929, 2010.
- [100] A. Jain, "Synchronized Real-Time Simulation of Distributed Networked Controls for a Power System Case Study", Ph.D, Colorado State University, 2013.
- [101] J. Liu, Y. Miura and T. Ise, "Comparison of Dynamic Characteristics Between Virtual Synchronous Generator and Droop Control in Inverter-Based Distributed Generators", *IEEE Transactions on Power Electronics*, vol. 31, no. 5, pp. 3600-3611, 2016.
- [102] "EIS: Energy Information Systems", *Eis.asu.edu*, 2018. [Online]. Available: <https://eis.asu.edu/flex/index.html>.
- [103] "The Modbus Organization", *Modbus.org*, 2018. [Online]. Available: <http://www.modbus.org/>.
- [104] J. Guerrero, J. Vasquez, J. Matas, M. Castilla and L. de Vicuna, "Control Strategy for Flexible Microgrid Based on Parallel Line-Interactive UPS Systems", *IEEE Transactions on Industrial Electronics*, vol. 56, no. 3, pp. 726-736, 2009.
- [105] J. Guerrero, J. Vasquez, J. Matas, L. de Vicuna and M. Castilla, "Hierarchical Control of Droop-Controlled AC and DC Microgrids—A General Approach Toward Standardization", *IEEE Transactions on Industrial Electronics*, vol. 58, no. 1, pp. 158-172, 2011.
- [106] E. Coelho, P. Cortizo and P. Garcia, "Small-signal stability for parallel-connected inverters in stand-alone AC supply systems", *IEEE Transactions on Industry Applications*, vol. 38, no. 2, pp. 533-542, 2002.
- [107] P. Kundur, N. Balu and M. Lauby, *Power system stability and control*. New York: McGraw-Hill, 2009.
- [108] J. Guerrero, L. GarciadeVicuna, J. Matas, M. Castilla and J. Miret, "Output Impedance Design of Parallel-Connected UPS Inverters With Wireless Load-Sharing Control", *IEEE Transactions on Industrial Electronics*, vol. 52, no. 4, pp. 1126-1135, 2005

- [109] Y. Liu, V. Vittal, J. Undrill and J. Eto, "Transient Model of Air-Conditioner Compressor Single Phase Induction Motor", *IEEE Transactions on Power Systems*, vol. 28, no. 4, pp. 4528-4536, 2013.
- [110] B. Williams, W. Schmus and D. Dawson, "Transmission voltage recovery delayed by stalled air conditioner compressors", *IEEE Transactions on Power Systems*, vol. 7, no. 3, pp. 1173-1181, 1992.
- [111] D. Vilathgamuwa, P. Loh and Y. Li, "Protection of Microgrids During Utility Voltage Sags", *IEEE Transactions on Industrial Electronics*, vol. 53, no. 5, pp. 1427-1436, 2006.
- [112] Y. Li, D. Vilathgamuwa, P. Loh and F. Blaabjerg, "A Dual-Functional Medium Voltage Level DVR to Limit Downstream Fault Currents", *IEEE Transactions on Power Electronics*, vol. 22, no. 4, pp. 1330-1340, 2007.
- [113] X. Lu, J. Wang, J. Guerrero and D. Zhao, "Virtual-Impedance-Based Fault Current Limiters for Inverter Dominated AC Microgrids", *IEEE Transactions on Smart Grid*, vol. 9, no. 3, pp. 1599-1612, 2018.

APPENDIX A

ANALYSIS OF THE TURN-ON TRANSITION WHEN $v_g > 0.5V_{dc}$

Case a

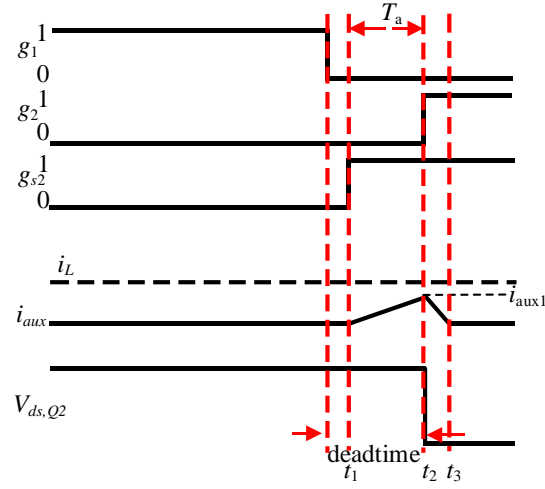


Figure A1 Case a of the Q_2 turn-on transition when $v_g > 0.5V_{dc}$

[$t_1 \sim t_2$]:

$$v_{ds,Q2} = V_{dc} \quad (\text{A.1})$$

$$i_{aux} = \frac{V_{dc} - v_g}{L_{aux}}(t - t_1) \quad (\text{A.2})$$

$$i_{aux1} = \frac{V_{dc} - v_g}{L_{aux}}T_a \quad (\text{A.3})$$

$$E_1 = I_{rms1}^2 R_{aux} T_a = \frac{i_{aux1}^3 L_{aux} R_{aux}}{3(V_{dc} - v_g)} \quad (\text{A.4})$$

$$E_{D1} = \frac{1}{2} V_F i_{aux1} T_a \quad (\text{A.5})$$

[$t_2 \sim t_3$]:

$$v_{ds,Q2} = 0 \quad (\text{A.6})$$

$$i_{aux} = \frac{-v_g}{L_{aux}}(t - t_2) \quad (\text{A.7})$$

$$E_2 = I_{rms2}^2 R_{aux} (t_3 - t_2) = \frac{i_{aux1}^3 L_{aux} R_{aux}}{3v_g} \quad (A.8)$$

$$E_{D2} = \frac{1}{2} V_F i_{aux1} (t_3 - t_2) = \frac{1}{2} V_F i_{aux1} \frac{L_{aux} i_{aux1}}{v_g} \quad (A.9)$$

$$E_{aux} = E_1 + E_2 + E_{D1} + E_{D2} \quad (A.10)$$

$$E_{on,Q2} = E_{on}(i_{aux1}, V_{ds1}) \quad (A.11)$$

Case b

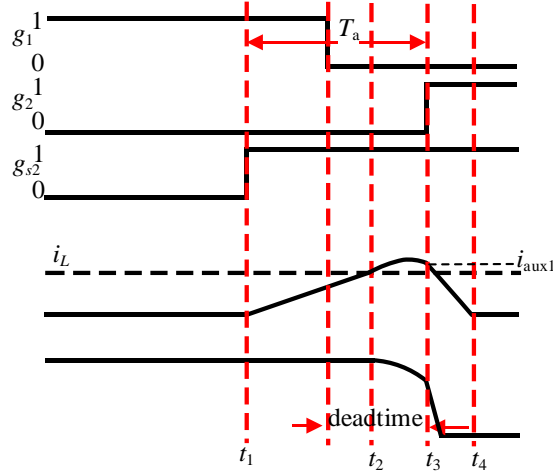


Figure A2 Case *b* of the Q_2 turn-on transition when $v_g > 0.5V_{dc}$

[$t_1 \sim t_2$]:

$$v_{ds,Q2} = V_{dc} \quad (A.12)$$

$$i_{aux} = \frac{V_{dc} - v_g}{L_{aux}} (t - t_1) \quad (A.13)$$

$$t_2 - t_1 = \frac{i_L L_{aux}}{V_{dc} - v_g} \quad (A.14)$$

$$I_{rms1} = \frac{i_L}{\sqrt{3}} \quad (A.15)$$

$$E_1 = I_{rms1}^2 R_{aux}(t_2 - t_1) = \frac{i_L^3 L_{aux} R_{aux}}{3(V_{dc} - v_g)} \quad (A.16)$$

$$E_{D1} = \frac{1}{2} V_F I_L (t_2 - t_1) = \frac{i_L^2 V_F L_{aux}}{2(V_{dc} - v_g)} \quad (A.17)$$

[t2~t3]:

$$v_{ds,Q2} = v_g + (V_{dc} - v_g) \cos(\omega_r(t - t_2)) \quad (A.18)$$

$$V_{ds1} = v_g + (V_{dc} - v_g) \cos(\omega_r(t_3 - t_2)) \quad (A.19)$$

$$i_{aux} = i_L + \frac{V_{dc} - v_g}{L_{aux} \omega_r} \sin(\omega_r(t - t_2)) \quad (A.20)$$

$$I_{aux1} = i_L + \frac{V_{dc} - v_g}{L_{aux} \omega_r} \sin(\omega_r(t_3 - t_2)) \quad (A.21)$$

$$t_3 - t_2 = T_a - \frac{i_L L_{aux}}{V_{dc} - v_g} \quad (A.22)$$

$$I_{rms2} = \sqrt{\frac{1}{t_3 - t_2} \int_{t_2}^{t_3} i_{aux}^2 dt} \quad (A.23)$$

$$E_2 = I_{rms2}^2 R_{aux}(t_3 - t_2) \quad (A.24)$$

$$E_{D2} = V_F \int_{t_2}^{t_3} i_{aux} dt = V_F \left(i_L(t_3 - t_2) - \frac{V_{dc} - v_g}{L_{aux} \omega_r^2} \cos(\omega_r(t_3 - t_2)) + \frac{V_{dc} - v_g}{L_{aux} \omega_r^2} \right) \quad (A.25)$$

[t3~t4]:

$$v_{ds,Q2} = 0 \quad (A.26)$$

$$i_{aux} = i_{aux1} - \frac{v_g}{L_{aux}}(t - t_3) \quad (A.27)$$

$$I_{rms3} = \frac{I_{aux1}}{\sqrt{3}} \quad (A.28)$$

$$E_3 = I_{rms3}^2 R_{aux} (t_4 - t_3) = \frac{i_{aux1}^3 L_{aux} R_{aux}}{3v_g} \quad (A.29)$$

$$E_{D3} = \frac{V_F i_{aux1}}{2} (t_4 - t_3) = \frac{V_F i_{aux1}^2 L_{aux}}{2v_g} \quad (A.30)$$

$$E_{aux} = E_1 + E_2 + E_3 + E_{D1} + E_{D2} + E_{D3} \quad (A.31)$$

$$E_{on,Q2} = E_{on}(0, V_{ds1})$$

Case c

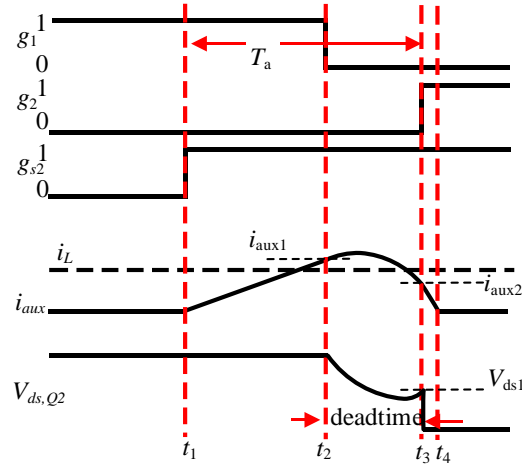


Figure A3 Case c of the Q_2 turn-on transition when $v_g > 0.5V_{dc}$

[$t_1 \sim t_2$]:

$$v_{ds,Q2} = V_{dc} \quad (A.32)$$

$$i_{aux} = \frac{V_{dc} - v_g}{L_{aux}} (t - t_1) \quad (A.33)$$

$$t_2 - t_1 = T_a - \frac{\pi}{\omega_r} \quad (A.34)$$

$$i_{aux1} = \frac{V_{dc} - v_g}{L_{aux}} (t_2 - t_1) \quad (A.35)$$

$$\Delta i = i_{aux1} - i_L \quad (\text{A.36})$$

$$E_1 = I_{rms1}^2 R_{aux}(t_2 - t_1) = \frac{i_{aux1}^3 L_{aux} R_{aux}}{3(V_{dc} - v_g)} \quad (\text{A.37})$$

$$E_{D1} = \frac{1}{2} V_F i_{aux1}(t_2 - t_1) \quad (\text{A.38})$$

[t2~t3]:

$$v_{ds,Q2} = v_g + (V_{dc} - v_g) \cos(\omega_r(t - t_2)) - \sqrt{\frac{L_{aux}}{2C_2}} \Delta i \sin(\omega_r(t - t_2)) \quad (\text{A.39})$$

$$V_{ds1} = 2v_g - V_{dc} \quad (\text{A.40})$$

$$i_{aux} = i_L + \frac{V_{dc} - v_g}{L_{aux} \omega_r} \sin(\omega_r(t - t_2)) + \Delta i \cos(\omega_r(t - t_2)) \quad (\text{A.41})$$

$$i_{aux2} = i_L - \Delta i \quad (\text{A.42})$$

$$t_3 - t_2 = \frac{\pi}{\omega_r} \quad (\text{A.43})$$

$$I_{rms2} = \sqrt{\frac{1}{t_3 - t_2} \int_{t_2}^{t_3} i_{aux}^2 dt} \quad (\text{A.44})$$

$$E_2 = I_{rms2}^2 R_{aux}(t_3 - t_2) \quad (\text{A.45})$$

$$E_{D2} = V_F \int_{t_2}^{t_3} i_{aux} dt \quad (\text{A.46})$$

[t3~t4]:

$$v_{ds,Q2} = 0 \quad (\text{A.47})$$

$$i_{aux} = i_{aux2} - \frac{v_g}{L_{aux}}(t - t_3) \quad (\text{A.48})$$

$$E_3 = I_{rms3}^2 R_{aux} (t_4 - t_3) = \frac{i_{aux2}^3 L_{aux} R_{aux}}{3v_g} \quad (A.49)$$

$$E_{D3} = \frac{V_F i_{aux2}}{2} (t_4 - t_3) = \frac{V_F i_{aux2}^2 L_{aux}}{2v_g} \quad (A.50)$$

$$E_{aux} = E_1 + E_2 + E_3 + E_{D1} + E_{D2} + E_{D3} \quad (A.51)$$

$$E_{on,Q2} = E_{on}(i_L - i_{aux2}, V_{ds1}) \quad (A.52)$$

$$E_{off,Q1} = E_{on}(\Delta i, V_{dc}) \quad (A.53)$$

Case d

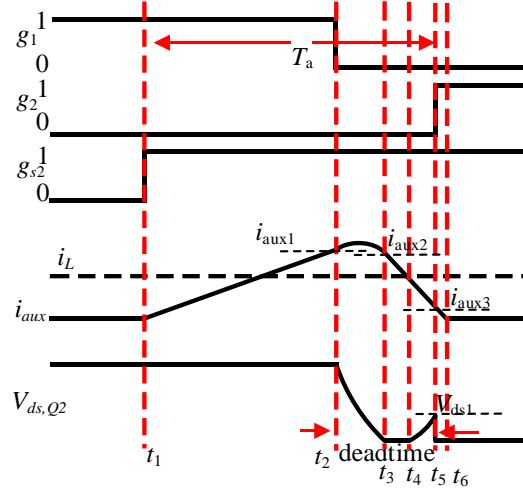


Figure A4 Case d of the Q_2 turn-on transition when $v_g > 0.5V_{dc}$

[t1~t2]:

$$v_{ds,Q2} = V_{dc} \quad (A.54)$$

$$i_{aux} = \frac{V_{dc} - v_g}{L_{aux}} (t - t_1) \quad (A.55)$$

$$t_2 - t_1 = T_a - \frac{\pi}{\omega_r} \quad (A.56)$$

$$i_{aux1} = \frac{V_{dc} - v_g}{L_{aux}}(t_2 - t_1) \quad (A.57)$$

$$\Delta i = i_{aux1} - i_L \quad (A.58)$$

$$E_1 = I_{rms1}^2 R_{aux}(t_2 - t_1) = \frac{i_{aux1}^3 L_{aux} R_{aux}}{3(V_{dc} - v_g)} \quad (A.59)$$

$$E_{D1} = \frac{1}{2} V_F i_{aux1}(t_2 - t_1) \quad (A.60)$$

[t2~t3]:

$$v_{ds,Q2} = v_g + (V_{dc} - v_g) \cos(\omega_r(t - t_2)) - \sqrt{\frac{L_{aux}}{2C_2}} \Delta i \sin(\omega_r(t - t_2)) \quad (A.61)$$

$$= k \cos(\omega_r(t - t_2) + \theta) + v_g$$

$$k = \sqrt{(V_{dc} - v_g)^2 + \frac{L_{aux}}{2C_2} \Delta i^2} \quad (A.62)$$

$$\theta = \tan^{-1} \left(\sqrt{\frac{L_{aux}}{2C_2}} \Delta i / (V_{dc} - v_g) \right) \quad (A.63)$$

$$i_{aux} = i_L + \frac{V_{dc} - v_g}{L_{aux} \omega_r} \sin(\omega_r(t - t_2)) + \Delta i \cos(\omega_r(t - t_2)) \quad (A.64)$$

$$t_3 - t_2 = \frac{\cos^{-1}(-v_g/k) - \theta}{\omega_r} = T_1 \quad (A.65)$$

$$i_{aux2} = i_L + \frac{V_{dc} - v_g}{L_{aux} \omega_r} \sin(\omega_r T_1) + \Delta i \cos(\omega_r T_1) \quad (A.66)$$

$$I_{rms2} = \sqrt{\frac{1}{t_3 - t_2} \int_{t_2}^{t_3} i_{aux}^2 dt} \quad (A.67)$$

$$E_2 = I_{rms2}^2 R_{aux}(t_3 - t_2) \quad (A.68)$$

$$E_{D2} = V_F \int_{t_2}^{t_3} i_{aux} dt \quad (\text{A.69})$$

[t3~t4]:

$$v_{ds,Q2} = 0 \quad (\text{A.70})$$

$$i_{aux} = i_{aux2} - \frac{v_g}{L_{aux}}(t - t_3) \quad (\text{A.71})$$

$$t_4 - t_3 = \frac{(i_{aux2} - i_L)L_{aux}}{v_g} = T_2 \quad (\text{A.72})$$

$$I_{rms3} = \sqrt{\frac{1}{t_4 - t_3} \int_{t_3}^{t_4} i_{aux}^2 dt} \quad (\text{A.73})$$

$$E_3 = I_{rms3}^2 R_{aux} (t_4 - t_3) \quad (\text{A.74})$$

$$E_{D3} = \frac{V_F i_{aux2}}{2} (t_4 - t_3) \quad (\text{A.75})$$

[t4~t5]:

$$v_{ds,Q2} = v_g - v_g \cos(\omega_r(t - t_4)) \quad (\text{A.76})$$

$$i_{aux} = i_L + \frac{-v_g}{L_{aux}\omega_r} \sin(\omega_r(t - t_4))$$

$$t_5 - t_4 = \frac{\pi}{\omega_r} - T_1 - T_2 = T_3 \quad (\text{A.77})$$

$$V_{ds1} = v_g - v_g \cos(\omega_r T_3) \quad (\text{A.78})$$

$$i_{aux3} = i_L + \frac{-v_g}{L_{aux}\omega_r} \sin(\omega_r T_3) \quad (\text{A.79})$$

$$I_{rms4} = \sqrt{\frac{1}{t_5 - t_4} \int_{t_4}^{t_5} i_{aux}^2 dt} \quad (\text{A.80})$$

$$E_4 = I_{rms4}^2 R_{aux} (t_5 - t_4) \quad (A.81)$$

$$E_{D3} = V_F \int_{t_4}^{t_5} i_{aux} dt \quad (A.82)$$

[t5~t6]:

$$v_{ds,Q2} = 0 \quad (A.83)$$

$$i_{aux} = i_{aux3} - \frac{v_g}{L_{aux}} (t - t_5) \quad (A.84)$$

$$E_5 = I_{rms5}^2 R_{aux} (t_5 - t_6) = \frac{i_{aux3}^3 L_{aux} R_{aux}}{3v_g} \quad (A.85)$$

$$E_{D5} = \frac{V_F i_{aux3}}{2} (t_5 - t_6) = \frac{V_F i_{aux3}^2 L_{aux}}{2v_g} \quad (A.86)$$

$$E_{aux} = E_1 + E_2 + E_3 + E_4 + E_5 + E_{D1} + E_{D2} + E_{D3} + E_{D4} + E_{D5} \quad (A.87)$$

$$E_{on,Q2} = E_{on}(i_L - i_{aux3}, V_{ds1}) \quad (A.89)$$

$$E_{off,Q1} = E_{on}(\Delta i, V_{dc}) \quad (A.90)$$

Case e

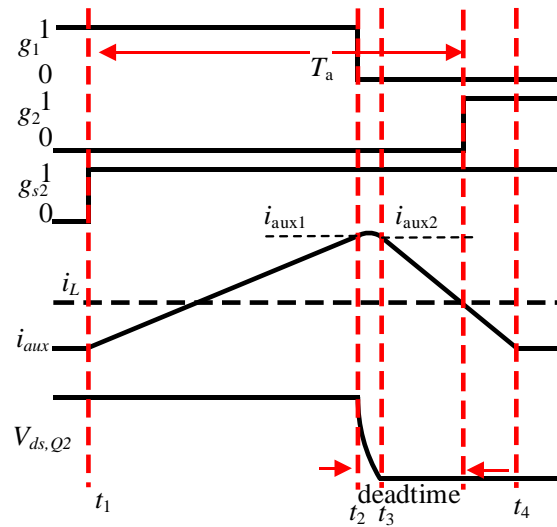


Figure A5 Case e of the Q_2 turn-on transition when $v_g > 0.5V_{dc}$

[t1~t2]:

$$v_{ds,Q2} = V_{dc} \quad (\text{A.91})$$

$$i_{aux} = \frac{V_{dc} - v_g}{L_{aux}}(t - t_1) \quad (\text{A.92})$$

$$t_2 - t_1 = T_a - \frac{\pi}{\omega_r} \quad (\text{A.93})$$

$$i_{aux1} = \frac{V_{dc} - v_g}{L_{aux}}(t_2 - t_1) \quad (\text{A.94})$$

$$\Delta i = i_{aux1} - i_L \quad (\text{A.95})$$

$$E_1 = I_{rms1}^2 R_{aux}(t_2 - t_1) = \frac{i_{aux1}^3 L_{aux} R_{aux}}{3(V_{dc} - v_g)} \quad (\text{A.96})$$

$$E_{D1} = \frac{1}{2} V_F i_{aux1}(t_2 - t_1) \quad (\text{A.97})$$

[t2~t3]:

$$v_{ds,Q2} = v_g + (V_{dc} - v_g) \cos(\omega_r(t - t_2)) - \sqrt{\frac{L_{aux}}{2C_2}} \Delta i \sin(\omega_r(t - t_2)) \quad (\text{A.98})$$

$$= k \cos(\omega_r(t - t_2) + \theta) + v_g$$

$$k = \sqrt{(V_{dc} - v_g)^2 + \frac{L_{aux}}{2C_2} \Delta i^2} \quad (\text{A.99})$$

$$\theta = \tan^{-1} \left(\sqrt{\frac{L_{aux}}{2C_2}} \Delta i / (V_{dc} - v_g) \right) \quad (\text{A.100})$$

$$i_{aux} = i_L + \frac{V_{dc} - v_g}{L_{aux} \omega_r} \sin(\omega_r(t - t_2)) + \Delta i \cos(\omega_r(t - t_2)) \quad (\text{A.101})$$

$$t_3 - t_2 = \frac{\cos^{-1}(-v_g/k) - \theta}{\omega_r} = T_1 \quad (\text{A.102})$$

$$i_{aux2} = i_L + \frac{V_{dc} - v_g}{L_{aux}\omega_r} \sin(\omega_r T_1) + \Delta i \cos(\omega_r T_1) \quad (\text{A.103})$$

$$I_{rms2} = \sqrt{\frac{1}{t_3 - t_2} \int_{t_2}^{t_3} i_{aux}^2 dt} \quad (\text{A.104})$$

$$E_2 = I_{rms2}^2 R_{aux} (t_3 - t_2) \quad (\text{A.105})$$

$$E_{D2} = V_F \int_{t_2}^{t_3} i_{aux} dt \quad (\text{A.106})$$

[t3~t4]:

$$v_{ds,Q2} = 0 \quad (\text{A.107})$$

$$i_{aux} = i_{aux2} - \frac{v_g}{L_{aux}} (t - t_3) \quad (\text{A.108})$$

$$E_3 = I_{rms3}^2 R_{aux} (t_4 - t_5) = \frac{i_{aux2}^3 L_{aux} R_{aux}}{3v_g} \quad (\text{A.109})$$

$$E_{D3} = \frac{V_F i_{aux2}}{2} (t_4 - t_5) = \frac{V_F i_{aux2}^2 L_{aux}}{2v_g} \quad (\text{A.110})$$

$$E_{aux} = E_1 + E_2 + E_3 + E_{D1} + E_{D2} + E_{D3} \quad (\text{A.111})$$

$$E_{on,Q2} = E_{on}(0,0) \quad (\text{A.112})$$

$$E_{off,Q1} = E_{on}(\Delta i, V_{dc}) \quad (\text{A.113})$$

APPENDIX B

CIRCUIT SCHEMATIC AND PCB LAYOUT OF THE HARDWARE

PROTOTYPE

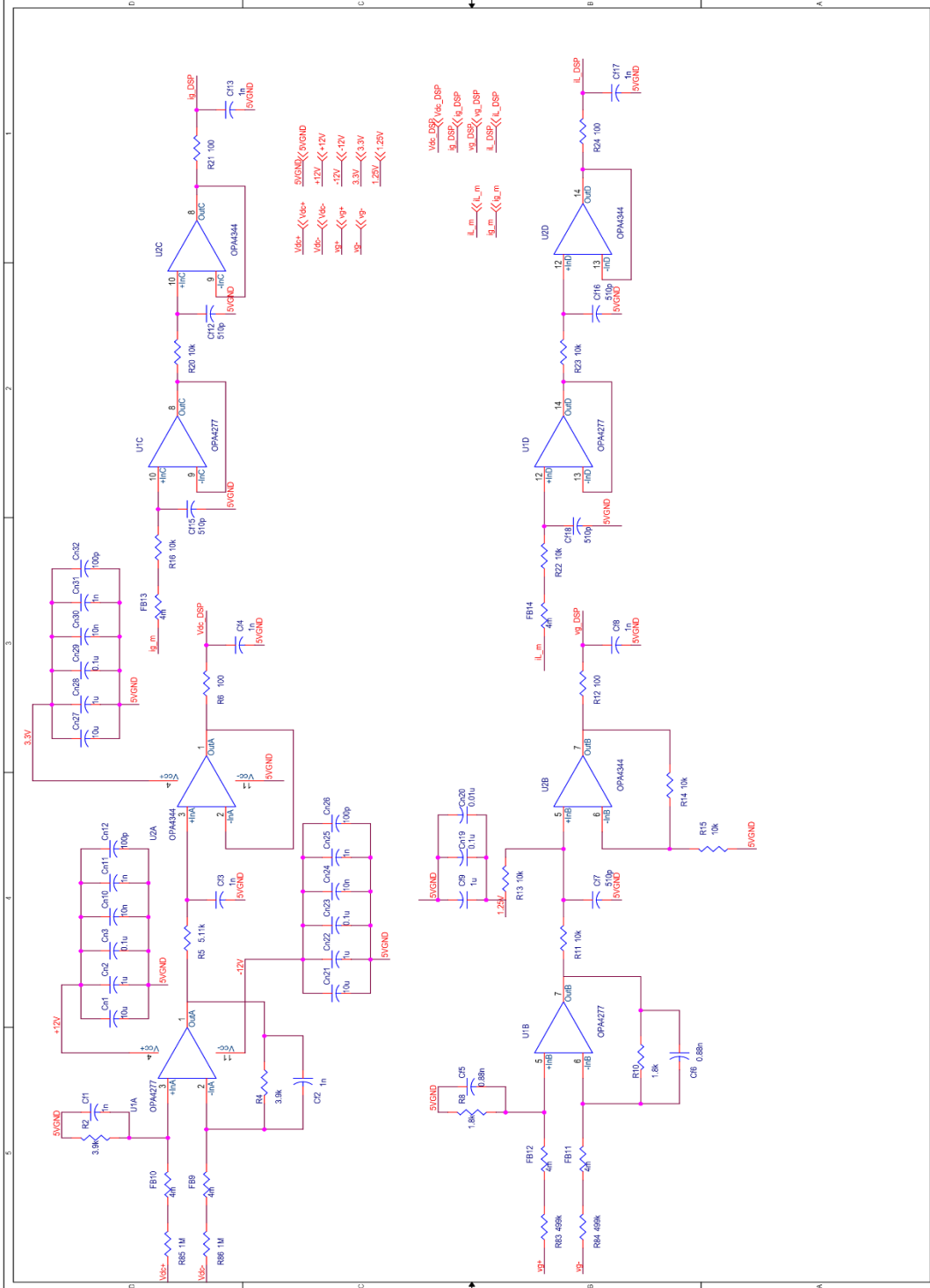


Figure B1 ZVT full-bridge inverter hardware prototype schematic: signal conditioning

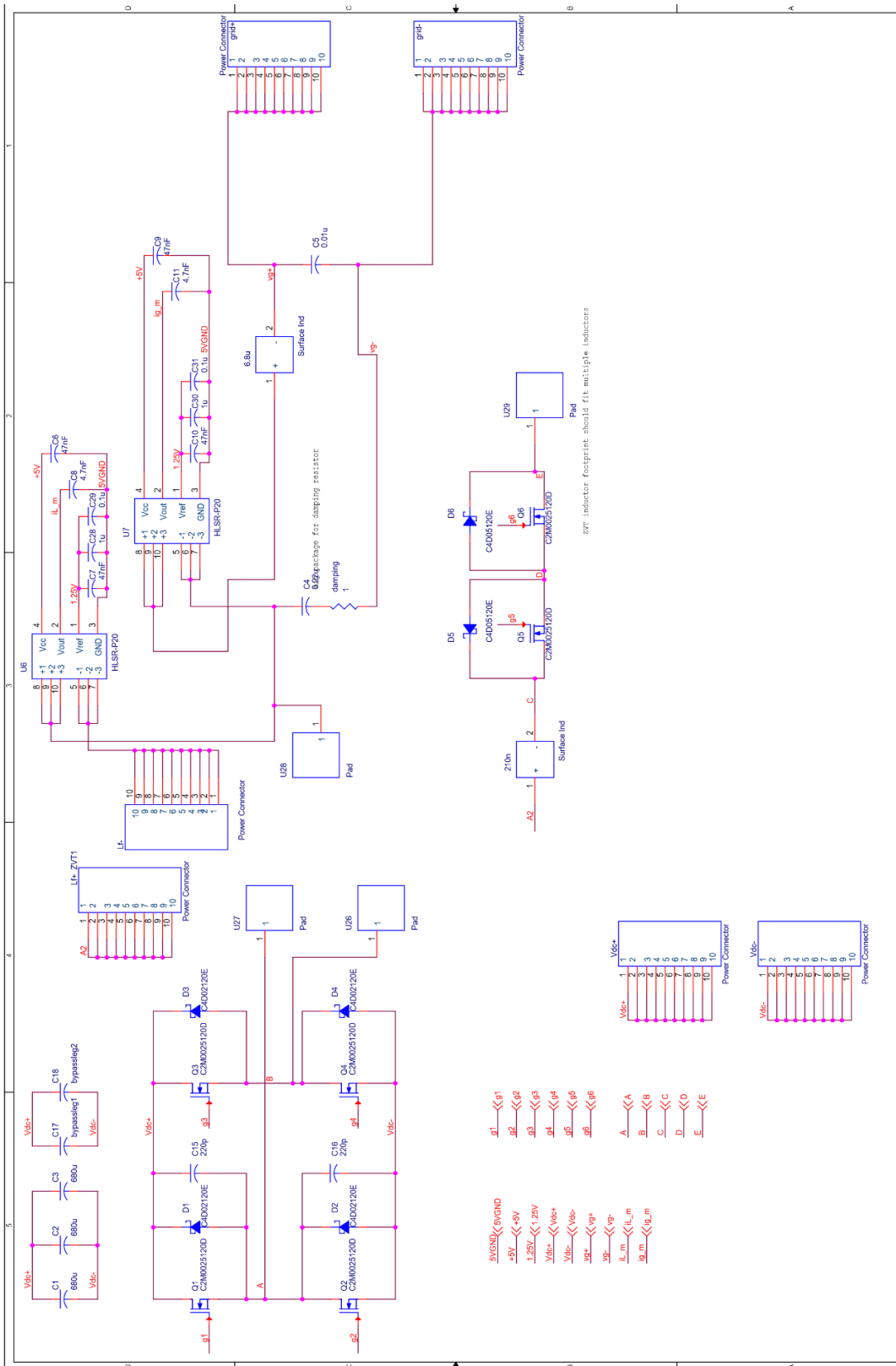


Figure B2 ZVT full-bridge inverter hardware prototype schematic: power stage

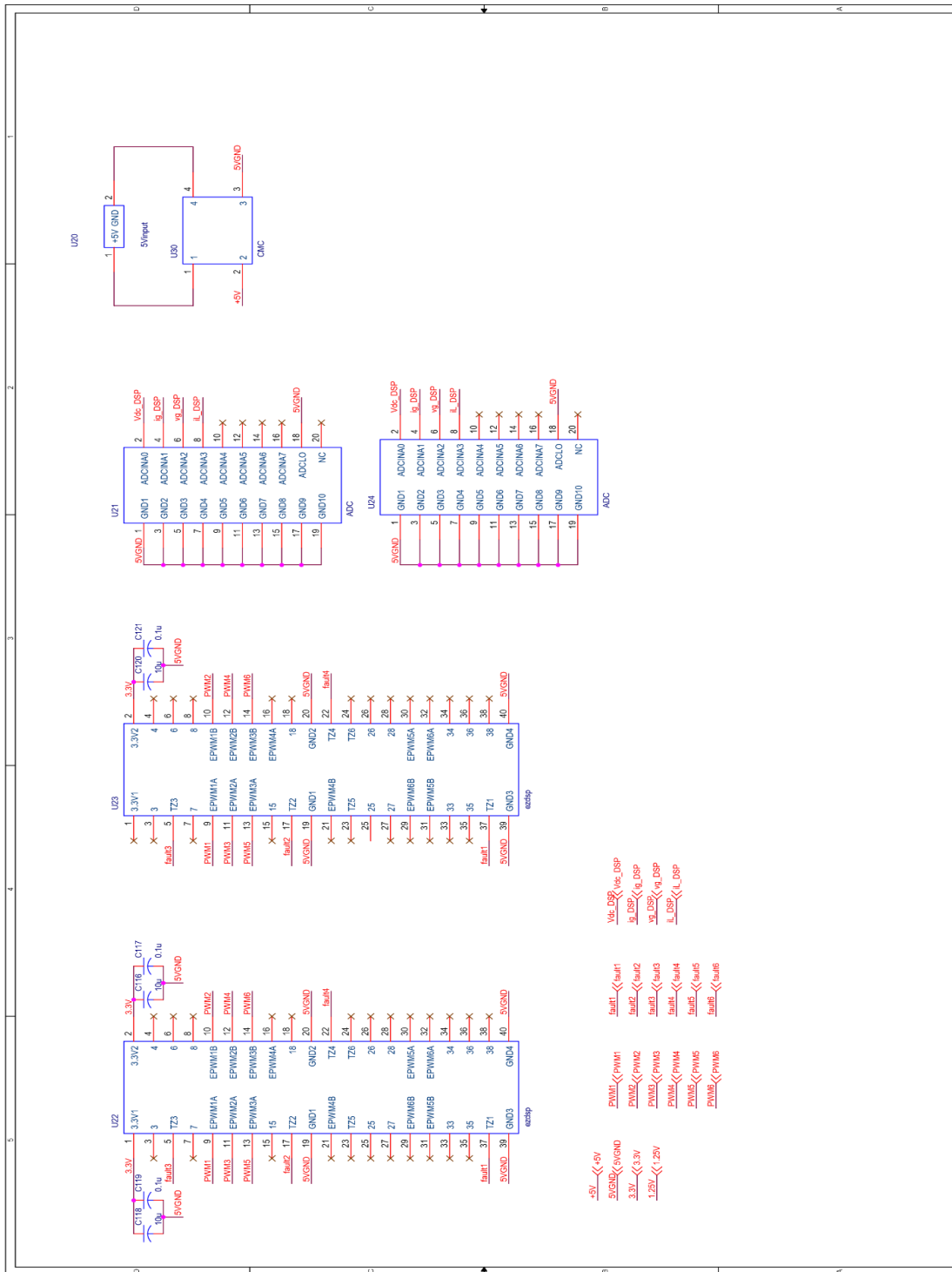


Figure B3 ZVT full-bridge inverter hardware prototype schematic: connectors

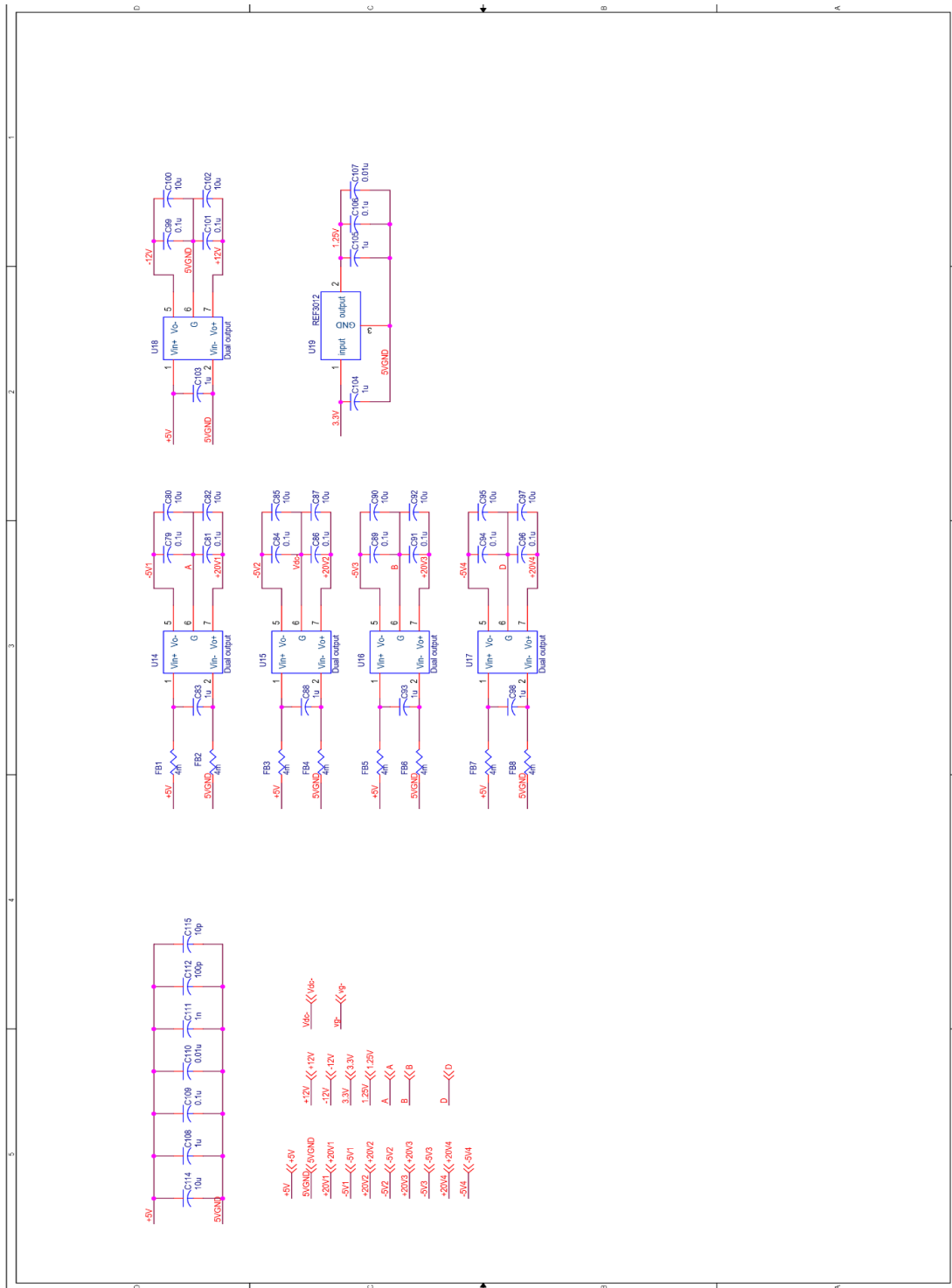


Figure B4 ZVT full-bridge inverter hardware prototype schematic: auxiliary DC power supply

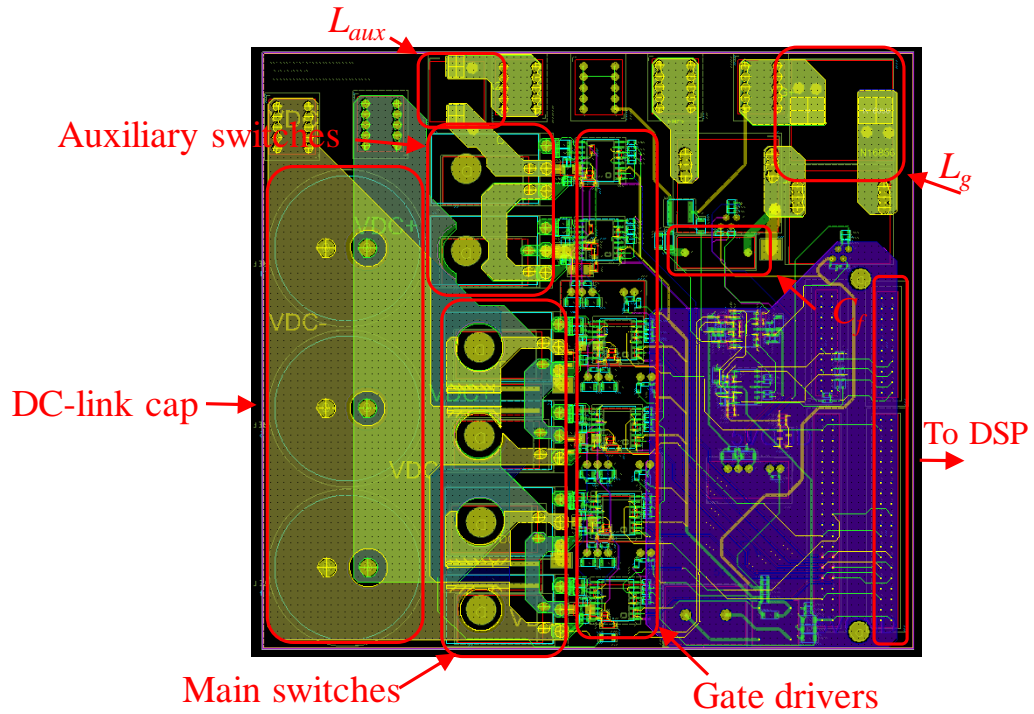


Figure B5 ZVT full-bridge inverter hardware prototype circuit board PCB layout

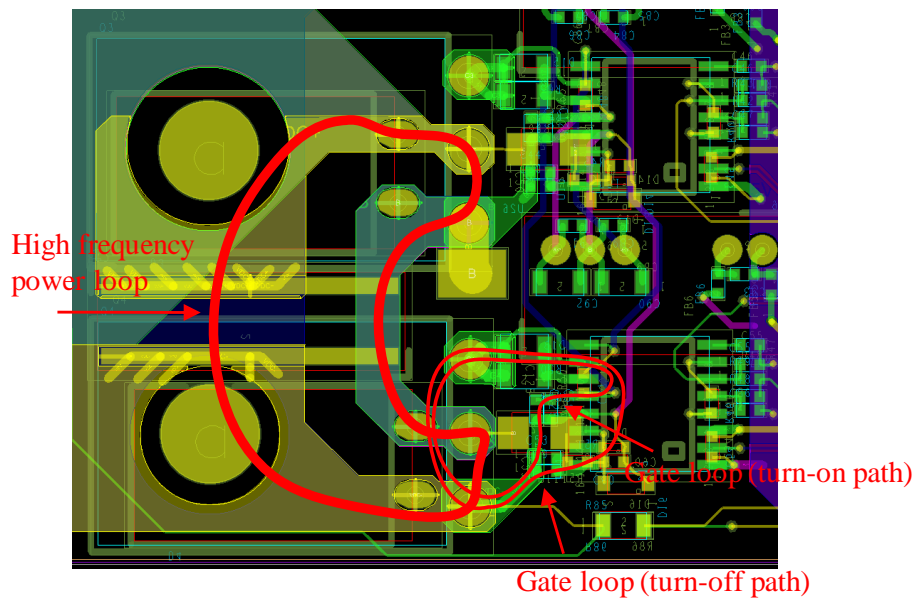


Figure B6 ZVT full-bridge inverter hardware prototype circuit board PCB layout: critical loops

APPENDIX C

BLOCK DIAGRAMS OF THE MICROGRID OPAL-RT MODEL

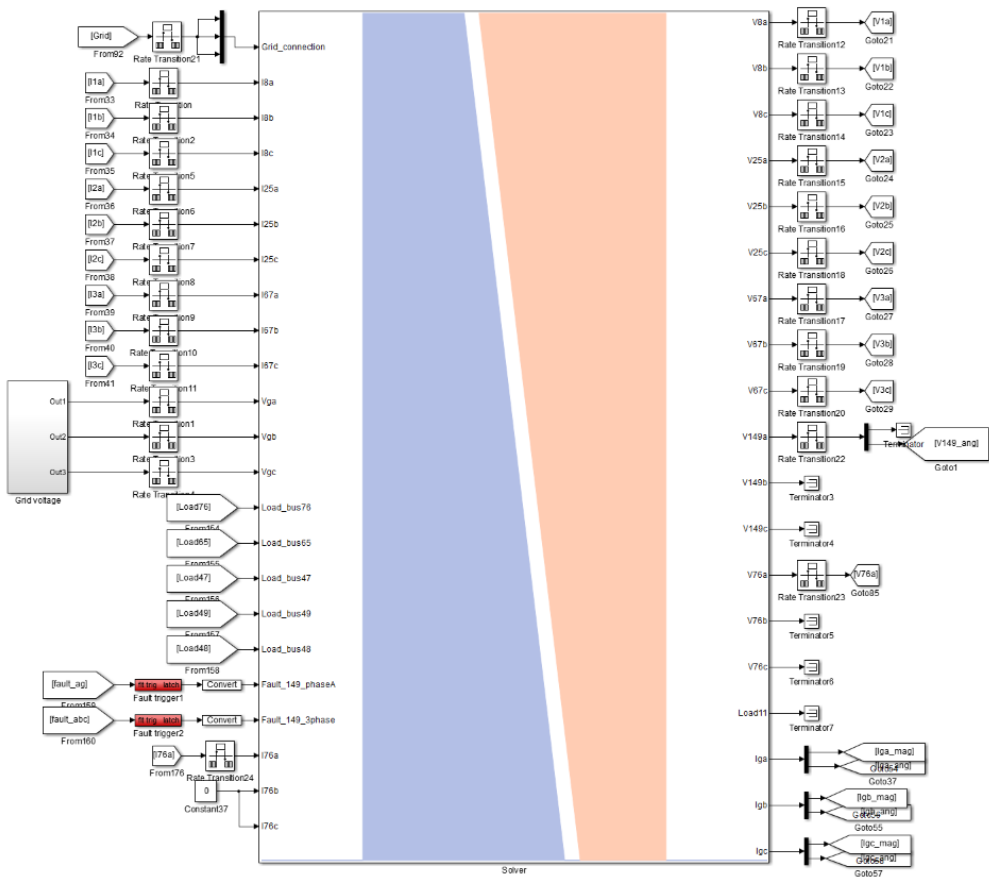


Figure C1 ePHASORsim model of IEEE 123 node test feeder

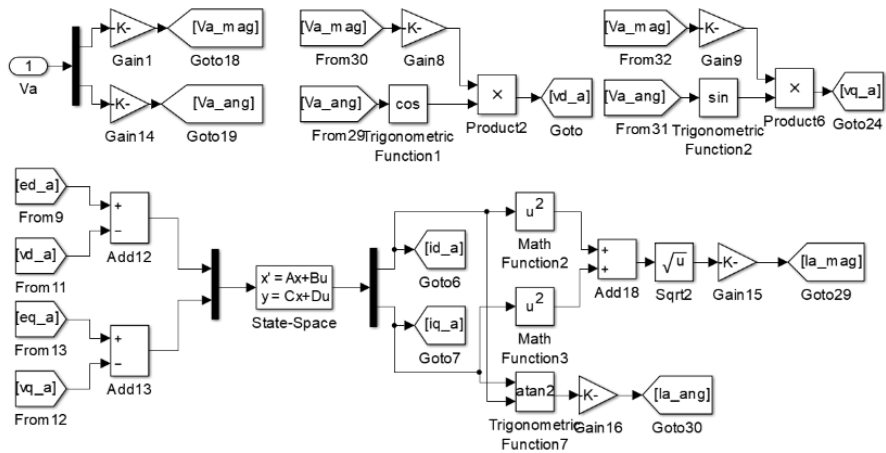


Figure C2 Grid filter dynamics

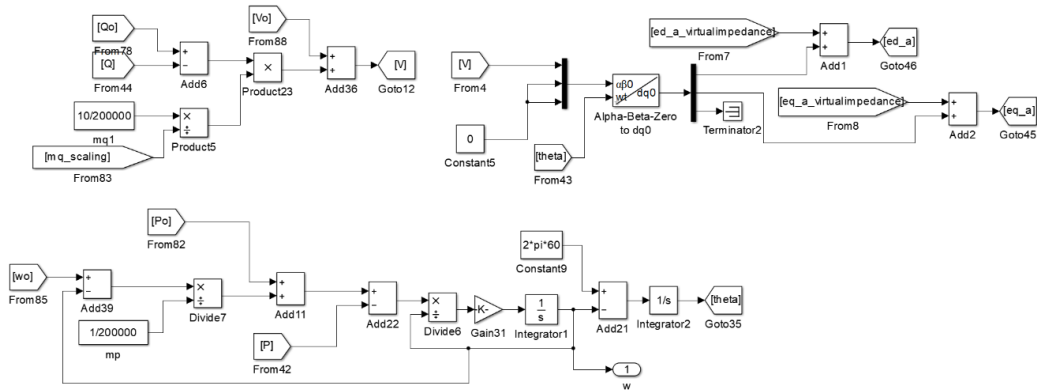


Figure C3 VSG control

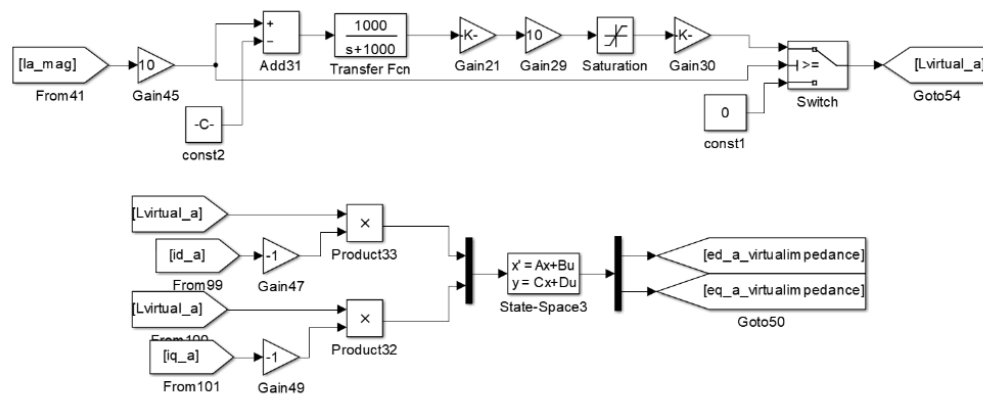


Figure C4 Virtual impedance current-limiting control

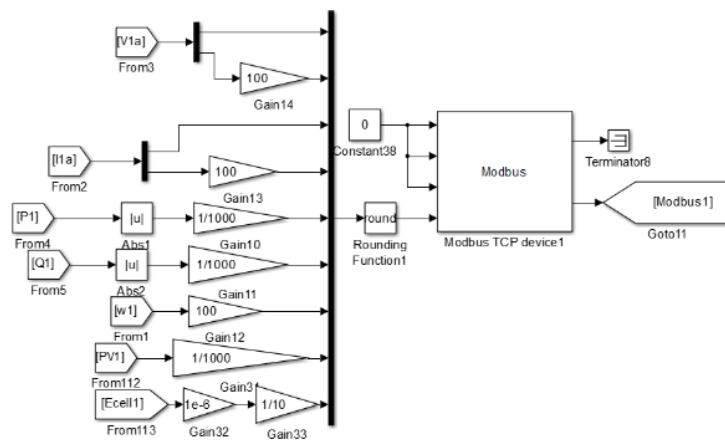


Figure C5 Modbus communication

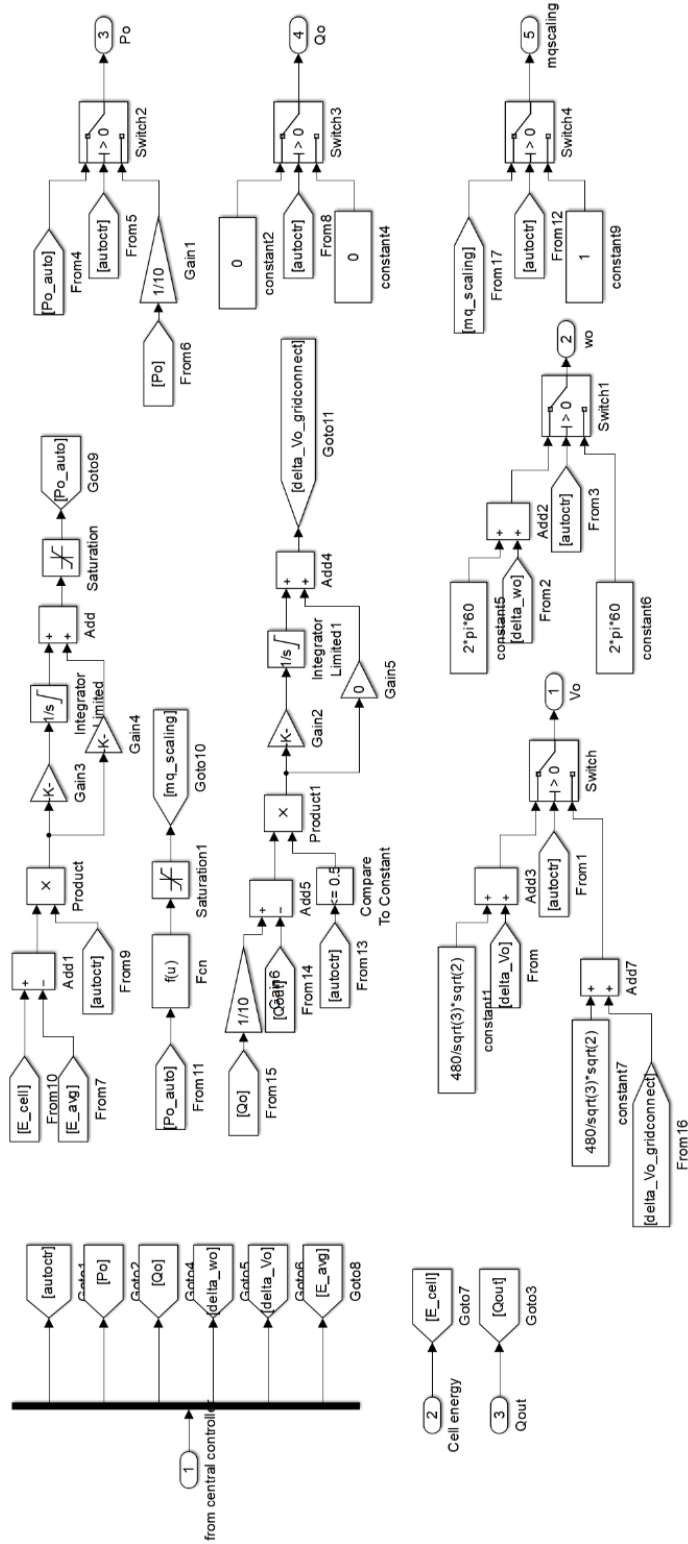


Figure C6 Control signal selection for different operating modes

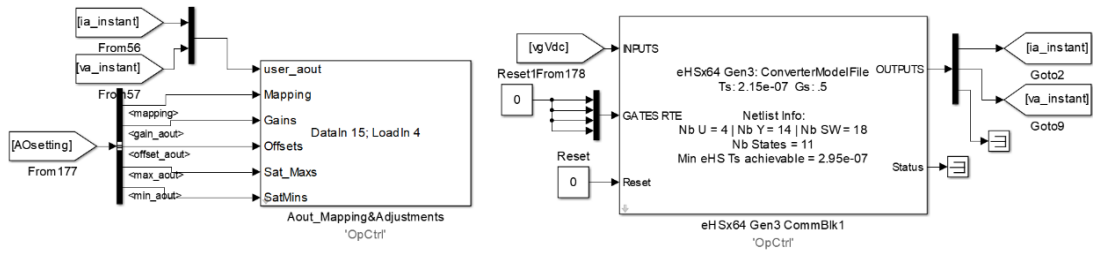


Figure C7 CHIL blocks

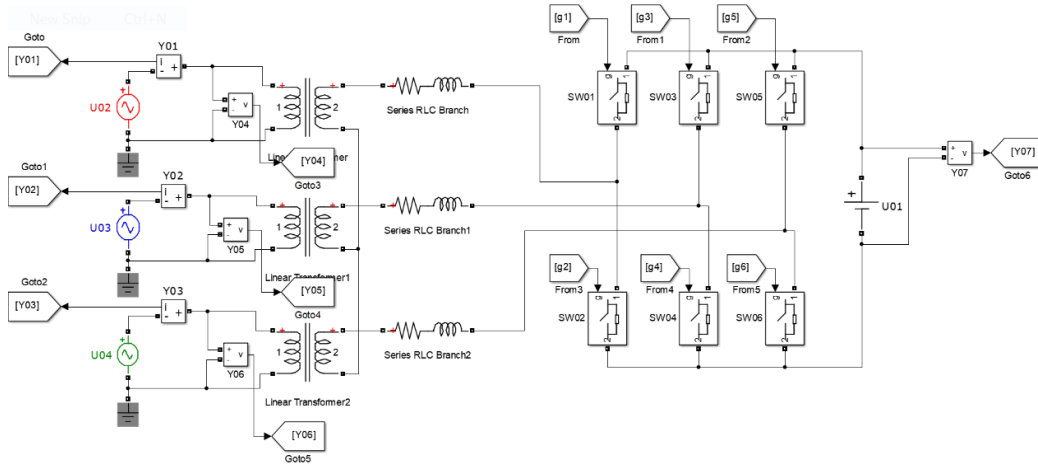


Figure C8 Inverter power stage circuit in CHIL simulation

APPENDIX D

MATLAB FUNCTION FOR THE DYNAMIC PHASOR MODEL OF SINGLE- PHASE PERMANENT-SPLIT CAPACITOR MOTOR

```

function
[d_ias_R,d_ibs_R,d_iar_R,d_ibr_R,d_vc_R,d_ias_I,d_ibs_I,d_iar_I,d_ibr_I
,d_vc_I,d_w,S_next] =
fcn(ias_R,ibs_R,iar_R,ibr_R,vc_R,ias_I,ibs_I,iar_I,ibr_I,vc_I,vs_R,vs_I
,theta,w,wt,S,Load)

wo = 2*pi*60;
Lm_unsat = 79.58e-3;
Ls_unsat = 1.3e-3;
Lr_unsat = 0.53e-3;
rr = 0.3;
Rs = 0.3;
C = 40e-6;
N = 1.4;
Tload = 6*Load;
Tav = 8*Load;
Hr = 0.00273;
Vbase = 230;
linkage_base = 1.414*Vbase/wo;

Lm = Lm_unsat/(1+S);
Ls = Ls_unsat/(1+S);
Lr = Lr_unsat/(1+S);

ias = cos(wt)*ias_R-sin(wt)*ias_I;
ibs = cos(wt)*ibs_R-sin(wt)*ibs_I;
iar = cos(wt)*iar_R-sin(wt)*iar_I;
ibr = cos(wt)*ibr_R-sin(wt)*ibr_I;

linkage = [Lm + Ls, 0 , Lm*cos(theta), Lm*sin(theta);
0, N*N*Lm + Ls, -N*Lm*sin(theta), N*Lm*cos(theta);
Lm*cos(theta), -N*Lm*sin(theta), Lm + Lr, 0;
Lm*sin(theta), N*Lm*cos(theta), 0, Lm + Lr;]*[ias;ibs;iar;ibr];

linkage_am = linkage(1) - Ls*(ias);
linkage_bm = linkage(2) - N*N*Ls*(ibs);
linkage_m = sqrt(linkage(1)*linkage(1) +
linkage(2)*linkage(2))/linkage_base;

if (linkage_m>0.758)
    S_next = 0.511*(linkage_m-0.758)^2;
else
    S_next = 0;
end

Te = linkage_am*(-iar*sin(theta)+ibr*cos(theta)) -
linkage_bm*(iar*cos(theta)+ibr*sin(theta));

AAA = mod(theta+pi,pi/2);
if (mod(theta+pi,pi)<pi/2)
    AAAA = Tav + Tav*(AAA-pi/4)*2/(pi/2);
else
    AAAA = -Tav+Tav*(3*pi/4-AAA)*2/(pi/2);
end

```

